Large Electroclinic Effect and Stability of Chiral Smectic Liquid Crystals

by

Uttam Manna

A thesis submitted for the
degree of Doctor of Philosophy

in the

Advanced Electronic Materials Laboratory
Department of Electronic and Electrical Engineering

Trinity College
The University of Dublin

August 2009

Declaration of Authorship

I, Uttam Manna, declare that this thesis titled, 'Large Electroclinic Effect and Stability of Chiral Smectic Liquid Crystals' and the work presented in it are my own. I confirm that:

- It has not been submitted as an exercise for a degree at this or any other University.
- It is entirely my own work, except where otherwise stated.
- I have quoted from the work of others, the source is always given. With the exception of such quotations, this thesis is entirely my own work.
- I agree that the Library may lend or copy the thesis upon request. This permission overs only single copies made for study purposes, subject to normal conditions of acknowledgment.

Signed: _____

Date: _____

"Science is a wonderful thing if one does not have to earn one's living at it."

Albert Einstein

"We are responsible for what we are, and whatever we wish ourselves to be, we have the power to make ourselves. If what we are now has been the result of our own past actions, it certainly follows that whatever we wish to be in future can be produced by our present actions; so we have to know how to act."

Swami Vivekananda

Acknowledgements

My journey started on November 2005 on a rainy and windy Sunday afternoon when I arrived in Dublin with a great deal of excitement, anticipation and expectations. Several people have played a decisive role towards successful completion of my Ph. D. Its my great pleasure to get a chance to acknowledge them.

At the start of my Ph. D, I knew almost nothing about 'Liquid Crystals' except the two words, 'Liquid' and 'Crystals.' In this regard, first of all, I would like to express my thankful gratitude to my supervisor **Prof. Jagdish K. Vij** for not only giving me a chance to prove my credentials as a research student in the field of Liquid Crystals but also for his guidances, encouragements and advices. He supported me in all respects, especially when implementing my own ideas.

I was fortunate to have **Dr. Jang-Kun Song** as one of my colleagues. He helped me in many aspects of my Ph. D, which include interpreting experimental results, teaching experimental techniques and discussing personal problems. I was also fortunate to have **Dr. Gerard Power** as one of my colleagues. He is one of the nicest and intelligent people, I have ever met. I am grateful to **Dr. Vitaly Panov** and **Dr. Yuri Panarin** for teaching me many experimental techniques, simulating discussions and dealing with my questions with patience. I am grateful to **Prof. Atsuo Fukuda** for donating his valuable liquid crystalline compounds. I sincerely thank **Prof. Antoni Kocot**, **Dr. Olga Panarina**, **Dr. A. D. L. Chandani** and **Dr. V. Manjuladevi** and **Eammon** for their helpful advice. My sincere thanks to **Prof. Robert Richardson** at the University of Bristol for carrying out x-ray diffraction measurements on my samples.

I also would like to thank our Head of the Department **Dr. Martin Burke** for his support and **Ms. Bernadatte Clerkin** for helping me in many aspects. I thank Trinity College Dublin for awarding me a Trinity College Postgraduate Studentship and Science Foundation of Ireland (SFI) for financial support.

I thank my wife, Mahua for bringing stability in my personal life. She was always there with me in good and bad times. I am grateful to my family friends (Amsarani, Shantanu, Arundhuti, Sukanta and Gopali) for their emotional support during my stay in Dublin.

Lastly, I come to my parents and brother. It is impossible to describe their contributions in words. They sacrificed a large portion of their life supporting me.

To my

Parents . . .

Summary

Large electroclinic effect in the smectic-A^* phase and stability of smectic-C^* variant phases are investigated in detail. Investigation of large electroclinic effect in the smectic-A^* phase is one of the recent topics, and stability of smectic-C^* variant phases is one of the less established topics in the field of chiral smectic liquid crystals. Various new physical phenomena were observed and interpreted.

An electric field applied parallel to the layer of a smectic-A^* (Sm-A^*) liquid crystal induces a molecular tilt relative to the layer normal, called the electroclinic effect. The electroclinic effect is a unique and technologically useful electro-optical property of the Sm-A^* liquid crystal phase. The physical properties of electroclinic liquid crystals having large induced tilt and small layer contraction (de Vries smectics) are studied using x-ray diffraction, electro-optic and dielectric spectroscopy.

Mixtures of different compositions of an antiferroelectric and ferroelectric liquid crystal compounds that exhibits Sm-A^* to Sm-C^* and Sm-C^*_A transitions were studied. The results of optical texture, birefringence, tilt angle and x-ray diffraction suggest that a part of the Sm-A^* phase is of de Vries type. An increase in the tilt angle with decreasing temperature results in a reduction in the value of the birefringence in the Sm-A^* phase, whereas the birefringence at Sm-A^* to Sm-C^* transition goes up significantly. For the de Vries Sm-A^* to Sm-C^* transition, the soft mode relaxation strength decreases, the Landau coefficient increases, and the Curie-Weiss temperature range decreases with an increased ferroelectric composition in the mixtures.

The dielectric strength is shown to increase, the relaxation frequency to decrease, and the response time to increase in the de Vries-type Sm-A^* phase up to a certain value of the electric field. This behavior contrasts to that observed in a conventional Sm-A^* phase. On assuming that the reorientation of the molecular dipoles with application of the electric field is of the Langevin type in the de Vries-type Sm-A^* phase, it was found that a certain number of molecules corresponding to a correlation length of $\xi_\perp \approx 45\ nm$ in a single layer, cooperatively respond to the applied field, predicted for the first time.

The stability of SmC^*_α, Sm$C^*_A(1/2)$, Sm$C^*_A(1/3)$ and SmC^*_A phases were investigated by determining the transition temperatures and the temperature ranges for which these are stable by varying the cell thickness experimentally. This is

a problem of nearly fifteen years old and was analyzed with a unique approach. This approach may be useful to other areas of surface sciences as well. A simple theory has explained experimental observations that the relative stability of any phase is found to be due to its large polar anchoring strength and low free energy compared to other phases in a cell.

The effects of confinement and electric field on the Sm-C^*_α phase were studied for various cell thicknesses under the influence of an electric field. On reducing the cell thickness, the surface-induced mode appears, as a result the dielectric strength of the Sm-C^*_α phase increases, and the distribution parameter, α, of the relaxation process decreases significantly. On increasing the electric field, the dielectric strength decreases and the relaxation frequency increases in the Sm-C^*_α phase. These are explained by the 'helical fracture' model, originally proposed for the Sm-C^* phase.

Contents

List of Figures

The captions listed here are not full captions but concise ones.

List of Tables

Abbreviations

LC	**L**iquid **C**rystal
LCD	**L**iquid **C**rystal **D**isplay
F	**F**erroelectric
AF	**A**nti-**F**erroelectric
FLC	**F**erroelectric **L**iquid **C**rystal
AFLC	**A**nti-**F**erroelectric **L**iquid **C**rystal
SSFLC	**S**urface **S**tabilized **F**erroelectric **L**iquid **C**rystal
SmA	**Sm**ectic **A** type phase (achiral)
SmC	**Sm**ectic **C** type phase (achiral)
SmA^*	chiral **Sm**ectic **A** phase (achiral)
SmC^*	chiral **Sm**ectic **C** phase
SmC^*_A	chiral **Sm**ectic $\mathbf{C}_A$ type phase
SmC^*_A**(1/3),Sm**C^*_γ	chiral 3-layer ferrielectric **Sm**ectic phase
SmC^*_A**(1/2),AF**	chiral 4-layer ferrielectric **Sm**ectic phase
SmC^*_α	chiral **Sm**ectic C^*_α phase
Cr.	**Cr**ystal phase
Iso.	**Iso**tropic phase
$^\circ C$	Degree Centigrade
ITO	**I**ndium **T**in **O**xide
dc, DC	**D**irect **C**urrent
ac, AC	**a**lternating **c**urrent
P_s	(**S**pontaneous) **P**olarization
E	**E**lectric field
T	**T**emperature

n	refractive index
S	S order parameter
D	D order parameter
P	P order parameter
C	C order parameter
PEM	**P**hoto **E**lastic **M**odulater
IR	**I**nfra **R**ed
$C_n,\ C_2$	n (2)-fold rotational symmetry group
C_{nh}	C_{nh} symmetry group
$D_n,\ D_2$	n (2)-fold rotational symmetry and flipping symmetry group
D_{nh}	D_{nh} symmetry group
PET	**P**oly**e**thylen **T**erephthalate
p	**p**itch
q	wave vector
α	polarizability, or an coefficient of the Landau expansion
$\epsilon,\ \epsilon',\ \epsilon''$	dielectric susceptibility, real part, imaginary part of

List of Publications

1. K. L. Sandhya, Y. P. Panarin, U. Manna, J. K. Vij, and S. Kumar, Comment on *Optical and Resonant X-Ray Diffraction Studies Confirm a SmC*FI2-SmC* Liquid Crystal Phase Sequence Reversal*, **Physical Review Letters**, **98**, 219801, (2007).

2. J. K. Song, U. Manna, Atsuo Fukuda, and J. K. Vij, *Sign reversals in the dielectric anisotropy as functions of temperature and frequency in SmA* phase*, **Applied Physics Letters**, **91**, 042907, (2007).

3. J. K. Song, U. Manna, and J. K. Vij, *"Mechanism of field induced unwinding of SmC* helix and bias field dependencies of dielectric permittivity and effective polarization"*, **Europhysics Letters**, **82**, 26003, (2008).

4. U. Manna, J. K. Song, Yu. P. Panarin, A. Fukuda, and J. K. Vij, *"Electro-optic and dielectric study of the de Vries–type smectic-A* phase exhibiting transitions to smectic-C_A^* and smectic-C* phases"*, **Physical Review E**, **77**, 041707, (2008).

5. U. Manna, J. K. Song, G. Power, and J. K. Vij, *"Effect of the cell surfaces on the stability of the chiral smectic-C phases"*, **Physical Review E**, **78**, 021711, (2008).

6. J. K. Song, U. Manna, A. Fukuda, and J. K. Vij, *"Antiferroelectric relaxation process in dielectric permittivity and the interlayer interaction in antiferroelectric liquid crystals"*, **Applied Physics Letters**, **93**, 142903 (2008).

7. U. Manna, J. K. Song, and J. K. Vij, *"Electric Field dependent dielectric response in the de Vries-type smectic-A* phase possessing local orientational order with nanoscale correlation length"*, **Physical Review E**, **78**, 041705 (2008).

8. U. Manna, J. K. Song, J. K. Vij, and J. Naciri *"Anomalous dependence of response time on electric field in an electroclinic liquid crystals with large induced tilt and polarization"*, **Applied Physics Letters**, **94**, 012901 (2009).

9. Y. Suzuki, G.-P. Chen, U. Manna, J. K. Vij, and A. Fukuda, *Realization of Field Sequential Color in Simple Matrix Antiferroelectric Liquid Crystal Displays by Utilizing Fast Pretransitional Response*, **Applied Physics Express**, **2**, 071403 (2009).

10. U. Manna, J. K. Song, A. D. L. Chandani, and J. K. Vij, *"Effects of confinement and electric field on the dielectric behavior of smectic-C^*_α phase"*, **Molecular Crystals and Liquid Crystals, In Press**.

11. M. Nagaraj, Y.P. Panarin, U. Manna, J.K. Vij, and C. Tschierske, *Electric field induced biaxiality and the electro-optic effect in a cluster nematic phase of bentcore liquid crystals*, (Submitted).

12. U. Manna, R. M. Richardson, and J. K. Vij, *"X-ray diffraction study of ferroelectric and antiferroelectric liquid crystal mixtures exhibiting de Vries SmA^*-SmC^* transitions"*, (In preparation).

List of Presentations

1. J. K. Song, U. Manna, and J. K. Vij, *"High frequency collective mode of dielectric relaxation in antiferroelectric liquid crystal"*, **Proceedings of the 11th Conference On Ferroelectric Liquid Crystals, FLC07, Sapporo, Japan**, P2-18, p. 124 (2007).

2. K. L. Sandhya, Yu. P. Panarin, J. K. Song, U. Manna, J. K. Vij, and S. Kumar, *"Electro-optics and Dielectric Studies Evidences the SmC^*_{FI2} - SmC^* Liquid Crystal Phase Sequence Reversal"*, **Proceedings of the 11th Conference On Ferroelectric Liquid Crystals, FLC07, Sapporo, Japan**, (2007).

3. V. P. Panov, U. Manna, K. L. Sandhya, and J. K. Vij, **Behavior of Smectic phases in Freestanding Film Geometry**, **Proceedings of the 11th International Conference on Ferroelectric Liquid Crystals**, Sapporo, Japan, 03-08 Sept. (2007).

4. J. K. Song, U. Manna, and J. K. Vij, *"Mechanism of Field Induced Unwinding of SmC* Helix and Bias Field Dependencies of Dielectric Permittivity and Effective Polarization"*, **Proceedings of the 22nd International Liquid Crystal Conference, ILCC08, Jeju Island, Korea**, (2008).

5. J. K. Song, U. Manna, and J. K. Vij, *"Surface Confinement Effect in Various Smectic C Phases"*, **Proceedings of the 22nd International Liquid Crystal Conference, ILCC08, Jeju Island, Korea**, (2008).

6. U. Manna, J.-K. Song, and J. K. Vij, *"Investigation of the Electric Field Dependent Dielectric Response using 'Helical Fracture' Model and Effects of the Confinement in the Sm-Ca* Phase"*, **Proceedings of the 22nd International Liquid Crystal Conference, ILCC08, Jeju Island, Korea**, (2008).

7. U. Manna, J.-K. Song, J. K. Vij, and J. Naciri, *"Behavior of the Optical Birefringence and Electric Field Dependent Dielectric Response in the de Vries-type Sm-A* Phase possessing Local Orientational Order with Nanoscale Correlation Length"*, **Proceedings of the 22nd International Liquid Crystal Conference, ILCC08, Jeju Island, Korea**, (2008).

8. U. Manna, J.-K. Song, J. K. Vij, and J. Naciri, *"Behavior of Response time in an Electroclinic Liquid Crystal with Large induced Tilt and Polarization"*, **Proceedings of the 2nd International Conference on Liquid Crystal for Photonics, LCP-2008, University of Cambridge, UK**, (2008).

Chapter 1

Introduction

"In this chapter, *the preface, fundamentals of liquid crystals, and the background required to understand the large electroclinic effect and stability of chiral smectic liquid crystal are discussed.* "

1.1 Preface

Liquid crystal science and applications now permeate almost all segments of society from large industrial displays to individual homes and offices. Non-display applications in nonlinear optics, optical communication, and data/signal/image processing are receiving increasing attention and are growing at a rapid pace. The idea of having a spontaneous electric polarization in a ferroelectric liquid crystal was revolutionary. The technological importance of these materials was realized after the discovery of fast electro-optic switching. This discovery triggered a long and fruitful period of fundamental research in the field of ferroelectric liquid crystals that culminated in discovery of antiferroelectric and intermediate ferrielectric phases. Apart from application point of view, the physical characteristics of liquid crystals have also attracted many scientists' interest over the decades. As

in all other areas of science, understanding and academic achievement in the liquid crystal field have been advanced originally by several pioneering scientists' inspirations, and subsequently by the contributions, small or large, of many other scientists inspired by previous discoveries.

This thesis presents the work done in the field of smectic liquid crystals, in particular large electroclinic effect and stability of chiral smectic liquid crystals on the basis of the knowledge already established by other scientists. It is hoped that this work will draw attention to new students and inspire them in further research and development in the field. Investigation of a large electroclinic effect in the smectic-A^* phase is one of the most recent topics, and stability of smectic-C^* variant phases is one of the less established topics in the field of chiral smectic liquid crystals. This thesis reports a number of new physical observations and their explanations.

The thesis consists of nine chapters. The first part of the thesis deals with the large electroclinic effect in the smectic-A^* phase, and the second part of the thesis deals with the stability of smectic-C^* variant phases.

Chapter 1 is the introduction, which briefly outlines the basic concepts of liquid crystals and their various phases, and describes some mathematical tools required to realize the subject matter of this work. However, the reader should realize that this does not suffice either to give a full introduction to the field of liquid crystals or to provide the requisite mathematical and theoretical background for the subject matter described in this work.

Chapter 2 describes the basic concepts of the experimental techniques and how these techniques are used to study smectic liquid crystals. The experimental methods used in this work are Broadband Dielectric Spectroscopy, Polarizing Microscopy, UV-VIS-NIR Spectroscopy, X-ray Diffraction and Electro-optic spectroscopy.

In **Chapter 3, 4 and 5**, the electroclinic liquid crystals exhibiting Sm-A^*-Sm-C^*_A and Sm-A^*-Sm-C^* transitions are studied using electro-optics, x-ray diffraction and dielectric spectroscopy. Some of the Landau parameters associated with the de Vries Sm-A^* to Sm-C^*_A and to Sm-C^* transitions are also determined using Landau theory of second order phase transitions.

In **Chapter 6**, electric field dependent dielectric response, and response time of electroclinic liquid crystals with small layer contraction are presented. The electric field dependent polarization data is fitted to the Langevin theory to determine the correlation length in these materials.

In **Chapter 7 and 8**, effect of the cell surfaces and electric field on the stability of the variant chiral smectic-C phases are presented. The experimantal results are fitted to the theory derived from the discrete flexoelectric model and also by considering the director distribution of variant smectic-C^* phases. The electric field dependent dielectric response in the Sm-C^*_α phase is also explained by a non-diverging pitch model.

Chapter 9 contains the conclusion of this thesis and proposed future work. Also in **Appendix A**, materials, apparatus and softwares used in this thesis are summarized.

1.2 The liquid-crystalline state

A liquid-crystalline state is a state of matter which exists between the organized solid and the amorphous liquid. Strictly, the liquid crystal or mesomorphic state is made up of a number of orientationally ordered mesophases which occur between the breakdown of transitional positional ordering of the molecules in a crystal and the formation of the orientationally disordered state of a liquid.

Typically the breakdown in molecular ordering on passing from a crystal to a liquid can be achieved either by changing the temperature of the material or by dissolving the material in a liquid. Liquid crystals that are formed by heating and/or cooling processes are called thermotropic liquid crystals, and those that are formed when a material dissolves in a solvent are called lyotropic liquid crystals. Typically the liquid crystal state has come to be defined as any state of matter where the molecules are orientationally ordered, but yet are in dynamic motion. Thus, this definition also includes soft crystals, sometimes called anisotropic plastic crystals, which can be formed between the solid and liquid crystal states. This thesis deals with the chiral smectic phases of thermotropic liquid crystals.

1.3 Liquid crystalline phases and subphases

A liquid crystalline material has, like normal materials, a solid phase (normally crystalline, i.e. containing both orientational and 3D positional order) and a liquid (isotropic) phase. However, in between these two phases the material has one or more intermediate liquid crystal phases as described below.

Nematic Phase: The simplest of all the phases is nematic phase (shown in Fig.1.1), where there is no positional order, but the molecules locally orient parallel to a certain direction called the director, denoted by **n**.

Smectic Phase: In these phases, the molecules are positionally ordered in layers, i.e. there is translation order along one dimension (shown in Fig.1.1), but within the layer there is no long-range positional order. A number of different smectic phases exist such as,

i) **Smectic-*A* (Sm-*A*)**: In Sm-*A* phase, the director is oriented along the layer normal.

ii) **Smectic-*C* (Sm-*C*)**: In Sm-*C* phase, there is a non-zero tilt angle between the director and the layer normal.

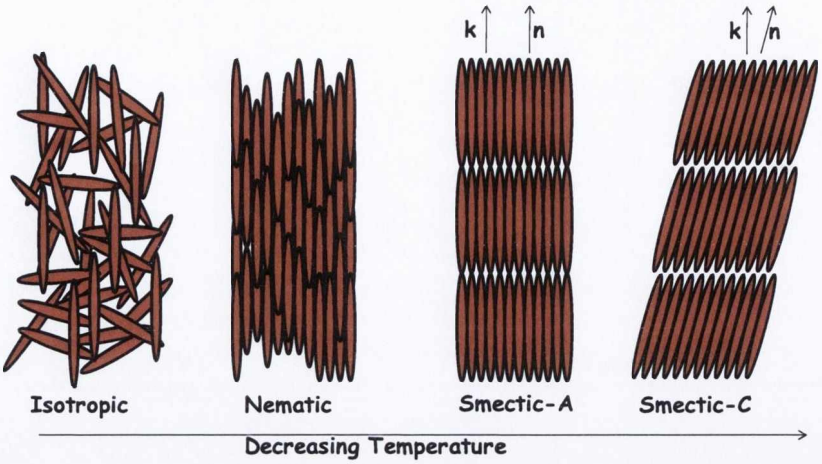

Figure 1.1: The structure of the liquid crystalline phases, illustrated for the case of rod-like molecules on changing the temperature.

1.3.1 Variant chiral smectic phases

If the liquid crystal molecules are chiral, i.e. they lack mirror symmetry, this may radically change the macroscopic behaviour of the phase, and such a phase is differentiated from the achiral one by adding a star after the letter, e.g. Sm-C^*, Sm-A^*, etc. The molecular arrangement of the chiral phase may be completely similar to the achiral version (as in Sm-A and Sm-A^*) or distinctly different (as in Sm-C and Sm-C^*), but the physical properties of the chiral phases are always different from those of the achiral ones.

Although an infinite number of variations of chiral smectic-C^* type order have been predicted theoretically [1–3] only five types have been discovered in reality. Our current understanding of how the director $\mathbf{n}$ (and thereby the polarization, being related to the director through $\mathbf{P} \propto \mathbf{k} \times \mathbf{n}$ [4], where $\mathbf{k}$ is the smectic layer normal) is modulated in the five different chiral smectic-C^* type phases is summarized graphically in Fig.1.2. This picture is based on a compilation of experimental data mainly from resonant x-ray scattering, ellipsometry and optical rotatory power measurements [5]. While the director modulation in Sm-C^*_α is incommensurate with the layer spacing, we can define 'repeating units' of one, four, three and two layers, respectively.

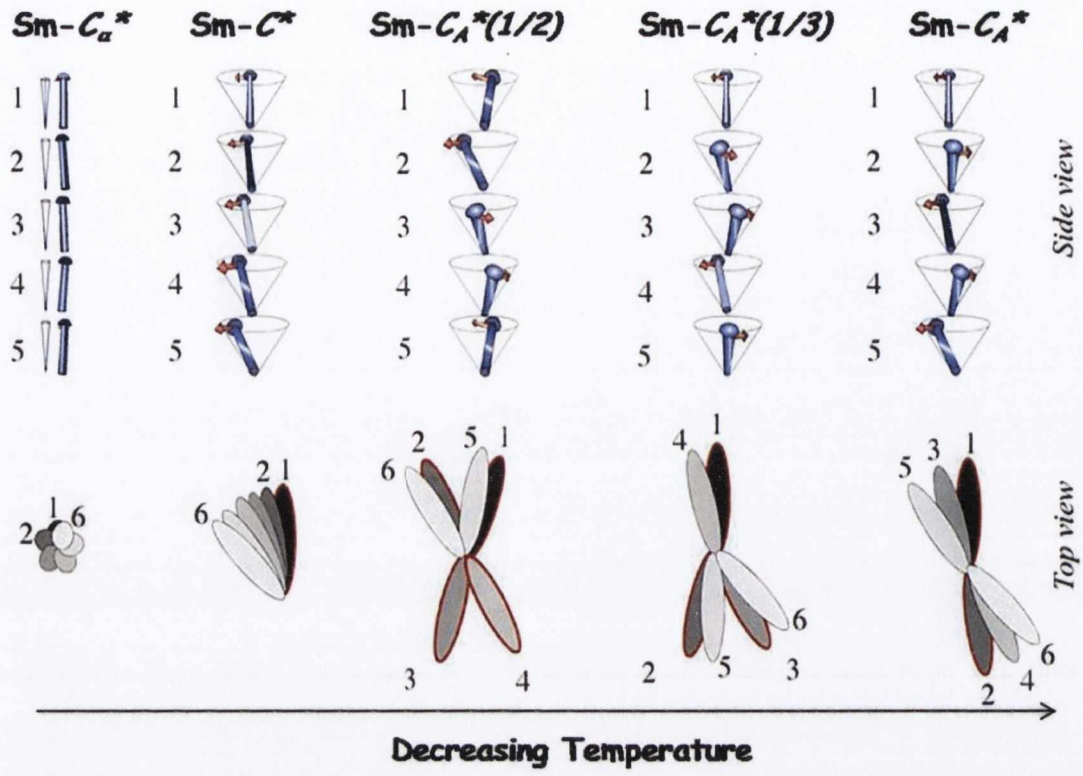

Figure 1.2: Illustrations of the director / polarization modulation in the five different chiral smectic-C phases. In the side view of five consecutive smectic layers, n is represented by a nail and P_s with red arrows. In the top view (along the smectic layer normal) the polarization is omitted and n is indicated with ellipses, the gray shade of which reflects the layer position (in both views indicated also by numbers). Since the tilt of the Sm-C_α^* phase is so small, the cone is too thin for drawing the director nail inside it, hence it has been placed next to the cone in this phase. In the other four phases the ellipses of the layers comprising one 'repeating unit' have been highlighted in the top view with thick red contours. This figure is taken from reference [5].

The Sm-C^* phase: The Sm-C^* phase is a tilted phase, i.e. all the molecules are inclined at an average temperature dependent angle (the tilt-angle) relative to the layer normal. This phase tends to form a macroscopic helical structure. The variable that changes along the helix axis is the phase-angle or azimuthal angle (often denoted by φ), i.e. the angle describing the direction towards which the molecules in a specific layer tilt. The periodicity of the helix, called the pitch p, often increases with temperature. If the helix is quenched through surface

stabilization it can become ferroelectric (Surface-Stabilized Ferroelectric Liquid Crystals; SSFLC).

The Sm-C_A^* phase: It is a chiral tilted smectic phase with no in-plane ordering and it also features the helical arrangement of the molecules. The important difference is that the Sm-C_A^* phase is anticlinic as opposed to the Sm-C^* phase which is synclinic, and thus it gives antiferroelectric properties to this phase. If the helix is quenched through surface stabilization it can become antiferroelectric (Surface-Stabilized Antierroelectric Liquid Crystals; SSAFLC).

The Sm-C_α^* phase: This phase consists of a helicoidal structure with extremely short pitch. It is obvious that, despite the extremely tight pitch, the actual difference in molecular orientation between adjacent layers is quite small, fully comparable with an ordinary Sm-C^* phase and much smaller than in Sm-$C_A^*(1/2)$, Sm-$C_A^*(1/3)$ and Sm-C_A^*.

The Sm-$C_A^*(1/2)$, Sm-$C_A^*(1/3)$ phases: These two phases in some sense represent intermediate states between synclinicity and anticlinicity. The Sm-$C_A^*(1/2)$) has a polarization-cancelling repeating unit consisting of four layers, whereas Sm-CA*(1/3) has a non-zero macroscopic polarization with a reapting unit consisting of three layers.

Recently, the existence of a biaxial subphase other than the three- and four-layer phases between the Sm-C_A^* and Sm-$C_A^*(1/3)$ phase has been confirmed by studying the Bragg reflections, the electric-field-induced birefringence, and the optical rotatory power [6, 7]. In this subphase region, a full-pitch Bragg reflection band has not been observed in the transmittance spectra at oblique incidence. The subphase exhibits clearly a finite threshold field, though lower than that in Sm-C_A^*, suggesting an antiferroelectric structure which is consistent with the absence of the full-pitch band at oblique incidence.

1.4 Different terminologies to describe chiral smectic phases

Four different shorthand schemes used for denoting the different phases of the chiral smectic-C^* family as tabulated below.

Table 1.1: Different terminologies to describe chiral smectic phases.

I	II	III	IV	V (this thesis)
Sm-C^*_α	Sm-C^*_α	Sm-C^*_α	Sm-C^*_α	Sm-C^*_α
Sm-C^*	Sm-C^*	Sm-C^*	Sm-C^*	Sm-C^*
Sm-C^*_β	Sm-$C^*_{1/4}$	AF	Sm-C^*_{FI2}	Sm-$C^*_A(1/2)$
Sm-C^*_γ	Sm-$C^*_{1/3}$	Sm-C^*_γ	Sm-C^*_{FI1}	Sm-$C^*_A(1/3)$
Sm-C^*_a	Sm-C^*_a	Sm-C^*_A	Sm-C^*_A	Sm-C^*_A

The nomenclature of the liquid crystalline phases introduced first by Isozaki *et al.* [8] is used in this thesis for the reason that the arrangement of a fraction of ferroelectric order in a unit cell is explicitly specified. They defined these as $q_T = [F]/([A] + [F]$, where $[F]$ and $[A]$ are the ferroelectric and the antiferroelectric orderings in a unit cell. Since all of these phases are closely related with SmC^*_A, they designated these as Sm$C^*_A(q_T)$. Thus Sm$C^*_A(0)$ and Sm$C^*_A(1/3)$ and Sm$C^*_A(1/2)$ are the designations for a two layer, three layer (also called SmC^*_γ and SmC^*_{FI1} by different groups) and 4-layer (called AF or SmC^*_{FI2} phases), respectively. The advantage of using Isozaki notation is that any newly discovered phase can be accommodated within the scheme whereas the other numbered designations may be misleading. Furthermore SmC^*_{FI2} is an antiferroelectric phase rather than ferrielectric phase, as may be implied by this nomenclature.

1.5 Liquid crystal order parameters

Axis of the preferred orientation of the molecules is usually characterized by the director $\mathbf{n}$. $\mathbf{n}$ has the usual vector properties except that it satisfies the physically reasonable condition $\mathbf{n} \equiv -\mathbf{n}$. The director determines only the axis of the preferred orientation of the molecules and has nothing to do with the degree of orientation.

The degree of orientation is described by the order parameter. The simplest form of order parameter is written as

$$S = \frac{1}{2}\left\langle 3\cos^2\theta - 1 \right\rangle, \tag{1.1}$$

where θ is the angle between the long axis of an individual molecule and the director. S represents the degree of orientation of the molecular long axis in nematic ordering, and is suitable for representing the ordering of nematic liquid crystals.

The ordering of a biaxial phase or the ordering of impurity molecules in nematics cannot be represented by Eq. 1.1, and requires a tensor order parameter. The simplest second rank tensor order parameter in diagonalized form can be written as [9]

$$S_{ij} = \left\langle \frac{1}{2}(3l_i l_j - \delta_{ij}) \right\rangle, \tag{1.2}$$

where l_i is the direction cosine of the director with respect to a molecular axis i. Eq. 1.2 is referred to the Saupe ordering matrix.

The non-zero components of this tensor in polar coordinates are

$$\begin{aligned} S_{xx} &= \left\langle \frac{1}{2}(3\sin^2\theta\cos^2\phi - 1) \right\rangle, \\ S_{yy} &= \left\langle \frac{1}{2}(3\sin^2\theta\sin^2\phi - 1) \right\rangle, \\ S_{zz} &= \left\langle \frac{1}{2}(3\cos^2\theta - 1) \right\rangle, \end{aligned} \tag{1.3}$$

where θ and ϕ are the coordinates for the director in the x, y, z system. Eqs. 1.2 and 1.3 are sometimes useful to express the molecular distribution, but it also expresses only uniaxial orderings of each molecular axis. For example, S_{xx} represents the extent to which x axes of molecules are aligned along the same direction. However, with these order parameter, we cannot describe whether the fluctuation of the x axis of a molecule is isotropic or hindered. Therefore, we need a better expression of the order parameter for the biaxial phases.

The tensor representation can be extended to describe the orientational ordering of biaxial molecules in a biaxial phase by introducing a fourth rank ordering tensor [10, 11]. Following the notation used in reference [10],

$$S_{\alpha\beta,ij} = \left\langle \frac{1}{2}(3l_{i,\alpha}l_{j,\beta} - \delta_{ij}\delta_{\alpha,\beta}) \right\rangle, \tag{1.4}$$

where $l_{i,\alpha}$ is the cosine of the angle between the molecule axis α and the laboratory or phase axis i. By a suitable choice of coordinates without loss of generality, the 81 components of $S_{\alpha\beta,ij}$ can be reduced to nine such that $i = j$ and $\alpha = \beta$. This is equivalent to defining three diagonal Saupe ordering matrices, one for each of the three axes, $i = X, Y, Z$.

$$S^{(i)}_{\alpha\alpha} = \left\langle \frac{1}{2}(3l^2_{i,\alpha} - 1) \right\rangle, \tag{1.5}$$

Taking the diagonal component of these three matrices allows the construction of a 3×3 matrix.

$$S^{(i)}_{\alpha\alpha} = \begin{pmatrix} S^X_{xx} & S^X_{yy} & S^X_{zz} \\ S^Y_{xx} & S^Y_{yy} & S^Y_{zz} \\ S^Z_{xx} & S^Z_{yy} & S^Z_{zz} \end{pmatrix}, \tag{1.6}$$

Note that x, y and z are the molecular axes, and X, Y and Z are the laboratory or phase axes. Hence, for example, S^X_{yy} represents the extent to which the y axis of molecules aligns along the X axis in the laboratory coordinate system.

The generalized biaxial order parameters can be defined as follows. The

long axis ordering is described by $S = S_{zz}^{Z}$, which is the same as Eq. 1.1 and S_{zz} in Eq. 1.3. The phase biaxiality for a uniaxial molecule is given by $P = S_{zz}^{X} - S_{zz}^{Y}$, which represents the anisotropic fluctuation of the molecular long axis in the laboratory coordinate, hence it is connected to the macroscopic phase biaxiality. For biaxial molecules in a uniaxial phase the biaxial order parameter is $D = S_{xx}^{Z} - S_{yy}^{Z}$, which represents the anisotropic fluctuation of the molecular long axis in molecular coordinate. D does not represent the phase biaxiality. It is also possible to define a biaxial order parameter with respect to the X and Y axes, such that $D' = S_{xx}^{X} - S_{yy}^{X}$, and $D'' = S_{xx}^{Y} - S_{yy}^{Y}$. Another biaxial order parameter $C = D' - D''$ represents a phase biaxiality induced by the hindered rotation around the molecular long axis. Thus, S, P, D and C describe the full set of the order parameters for a biaxial molecule.

These order parameters are also defined using Euler angles as

$$\begin{aligned} S &= S_{zz}^{Z} = \left\langle \frac{1}{2}(3\cos^2\theta - 1) \right\rangle, \\ D &= S_{xx}^{Z} - S_{yy}^{Z} = \left\langle \frac{3}{2}(3\sin^2\theta\cos 2\psi) \right\rangle, \\ P &= S_{zz}^{X} - S_{zz}^{Y} = \left\langle \frac{3}{2}(3\sin^2\theta\cos 2\phi) \right\rangle, \\ C &= (S_{xx}^{X} - S_{yy}^{X}) - (S_{xx}^{Y} - S_{yy}^{Y}) \\ &= \left\langle \frac{3}{2}\left[(1+\cos^2\theta)\cos 2\phi\cos 2\psi - 2\cos\theta\sin 2\phi\sin 2\psi\right] \right\rangle, \end{aligned} \tag{1.7}$$

Where θ, ϕ and ψ are the Euler's angles. These order parameters are useful for connecting the microscopic molecular properties to the macroscopic phase properties.

1.6 Landau theory of liquid-crystalline phase transitions

The expanded Landau model [12, 13] leads to the structures for various ferroelectric and antiferroelectric phases by taking the chiral terms explicitly into account. The model consists of a Landau expansion in terms of ferroelectric and antiferroelectric order parameters. Because of the chirality of the molecules, expansion includes Lifshitz invariants with respect to both order parameters as well as a bilinear coupling between them. It is assumed that the changes of the order parameters from one smectic layer to another are small and therefore the continuum approximation can be used.

The tilt of molecules in the ith layer can be described by a two-component tilt vector

$$\xi_i = (n_{ix}n_{iz}, n_{iy}n_{iz}), \qquad i = 1, 2, \tag{1.8}$$

where $n_i = (n_{ix}, n_{iy}, n_{iz})$ is the director of the even and odd layers, respectively, and the z axis is normal to the layers. In the Sm-C_A^* phase the molecules in the neighbouring layers tilt in the opposite directions, in the Sm-C^* phase tilt from one layer to another does not change. We therefore introduce two new vectors instead of ξ_1 and ξ_2.

$$\xi_a = \frac{1}{2}(\xi_1 - \xi_2), \qquad \xi_f = \frac{1}{2}(\xi_1 + \xi_2), \tag{1.9}$$

where ξ_a represents the antiferroelectric and ξ_f the ferroelectric order.

The Landau free energy density expansion in ξ_a and ξ_f can be expressed as

$$\begin{aligned} g(z) = {} & \frac{1}{2}\alpha_a\xi_a^2 + \frac{1}{2}\alpha_f\xi_f^2 + \frac{1}{4}\beta_a\xi_a^4 + \frac{1}{4}\beta_f\xi_f^4 + \frac{1}{2}\gamma_1\xi_a^2\xi_f^2 + \frac{1}{2}\gamma_2(\xi_a.\xi_f)^2 \\ & + \delta_a\left(\xi_{ax}\frac{\partial\xi_{ay}}{\partial z} - \xi_{ay}\frac{\partial\xi_{ax}}{\partial z}\right) + \delta_f\left(\xi_{fx}\frac{\partial\xi_{fy}}{\partial z} - \xi_{fy}\frac{\partial\xi_{fx}}{\partial z}\right) \\ & + \frac{1}{2}k_a\left(\frac{\partial\xi_a}{\partial z}\right)^2 + \frac{1}{2}k_f\left(\frac{\partial\xi_f}{\partial z}\right)^2, \end{aligned} \tag{1.10}$$

where α and β are the coefficients for the expansion up to the fourth order in magnitude of ξ_a and ξ_f, ∂ is the Lifshitz term (which appears as a result of the chirality of the molecules, k is the elastic constant) and γ_2 is the coupling term between the two order parameters.

Assuming that only $\alpha_a = a(T - T_{a,0})$ and $\alpha_f = a(T - T_{f,0})$ $(T_{a,0} < T_{f,0})$ are temperature dependent, a minimization of free energy (Eq. 1.10) with respect to the three parameters θ_a, θ_f and q (helical pitch) gives four types of solutions for different phases:

$$\begin{aligned} SmA^* &: \theta_a = 0, \theta_f = 0 \\ SmC^* &: \theta_a = 0, \theta_f \neq 0 \\ SmC_A^*(1/3) &: \theta_a \neq 0, \theta_f \neq 0 \\ SmC_A^* &: \theta_a \neq 0, \theta_f = 0 \end{aligned} \tag{1.11}$$

where $\theta_a = (\theta_1 - \theta_2)/2$, $\theta_f = (\theta_1 + \theta_2)/2$, and θ_i is the molecular tilt angle in the ith smectic layer.

As the temperature is lowered, the Sm-A^* phase transforms to the ferroelectric Sm-C^* phase and then to the ferrielectric Sm-$C_A^*(1/3)$ phase. In this phase the ferroelectric order parameter (ξ_f) decreases from ξ to 0 when the temperature decreases, whereas the antiferroelectric order parameter (ξ_a) increases from 0 to (ξ). In other words, the angle between the tilt vectors in the neighboring smectic layers changes from 0 to π on cooling through the Sm-$C_A^*(1/3)$ phase. This model also predicts the existence of incommensurate phases when the coupling term between the two order parameters γ_2 is not strong enough.

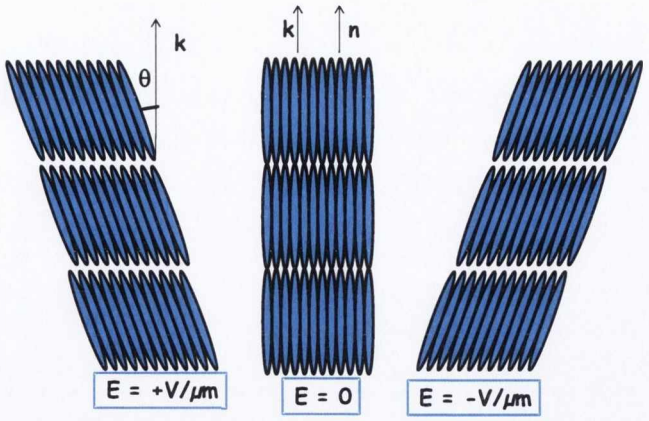

Figure 1.3: Schematic diagram of the electroclinic effect in Sm-A^* liquid crystal. The molecules are oriented normal to the layer plane in the absence of electric field. With the application of an electric field, the molecules tilt in a plane perpendicular to the electric field direction. The tilt direction is reversed on changing the E-field direction.

1.7 Electroclinic effect in liquid crystals

The chiral Sm-A^* phase is uniaxial with the long molecular axis or director **n** parallel to the smectic layer normal **k** and a two fold axis perpendicular to the molecules. The molecules are free to rotate about their long axis. If an electric field E is applied parallel to the smectic layers, this free rotation is biased due to the tendency of the transverse component of the permanent molecular dipole μ to orient parallel to the field. The system maintains a twofold axis along the electric field. In a non-chiral system, the plane containing **n** and μ is a mirror plane. However, the chirality of the phase destroys all mirror symmetries. Therefore, the free energy for molecular tilt is no longer symmetric about the $\mathbf{n}\mu$ plane and a molecular tilt is induced in a plane perpendicular to the $\mathbf{n}\mu$ plane as shown in Fig. 1.3. This linear connection between the polarization and induced tilt, discovered by Garoff and Meyer, represents the electroclinic response of the Sm-A^* phase [14, 15]. It is also referred to as the 'soft mode' in analogy with the softening of a vibration mode near the paraelectric-ferroelectric transition in solid ferroelectrics.

The electroclinic effect is demonstrated as a pretransition effect in the Sm-A^*- Sm-C^* transition. It can be described in its simplest form, in terms of Landau phenomenological description with a free energy (F) that is expressed in terms of the tilt (θ) as the order parameter and including a term to account for the coupling of the tilt to the electric field.

$$F = \frac{1}{2}a\theta^2 + \frac{1}{4}b\theta^4 - sE\theta, \tag{1.12}$$

where a, b, and s are Landau coefficients. For small values of θ, the θ^4 term can be neglected. Then the equilibrium value of θ, obtained by minimizing Eq. 1.12, is

$$\theta = \frac{sE}{\alpha(T - T_c)} \tag{1.13}$$

Here s is the chiral coupling coefficient and $a = \alpha(T - T_c)$; T_c is the Sm-A^*- Sm-C^* transition temperature and α determines the nature of this transition.

The amount of tilt induced for a given field can be defined in terms of the electroclinic coefficient, $e_c = \theta/E = s/\alpha(T - T_c)$. Clark and Lagerwall covered all aspects of the physics of the electroclinic effect [16]. Since then, molecular engineering of electroclinic material has made considerable progress, leading to the development of materials with large electroclinic coefficients, large induced tilt and small layer contraction.

1.7.1 Large electroclinic effect; Liquid crystals with small layer contraction

In most of the ferroelectric liquid crystals (FLCs) and antiferroelectric liquid crystals (AFLCs), the smectic layer normally shrinks at the transition from the Sm-A^* to Sm-C^* phase. The molecules are translationally anchored along the confining surfaces, with the period of the smectic layer spacing d_A. At the transition to the tilted Sm-C and Sm-C^* phases the layers normally start to contract while the

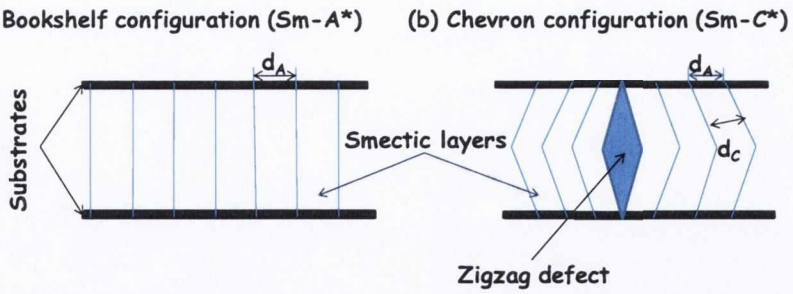

Figure 1.4: As a result of smectic layer shrinkage, a Sm-A^* sample confined between two glass substrates in the (a) bookshelf configuration transforms into the (b) chevron configuration when entering the Sm-C^* phase.

molecules at the surface preserve their anchoring. Fig. 1.4a shows the arrangement of a Sm-A or Sm-A^* phase confined between the two glass substrates of a display device in the so-called bookshelf geometry, in which the smectic layers are more or less perpendicular to the substrates. The only possibility compatible with both the surface anchoring with period d_A and the Sm-C structure with period $d_C < d_A$ is that the layers buckle into the chevron geometry shown in Fig. 1.4b. The factual existence of these chevrons was experimentally demonstrated by Rieker *et al.* in 1987 [17]. Chevrons of opposite fold direction are separated from each other by striking defects called zigzag lines. The formation of chevrons and zigzags severely degrades the quality of any electro-optic device based on FLC and AFLC materials. Probably, the only clear-cut solution to this problem is to find materials without substantial layer shrinkage in their tilted states.

However, the Sm-A^* phase of a small number of FLCs and AFLCs show an almost constant smectic layer spacing on decreasing temperature to Sm-C^* phase or increasing electric field. The understanding of why such materials do not show smectic layer shrinkage was explained by the American Scientis Adrian de Vries [18–20]. The simplest structure of the Sm-A^* phase assumes that the smectic layer spacing (d_A) is equal to the molecular length L. If we assume perfectly ordered rod-like molecules with director tilt θ, the smectic layer spacing d_C is reduced to

$$d_C = d_A cos\theta \tag{1.14}$$

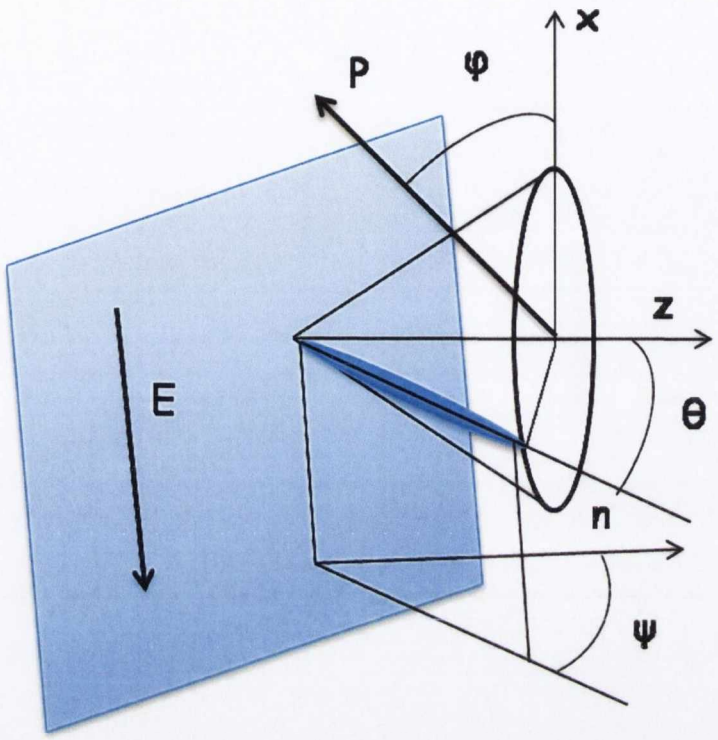

Figure 1.5: In the deVries-type Sm-A^* phase, φ is randomly distributed on the smectic tilt cone θ in the absence of fields. Applied electric field changes this distribution and induces a polarization $\mathbf{P}$, causing a reorientation ψ of the optic axis (along n) away from the layer normal z, in the plane normal to E (the electroclinic effect). In the Sm-C^* phase, φ is condensed to a single value on the cone. The director field is polarization stabilized and uniform, with an orientation controlled by the applied field.

In 1970s, x-ray experiments on Sm-A phase of a number of achiral compounds carried out by Diele *et al.* [21], suggested that the smectic layer spacing d_A is 5-10% lower than the calculated length L of the mesogenic molecules which may lead to a constant layer spacing with decreasing temperature. Based on the experimental data by Diele *at al.*, Adrian de Vries suggested that both the Sm-A and Sm-C phases are constituted from stacks of smectic layers where the molecules are tilted permanently and almost uniformly in each individual layer [18]. In this model, the tilt angle does not change in the Sm-A phase, but the direction of the tilt changes

between layers in the Sm-A phase. Since light of visible wavelength avarages over some hundred layers, the randomization of the tilt directions lead to an optically uniaxial structure with the optical axis along the layer normal as required for Sm-A phase. This explains why $d_A < L$, and since the molecules are equally tilted in the Sm-A and Sm-C phases, the model explains that $d_A \approx d_C$, that is the transition without layer shrinkage.

1.7.2 The diffuse cone model

With the recognition that the thermal orientational fluctuations of the molecules lead to a non-zero molecular inclination in all Sm-A phases, de Vries proposed the 'diffuse cone model' [19, 20]. In this model, the most probable molecular long axis orientation is tilted through a finite angle θ_A but is spatially disordered in azimuth, with a uniform distribution $f(\varphi) = 1/2\pi$ on a cone about z as shown in Fig. 1.5. The absence of macroscopic tilt in the Sm-A phase requires that the directions of the local tilt fluctuations are only short range correlated. The transition into the Sm-C phase could take place by the tilt fluctuations becoming long-range correlated in the tilt direction and simply as a result of this ordering, the macroscopic tilt appears.

If the constituent molecules are chiral, then the electro-optic behavior of a de Vries material is due to electric field (E)-induced azimuthal reorientation on the cone. Chirality couples with the local tilt to generate a polarization density $\mathbf{P}(r)$ locally normal to the tilt plane, and the resulting electrostatic energy density $u_p(r) = -\mathbf{P}(r).E$ enhances $f(\varphi)$ about $\varphi = 0$, breaking uniaxial symmetry and rotating the principal optical dielectric tensor axes away from z giving rise to a large electroclinic effect.

Recently, several authors reported that the electroclinic effect in de Vries materials is unusually large and, in addition, coupled to an increasing birefringence [5, 22–27]. It has been shown that for low layer shrinkage materials, the

electroclinic effect is observed to increase, *i.e* the same applied field at the same normalized temperature induces a higher optical tilt.

Chapter 2

Experimental techniques and relevance to liquid crystals

"In this chapter, *the details of the experimental techniques used in this thesis to study the electroclinic effect and stability of chiral smectic phases are discussed. These include (i) Polarizing Microscopy, (ii) Broadband Dielectric Spectroscopy, (iii) Optical Spectroscopy (UV-VIS-NIR), (iv) X-ray Diffraction, and (v) Polarization Measurement. These tools are very useful to investigate the properties of liquid crystals. In this thesis, the working principle of these techniques and how these techniques are used to study the liquid crystal properties will be described."*

2.1 Polarizing microscopy

The polarizing microscope is basically a regular microscope combined with a pair of polarizers and other accessories. This combination is made in order to observe the optical properties of double refracting materials such as crystals. The polarizing microscope was originally developed for investigating crystalline

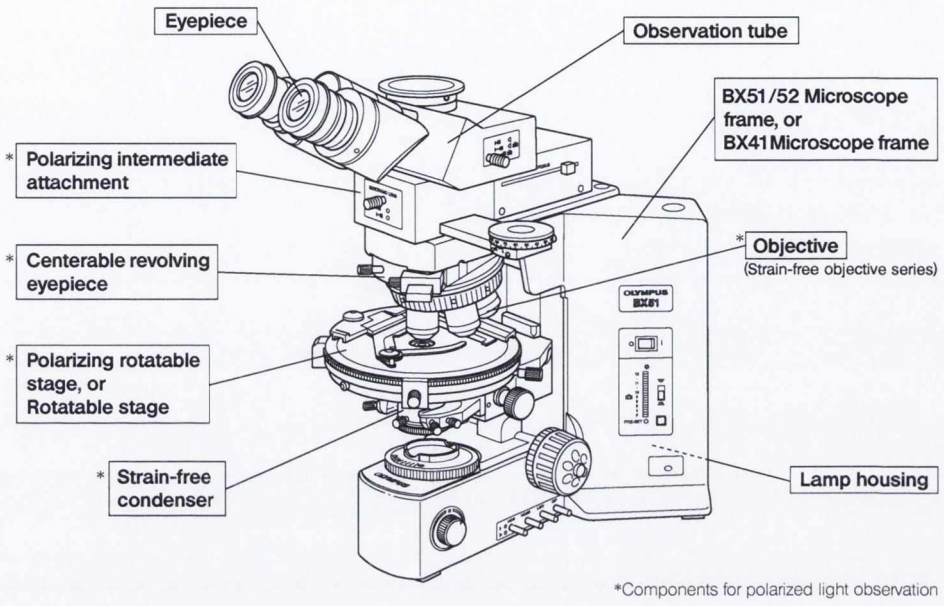

Figure 2.1: The Olympus BX51 microscope frame as depicted in the Olympus BX-51 User Manual [28].

structures within rocks and minerals. However, this microscope has now come to be used for research and examinations in medical and biological fields, as well as in such industrial fields as abestos identification, chemicals, fibres, materials, electronics, and forensics. Improved performance of the polarizing microscope combined with a full line of accessories has made it possible to perform operations such as detecting minute double refracting materials and measuring retardation. These operations were previously not possible with simple polarizing microscopes. The microscope equipment and its use in liquid crystals are described below.

2.1.1 Microscope equipment

Microscopes for examination of liquid crystal mesophases vary greatly in quality and price. Two primary considerations are made when selecting a microscope for such purposes, one the quality of the optics, and two the working space

between the stage of the microscope and the objectives and between the stage and and the illumination source. For these reasons, the Leitz Orthoplan and the Zeiss Universal polarizing microscopes are the best. However, they are also very expensive. Less expensive alternatives include the microscope shown in Fig. 2.1 - **The Olympus BX51** is used to study the liquid crystal properties in this thesis.

The Olympus BX51 polarizing microscope comprises the following sections:

I. Base: (i)Voltage Indication, (ii)Light Intensity Preset Switch, (iii)Filters

II. Focusing Block: (i)Fine Adjustment Knob, (ii)Coarse Adjustment Knob Tension, (iii)Pre-focusing Lever

II. Stage: (i)Place for the Specimen, (ii)X- and Y-Axis Knob Tension, (iii)Rotation of the Stage, (iv)Adjustment of the Stage Height

III. Observation Tube: (i)Adjustment of the Interpupillar Distance, (ii)Diopter, (iii)Eye Shades, (iv)Eyepiece Micrometer Disk, (v) Trinocular Tube

IV. Condenser

For details of how to use these control to operate the equipment effectively, one can go through the Olympus BX-51 User Manual [28].

2.1.2 The interaction of polarized light with liquid crystals

The first stage in liquid crystal characterization is the assignation of phase type and one of the primary methods of doing this is polarized light microscopy. Here, the interaction of light with liquid crystals is discussed. This is important not only for microscopy, but also for the measurement of various liquid crystalline parameters and the operation of devices.

Light is an electromagnetic wave, and liquid crystals are dielectric media. The speed of light propagating in a medium of dielectric permittivity ϵ at optical frequencies is c_0/n, where c_0 is the speed of light in vacuum and n is the refractive

index, given by

$$n = \sqrt{\epsilon} \tag{2.1}$$

A consequence of the anisotropy is that the dielectric permittivity ϵ depends upon the direction in which it is measured. In a dielectrically uniaxial anisotropic medium, the permittivity is defined by the tensor,

$$\epsilon = \begin{vmatrix} \epsilon_{\perp} & 0 & 0 \\ 0 & \epsilon_{\perp} & 0 \\ 0 & 0 & \epsilon_{ll} \end{vmatrix},$$

where $\epsilon_{\perp}$ and ϵ_{ll} are the permittivities measured perpendicular and parallel to the long molecular axis, respectively. Consequently, the speed of light wave propagating in the medium depends upon the direction in which it propagates, as determined by the refractive indices

$$n_{\perp}^2 = \epsilon_{\perp}, \qquad n_{ll}^2 = \epsilon_{ll} \tag{2.2}$$

The medium has therefore optical anisotropy. A plane polarized light propagating perpendicular to the optic axis and with its **E** vector parallel to the optic axis (see the refractive index n_{ll}). In this case, the wave is an extraordinary wave. Instead, if its **E** vector is perpendicular to the optic axis, it is an ordinary wave.

Most liquid crystals are uniaxial, or have sufficiently small optical biaxiality that it can be neglected. When a film of liquid crystal is viewed between crossed polarizers, the following two situations may arise:

A. The plane polarized light incident parallel to the molecular optic axis does not interact with the medium. Hence, the plane of polarization is unaffected and will not be passed by the analyzer - **the samle appears dark**.

B. At any other direction of incidence, the incident light will interact with the uniaxial liquid crystal film. As a result, the light will be split into two rays which propagate through the system at different velocities defined by the ordinary and

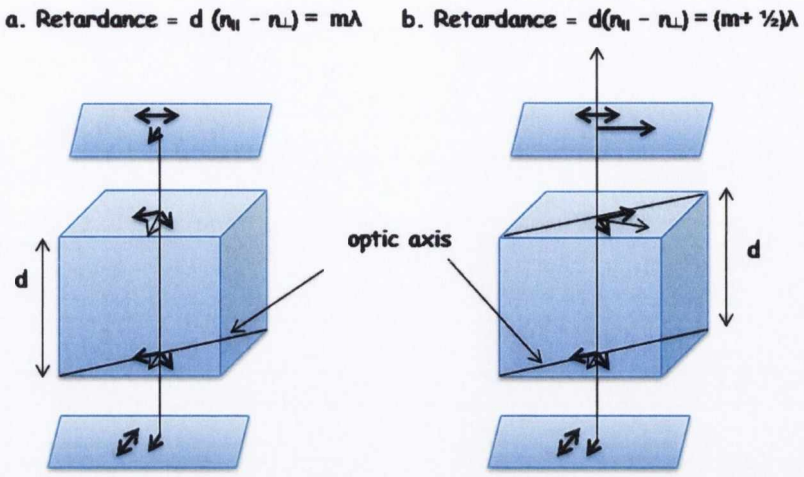

Figure 2.2: The interaction of polarized light with the liquid crystal optic axis. For (a) minimum light passes through, while for (b) maximum light passes through.

extra-ordinary refractive indices. As the two orthogonally polarized components propagate through the film a phase difference is introduced between them. Except in special circumstances, these rays combine to produce elliptically polarized light and a component of this will pass the analyzer - in general **the sample appears bright**.

To describe the second case, let us consider the diagram shown in Fig. 2.2. Light propagates normally to the crystal surface with the plane of polarization at an angle to the optic axis. On entering the sample, the light is split into two orthogonally polarized rays travelling with the ordinary or the extraordinary velocity. The two rays have a phase difference between them when they leave the slab. The extraordinary ray is retared by an amount $d(n_{ll} - n_{\perp})$, known as the retardance, with respect to the ordinary ray. $(n_{ll} - n_{\perp}) = \Delta n$ is the birefringence of the sample. Depending on the value of retardance, maximum or minimum light passes through the analyzer.

If $\Delta nd = m\lambda$, Mimimum light passes

If $\Delta nd = (m + 1/2)\lambda$, Maximum light passes

An important consequence of this is that for white light illumination, some wavelengths will not pass analyzer, whilst others do. This means that a birefringent material observed between crossed polarizers will be coloured and the colour observed depends on the retardance of the sample and its orientation between crossed polarizers. Such colours are generally known as birefringence colours and can be used to make relatively quantitative measurements of birefringence for samples of known thickness.

2.1.3 Liquid crystal texture investigations using polarizing microscopy

Liquid crystals are often observed by polarizing microscopes because they exhibit optical anisotropy. These microscopes are popular for thermotropic liquid crystal applications. Liquid crystal observations by a polarizing microscope can be divided into the following main groups:
- observation of peculiar optical textures in phase and defects of liquid crystals
- measurement of liquid crystal retardation
- judgement of whether a liquid crystal is optically positive or negative by conoscopic observation of their orientation pattern.

By observing these optical textures, the phase and defects in the liquid crystal can be investigated. Transmitted polarized light observations are also frequently performed. Liquid crystals and retardation of their orientation patterns can be measured with a compensator. It is necessary to select compensators in accordance with the size and retardation of each liquid crystal and orientation pattern. Here, observation of optical textures in smectic liquid crystals are discussed.

In the study of liquid crystals, we distinguish between the two basic sample geometries: homeotropic and planar alignment, Homeotropic alignment strictly means that the optic axis is aligned along the viewing direction, which normally means perpendicular to the sample substrate. With a Sm-A phase this is achieved when the director $\mathbf{n}$ is perpendicular to the substrate and, consequently, the smectic layers are in the substrate plane. In the case of smectic-C phases, the same

layer geometry is usually referred to as homeotropic, even though the director is no longer along the layer normal. Planar alignment is the complementary geometry to homeotropic, i.e. in the case of smectics, the layers are perpendicular to the substrates. In the Sm-A phase $\mathbf{n}$ is then in the plane of the substrate, explaining the name of this alignment type. In the smectic-C phases $\mathbf{n}$ is around a cone with half the cone angle θ. Since the vertical layers have some similarity to books in a bookshelf, planar alignment is sometimes also referred to as bookshelf geometry. However, the actual layer geometry in the smectic-C phases is generally not one with vertical layers but one where the layers fold in a chevron geometry [17]. The concept planar alignment includes bookshelf as well as chevron geometry. Sometimes planar alignment is called homogeneous alignment.

Homeotropic textures: In order to prepare homeotropically aligned samples one usually coats the substrates with a surfactant such as carboxylato chromium complexes (chromolane). The surfactant molecules adsorb with their polar head groups onto the glass, extending their non-polar tails perpendicular to the glass into the liquid crystal, which thereby tends to adopt the same type of molecule orientation, i.e. align homeotropically. An alternative way to obtain homeotropic alignment is to prepare a free-standing film; the smectic layers always form parallel to the liquid crystalair interface. When observing a homeotropically aligned SmA^* sample in the polarizing microscope, we are looking along $\mathbf{n}$ and thus along the single optic axis of this uniaxial phase. The effective birefringence is then zero and the sample looks black. In the case of the different smectic-C phases the director is tilted away from the viewing direction and a non-zero effective birefringence is possible. When the sample is chiral we are however also looking along the helix axis so the actual appearance will depend strongly on the pitch p of the helix as well as on the tilt angle θ. If p is shorter than visible light wavelengths in the medium, the effective birefringence is averaged out to zero. Such a phase will in homeotropic alignment thus look essentially identical to Sm-A^*. If p is in the range of wavelengths of visible light in the medium we will observe a phenomenon referred to as selective reflection [29, 30].

Planar textures: To ensure planar alignment one can fill the sample into a cell where the inner surfaces are coated with a thin layer of polyimide or polyamide, normally rubbed in one direction in order to impose a uniform director orientation. Most often one also achieves planar alignment (but with non-uniform layer direction) between clean glass surfaces. The texture can depend much on the thickness of the sample, with many characteristic defects developing. Uniformity in alignment is best achieved in thin cells but the phase sequence of AFLCs can be severely influenced by the confinement in case of lower cell gaps. In contrast to the case of homeotropic alignment, the Sm-C^*_α phase can here easily be distinguished from Sm-A^*, through the many ripples that appear on the focal conic domains. For the smectic-C^* phases, the phase sequence has a large impact on what the textures will look like for different phases. For non-existing Sm-C^* samples, in Sm-$C^*_A(1/2)$, Sm-$C^*_A(1/3)$ phases stripes appear along the smectic layers, reflecting the very long pitch in these phases. The stripes (often called helix unwinding lines), which are characteristics of a helicoidally modulated phase with pitch longer than visible light wavelengths, are defects through which the uniform (unwound helix) director structure at the surface is mediated with the helicoidal structure in the bulk [31]. The situation is completely different when a Sm-C^* phase is present. After the Sm-A^*-Sm-C^* transition the texture of the thick sample is divided into two types of ribbon: in one type the smectic layers have the same orientation as in Sm-A^*, in the other they fold in a horizontal chevron geometry [32]. Once the transition from Sm-C^* to Sm-$C^*_A(1/2)$ is reached the change in texture is even more drastic. The first indication of the transition is the appearance of helix unwinding lines, reflecting the long pitch in the new phase, but almost simultaneously parabolic focal conic defects [33] appear. The reason for the drastic change in texture and the appearance of the focal conic defects may be related to the horizontal chevron structure which develops in the Sm-C^* phase. Due to the layer shrinkage that the director tilt normally brings about after cooling from Sm-A^* into the Sm-C^* phase, the layers buckle into the horizontal chevron structure, in which the director still is along the rubbing direction although it is tilted with respect to the smectic layer normal.

2.2 Broadband dielectric spectroscopy

Broadband Dielectric Spectroscopy provides a powerful tool for investigating a variety of dielectric processes for both electrical and non-electrical applications. Also called Impedance Spectroscopy, the measurement separates molecular process on the basis of response time, providing a unique relaxation frequency along with a signature variation with frequency. Some common dielectric processes investigated by dielectric spectroscopy include:

- Small-molecule rotation in liquids - chemical and physical diagnostics.
- Large-molecule reorientation in polymers - physical diagnostics.
- Bulk conduction in solids and liquids and separation of electrode effects.
- Surface conduction and grain-boundary charge in porous materials.
- Interstitial ion effects in various solids.

The basic concepts including the principle of operation of broadband dielectric spectroscopy and how this is used in liquid crystals, are discussed below.

2.2.1 The dielectric spectroscopy equipment

The dielectric spectroscopy measures the impedance spectrum $Z^*(\omega)$ of a sample material arranged between two or more electrodes. One is mainly interested in the sample material properties without electrode effects. The intrinsic electric material properties like e.g. the complex permittivity $\epsilon^*(\omega)$ or conductivtiy $\sigma^*(\omega)$ spectra are evaluated from $Z^*(\omega)$. In addition to frequency, usually the $Z^*(\omega)$ dependency from additional parameters is determined. The most important one is temperature. Time, DC bias (superimposed static electrical field), ac field strength and pressure dependency are often measured, too.

Novocontrol Alpha-A Dielectric Analyzer was used to study the dielectric properties of smectic liquid crystals. The Aplha-A system set-up is shown in Fig. 2.3. The sample current is converted by the ZGS active sample cell test

Figure 2.3: Novocontrol Aplha-A system set-up

interface for the Alpha-A mainframe into two voltages from which the sample impedance is evaluated and converted to complex permittivity or conductivity by internal firmware. All system functions are controlled by the Alpha-A mainframe via high level GPIB commands provided by Novocontrol WinDETA/WinFIT software.

Low frequency analyzers < 20 MHz:

The Alpha-A modular measurement system incorporating test interfaces is used for nearly all types of direct materials and components with the impedance ranging from 0.001 to 10^{15} Ω, and $\tan(\delta) > 3 \times 10^{-5}$. The system combines features of general impedance analyzers, dielectric and electrochemical measurement systems, and extends $\tan(\delta)$ accuracy. The system is convenient for nearly all kinds of materials or components, and supports a series of high performance test interfaces with special functionality like integrated active sample cell, 4-wire high impedance measurements, high voltage / high current measurements and potentiometer, galvanometer functions for electrochemical applications.

RF impedance analyzers > 1 MHz:

At frequencies above about 10 MHz, electrical wave effects become prominent and

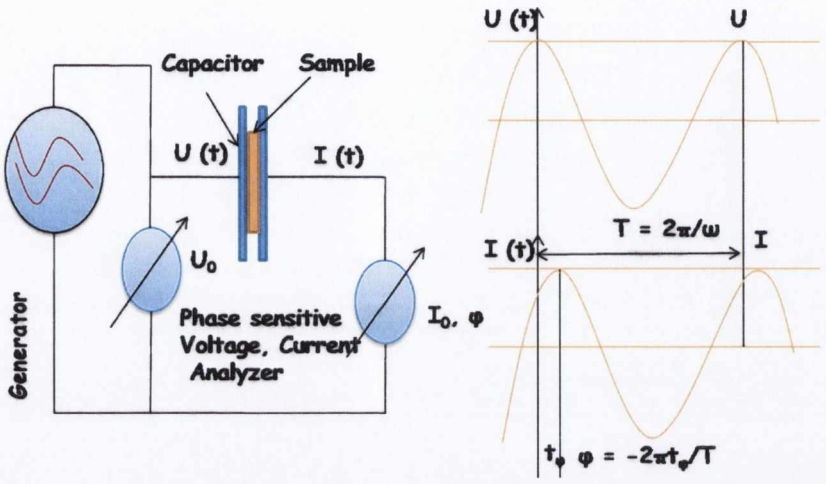

Figure 2.4: Principle of impedance measurement

microwave techniques have to be applied.

Network or RF-impedance analyzers:
Typical ranges: Frequency 1 MHz to 3 GHz, Impedance 0.1 to 10^5 Ω, $\tan(\delta) > 3\times10^{-3}$. This technique is suitable for dielectrics with large relaxation strength and conducting samples like semiconductors, electrolytes and electronic components.

2.2.2 Principle of dielectric measurement

As shown in Fig. 2.4, the basic operation is to create a sine wave at the frequency of interest, and to apply it to the dielectric sample

$$U(t) = U_0 \cos(\omega t) \tag{2.3}$$

and the resulting current

$$I(t) = I_0 \cos(\omega t + \varphi) = re(I^* \exp(j\omega t)) \tag{2.4}$$

From this, the amplitude I_0 and phase angle φ of the current harmonic base wave component $I^*(\omega)$ is calculated by complex Fourier Transform of $I(t)$ as follows:

Fourier Transform over n periods,

$$I^*(\omega) = I' + iI'' = \frac{2}{nT}\int_0^{nT} I(t)\exp(i\omega t)dt \tag{2.5}$$

$$I_o = \sqrt{(I')^2 + (I'')^2}; \quad \tan(\varphi) = \frac{I''}{I'} \tag{2.6}$$

In addition to the phase detection, the Fourier Transform suppresses all frequency components in $I(t)$ except a narrow band centered around the generator frequency. This improves accuracy and reduces noise and DC drifts by several orders of magnitude. Finally, the impedance $Z(\omega)$ and material parameters $\epsilon^*(\omega)$ and $\sigma^*(\omega)$ are calculated as follows:
The Impedance,

$$Z^*(\omega) = Z' + iZ'' = \frac{U_0}{I^*(\omega)} \tag{2.7}$$

The permittivity,

$$\epsilon^*(\omega) = \epsilon' - i\epsilon'' = \frac{-i}{\omega Z^*(\omega)}\frac{1}{C_0}, \tag{2.8}$$

where C_0 is the empty cell capacitance.

The conductivity,

$$\sigma^*(\omega) = \sigma' - i\sigma'' = \frac{-i}{Z^*(\omega)}\frac{d}{A}, \tag{2.9}$$

where d is the electrode spacing and A is the electrode area.

2.2.3 Polarization of dielectrics

Liquid crystals are dielectrics, *i.e* they have low electrical conductivity, but polarize in the presence of an electric field **E**. This means that the electric field

induces an internal charge reorganization or distortion in the material, such that a net electric dipole moment per unit volume, called the polarization **P** appears. This is a macroscopic quantity and appears as a result of different microscopic polarization machanisms, such as:

A. Charge displacement polarization: An applied electric field displaces the negative electrons in the material in one direction and the positive nuclei in the other direction. For ionic liquids, same kind of displacement occurs for negative and position ions, respectively. Even though, the displacements are very small, they produce an induced dipole moment. The value of the induced dipole moment is given by $\mathbf{P}_{dis} = \alpha \mathbf{E}_{local}$, where α is the material polarizability. Charge dislacements are very fast and thus contribute to ϵ up to very high frequencies.

B. Orientational polarization: If the molecules have permanent dipole moments, these contribute to the macroscopic polarization. However, thermal disorder of the undistributed state leads to random molecular orientations and the dipoles cancel each other. But if an electric field is applied, there will be an aligning force opposing the thermal disorder and a bias in the molecular vibrations and rotations corresponding to the partial orientation of the dipoles is created. This contribute to the macroscopic polarization.

The magnitude and direction of the polarization induced by a unit electric field is given by a tensor material parameter χ, called the dielectric susceptibility:

$$\mathbf{P} = \chi \epsilon_0 \mathbf{E}, \tag{2.10}$$

where ϵ_0 is the permittivity of free space and its value is approxiamately 8.85 $\times$ 10^{-12} C/V-m. In dielectric spectroscopy, we also deal with another material parameter called the dielectric permittivity ϵ, given by

$$\epsilon = 1 + \chi \tag{2.11}$$

The dielectric permittivity gives a simple relation to obtain the electric displacement, **D** as:

$$\mathbf{D} = \epsilon_0 \mathbf{E} + \mathbf{P} = \epsilon_0(1 + \chi)\mathbf{E} = \epsilon_0 \epsilon \mathbf{E} \tag{2.12}$$

If we know the dielectric permittivity of a material, we can obtain the field induced polarization though the following relation:

$$\mathbf{P} = \epsilon_0 \mathbf{E}(\epsilon - 1) \tag{2.13}$$

The dielectric permittivity is a macroscopic quantity and relates the external electric field **E** to the macroscopic polarization.

2.2.4 Complex dielectric permittivity; the Debye relaxation

In this section, how dielectric materials respond to steady-state and alternating electric fields will be discussed. This will bring us to the complex dielectric permittivity and the most common equation, the Debye equation, used to model the dielectric behavior at varying frequencies.

After applying a static electric field E at $t = 0$ across a dielectric, and waiting for a long time, the induced polarization P will reach its final saturation value P_f given by

$$P_f = \chi(0)\epsilon_0 E, \tag{2.14}$$

where $\chi(0)$ denotes the static (the zero stands for zero frequency) suceptibility. It is reasonable to assume that, before reaching the equilibrium value, the polarization will change at a rate which is proportional to its deviation from that value. This corresponds to the basic assumption in irreversible thermodynamics, describing how a thermodynamic variable approaches its new equilibrium value, or how a perturbation in a variable relaxes back towards equilibrium, once brough out of it

by some force [34]. We can therefore write

$$\dot{P} = \frac{P_f - P}{\tau}, \tag{2.15}$$

where $1/\tau$ is the proportionality constant, By integrating Eq. 2.15 and inserting $P = 0$ for $t = 0$, we get

$$P = P_f(1 - e^{-t/\tau}) \tag{2.16}$$

Thus, the polarization is approaching its saturation value exponentially, with a characteristic time constant τ, called the relaxation time. After reaching the saturated value of the polarization, if we turn off the field, the polarization decays to zero with the same characteristic time constant according to

$$P = P_f e^{-t/\tau} \tag{2.17}$$

If an AC electric field $E = E_0 e^{i\omega t}$ is applied to a dielectric with a given relaxation time τ, the response of the medium is dependent on frequency ω. Now, P can be written as

$$P = \chi(\omega)\epsilon_0 E \tag{2.18}$$

We assume that Eq. 2.15 is still valid at any instant. The response of the medium is now described by the frequency dependent susceptibility $\chi(\omega)$. We can find $\chi(\omega)$ by assuming that the induced polarization varies with the same frequency as the applied field as

$$P = \chi(\omega)\epsilon_0 E_0 e^{i\omega t} \tag{2.19}$$

A phase difference between E and P will be hidden in $\chi(\omega)$ which in general will be complex. Inserting Eq. 2.19 into Eq. 2.15 gives

$$i\omega P = i\omega\chi(\omega)\epsilon_0 E = \frac{\chi(0)\epsilon_0 E - \chi(\omega)\epsilon_0 E}{\tau} \tag{2.20}$$

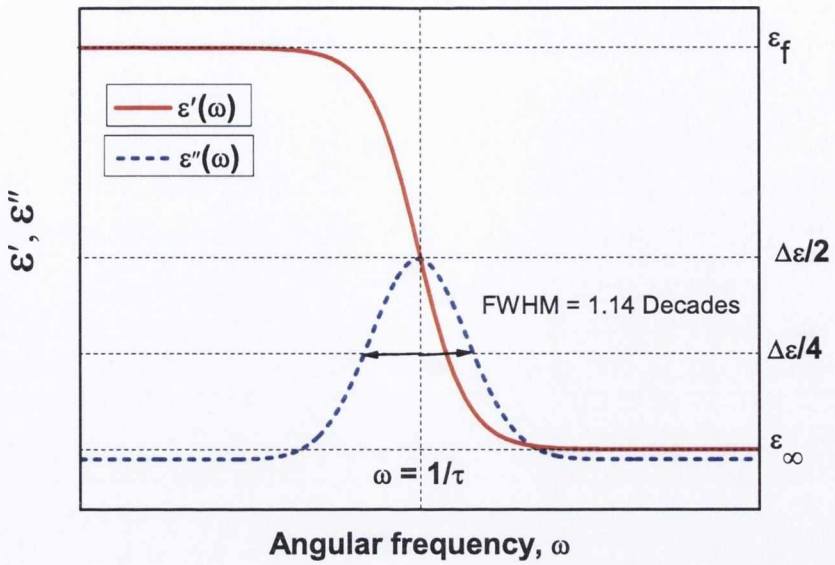

Figure 2.5: The real and imaginary parts of the Debye equation. The graphical relationships between the various parameters are shown. The loss has a peak value of $\Delta\epsilon/2$ at $\omega = 1/\tau_D$. The full width at half maximum (FWHM) is at 1.14 decades.

Hence,

$$\chi(\omega) = \frac{\chi(0)}{1 + i\omega\tau} \tag{2.21}$$

Splitting Eq. 2.21 in real and imaginary parts gives

$$\chi'(\omega) = \frac{\chi(0)}{1 + \omega^2\tau^2} \tag{2.22}$$

$$\chi''(\omega) = \frac{\omega\tau\chi(0)}{1 + \omega^2\tau^2} \tag{2.23}$$

So far one dielectric mode being excited in the medium is considered. In reality, there are several modes, often clearly seperated in absorption frequency and each giving contribution to χ' as long as the applied frequency ω is well below $1/\tau$ for the mode in question. In particular, this is true for the electronic excitations which always give a background contribution to χ' and ϵ' in dielectric spectroscopy, because their relaxation times are vanishingly small, so $\omega\tau << 1$

is always valid. Thus their high frequency contributions χ'_∞ and ϵ'_∞ (which are consequently frequency independent in our spectroscopy range) have to be added at any applied frequency. In terms of permittivity, by using $\epsilon = 1 + \chi$ and the static susceptibility $\chi(0) = \chi_f - \chi_\infty = \epsilon_f - \epsilon_\infty$, Eqs. 2.21-2.23 can be written as

$$\epsilon = \epsilon_\infty + \frac{\epsilon_f - \epsilon_\infty}{1 + i\omega\tau} \tag{2.24}$$

$$\epsilon' = \epsilon_\infty + \frac{\epsilon_f - \epsilon_\infty}{1 + \omega^2\tau^2} \tag{2.25}$$

$$\epsilon'' = \frac{\omega\tau(\epsilon_f - \epsilon_\infty)}{1 + \omega^2\tau^2} \tag{2.26}$$

This was first published by Peter Debye in 1927 [35] and a mechanism contributing to the polarization in the material in accordance with Eqs. 2.24-2.26 is called Debye-type mechanism. In the Debye equations the static susceptibility is replaced with the difference $\chi_f - \chi_\infty$ and it is often written as $\Delta\epsilon$ and referred as 'dielectric strength'. Graphs of Eqs. 2.25 and 2.26 are shown in Fig. 2.5. If we sweep the frequency ω from zero to infinity, it is seen from Eq. 2.25 that ϵ' has a practically constant value ϵ_f until ω approaches $1/\tau$. It then decreases, having an inflexion point at $\omega\tau = 1$ and becomes ϵ_∞ for $\omega\tau >> 1$. As for ϵ'', it is very small except in the neighborhood of $\omega\tau = 1$, where it has a maximum, where the absorption occurs. If several modes influence the measurement, we get several χ and f_{max} ($= \omega/2\pi$ at $\omega\tau = 1$) values, each corresponding to one contributing mechanism.

2.2.5 Non-Debye type relaxations

Often relaxation processes show a deviation from the single relaxation behavior. And it becomes impossible to obtain a good fit to the experimental data using Eqs. 2.25 and 2.26. The results of the previous analysis was modified by K.

S. Cole and R. H. Cole in 1941 as [36, 37] (given in the frequency domain form)

$$\epsilon = \epsilon_\infty + \frac{\epsilon_f - \epsilon_\infty}{1 + (i\frac{f}{f_{max}})^{(1-\alpha)}} \tag{2.27}$$

For $\alpha = 0$, this equation corresponds to Eq. 2.24. The real and imaginary parts of Eq. 2.27 can be written as

$$\epsilon' = \epsilon_\infty + [\epsilon_f - \epsilon_\infty]\frac{1 + (\frac{f}{f_{max}})^{(1-\alpha)}\sin(\frac{\alpha\pi}{2})}{1 + 2(\frac{f}{f_{max}})^{(1-\alpha)}\sin(\frac{\alpha\pi}{2}) + (\frac{f}{f_{max}})^{2(1-\alpha)}} \tag{2.28}$$

$$\epsilon'' = [\epsilon_f - \epsilon_\infty]\frac{(\frac{f}{f_{max}})^{(1-\alpha)}\cos(\frac{\alpha\pi}{2})}{1 + 2(\frac{f}{f_{max}})^{(1-\alpha)}\sin(\frac{\alpha\pi}{2}) + (\frac{f}{f_{max}})^{2(1-\alpha)}} \tag{2.29}$$

The parameter α is called the symmetric distribution parameter. The word symmetric arises because the absorption curve is symmetric with respect to the relaxation frequency, *i.e* $f = f_{max}$.

While the Cole-Cole relation correctly maps small deviations from the ideal Debye behavior, it is not adequate to represent more distorted forms of non-Debye behaviors. A further generalization was introduced by Havriliak and Negami in 1966 [38] as

$$\epsilon = \epsilon_\infty + \frac{\epsilon_f - \epsilon_\infty}{[1 + (i\frac{f}{f_{max}})^{(1-\alpha)}]^\beta} \tag{2.30}$$

The parameter β is called the asymmetric distribution parameter. The real and imaginary parts of Eq. 2.30 can be written as

$$\epsilon' = \epsilon_\infty + [\epsilon_f - \epsilon_\infty]\frac{\cos(\beta\varphi)}{[1 + 2(\frac{f}{f_{max}})^{1-\alpha}\sin\frac{\alpha\pi}{2} + (\frac{f}{f_{max}})^{2(1-\alpha)}]^{(\beta/2)}} \tag{2.31}$$

$$\epsilon'' = [\epsilon_f - \epsilon_\infty]\frac{\sin(\beta\varphi)}{[1 + 2(\frac{f}{f_{max}})^{1-\alpha}\sin\frac{\alpha\pi}{2} + (\frac{f}{f_{max}})^{2(1-\alpha)}]^{(\beta/2)}} \tag{2.32}$$

$$\varphi = \tan^{-1}\left[\frac{(\frac{f}{f_{max}})^{(1-\alpha)}\cos(\frac{\alpha\pi}{2})}{1+(\frac{f}{f_{max}})^{(1-\alpha)}\sin(\frac{\alpha\pi}{2})}\right] \tag{2.33}$$

The parameters α and β are purely empirical and there is no microscopic theory for these. For liquid crystals, the values of α is found to be very low ($\alpha << 1$), whereas the values of β are found to be close to 1.

2.2.6 Liquid crystal relaxation processes

In this section, the possible relaxation processes in chiral smectic liquid crystals will be discussed. There are two types of molecular processes; collective and non-collective processes exist in chiral smectic liquid crystals.

2.2.6.1 Non-collective processes

In order to discuss the possible non-collective relaxation processes in liquid crystals, let us consider a general case of a molecule with a permanent dipole moment which makes an angle with the long axis of the molecule. Since the order parameter is less that 1, each of the components longitudinal (μ_l) and transverse (μ_t) to the long axis has a non-zero projection both parallel and perpendicular to the molecular director **n**, resulting in four relaxations, two in each measurement geometry, **E** *ll* **n** and **E** $\perp$ **n**. The relaxation frequency connected with the rotation of μ_l observed in the cases where **E** is parallel and perpendicular to **n** are basically equal with different intensities and located in the low frequency region of the spectrum, because their rotational diffusion motion is hindered by the nematic potential. Similarly, the mechanism of μ_t which is connected with the rotation around the long axis of molecules can be observed in the two orientations with the same frequency but with different intensities. The absorption intensity of these mechanisms depends on the projection of the dipole moment in the direction of the measuring field, and on the order parameter [39].

However, because of weak intensities of some absorptions due to the reasons discussed above, we are left with two fundamental and characteristics absorptions

of non-collective types in chiral and non-chiral liquid crystal phases: one absorption observed in homeotropic orientation, which is assigned to the molecular reorientation around the short axis of the molecules. The second absorption is observed in the planar orientation, which is assigned to the molecular rotation around the long axis of the molecules.

2.2.6.2 Collective processes

Beside the non-collective processes, the dielectric spectrum of the chiral smectic liquid crystals contains two additional collective processes connected with the director fluctuations.

A. The Soft mode: In Sm-A^* phase, there exists one process assigned to the tilt fluctuation of the director, known as the soft mode. In the Sm-A^* phase the molecules are aligned in a direction parallel to the layer normal. The stability of this structure is governed by an elastic constant which keeps the long molecular axis parallel to the smectic layer normal. However, due to the thermal energy the director will be fluctuating, giving locally an instantaneous tilt angle between the director and the smectic layer normal. If the Sm-A^* phase is cooled down and allowed to approach the Sm-A^*-Sm-C^* transition temperature T_c, the elastic constant controlling the tilt fluctuation gets soft. Thus the fluctuation amplitude increases drastically and its susceptibility diverges at T_c. The softening of this elastic constant means that the phase will lose its stability gradually until it becomes unstable at T_c. When a weak electric field is applied in a direction perpendicular to the director it can easily perturb the tilt fluctuation depending on how near the system is to T_c. In the case of a non-chiral Sm-A phase the amount of induced dipole moment due to the applied electric field is too small to be detected by dielectric measurements. In the case of chiral Sm-A^*, the chirality enhances the value of the induced dipole moment due to the electroclinic effect, thus permitting the study of the soft mode dielectrically.

B. The Goldstone mode:In the Sm-C^* phase, beside director tilt fluctuations, the director is subjected to a large phase angle fluctuations, called the

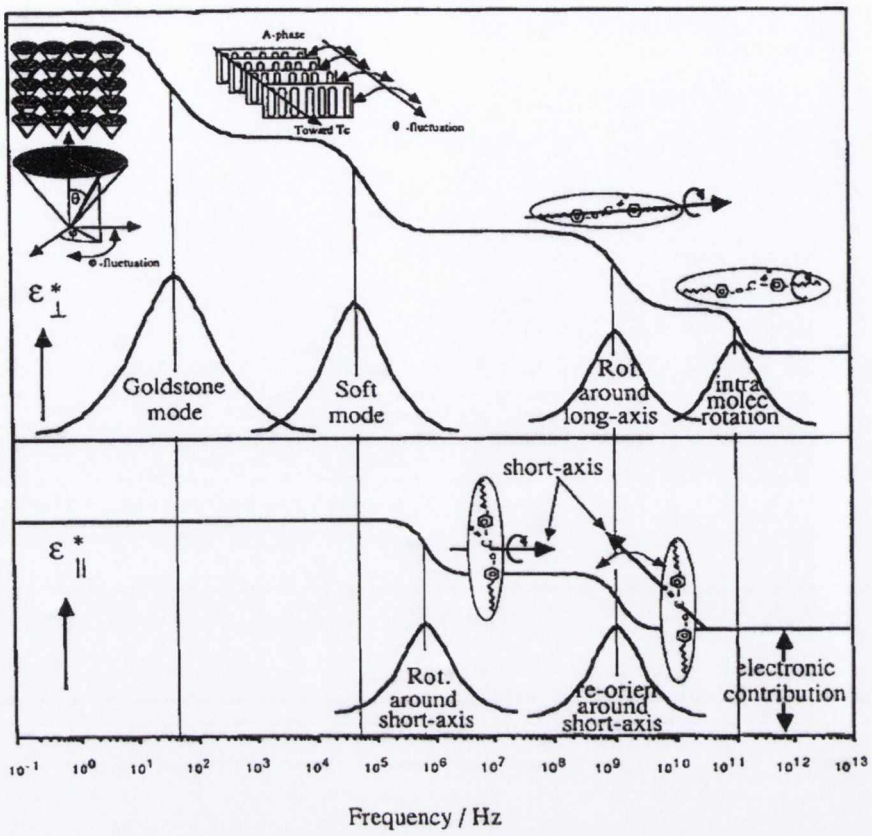

Figure 2.6: Frequency dependence of the perpendicular ($\epsilon_{\perp}$, planar cell) and parallel (ϵ_{ll}, homeotropic cell) components of the complex dielectric permittivity in the Sm-A^* and Sm-C^* phases, connected to the collective and non-collective molecular mechanisms. This figure is taken from reference [40].

Goldstone mode. The Sm-C^* is characterized by its chirality, molecular tilt and sometimes the helical structure. The director makes an angle with the smectic layer normal, and it often precesses with a finite phase angle φ from one layer to another resulting in a helical structure with helical axis parallel to the normal to the smectic layer. If we let the director in a certain layer fluctuate locally as a result of thermal excitation, then this partial reorientation will propagate along the helical axis with a long wave length. This type of fluctuation manifests itself as a distortion of the phase angle φ (the Goldstone mode in the Sm-C^* phase). In the Sm-C^* phase, both the Goldstone mode (φ-fluctuation) and the soft mode (tilt fluctuation) are present.

Fig. 2.6 illustrates the frequency dependence of real and imaginary parts of both parallel and perpendicular components of the complex dielectric permittivity.

2.2.7 Identification of chiral smectic phases using dielectric spectroscopy

Dielectric spectroscopy is used to measure the relaxation phenomena that are related to the presence of dipoles in liquid crystals. From the dielectric spectrum, information about the dynamics of the liquid crystalline molecules are deduced. A particular liquid crystal phase corresponds to a unique dielectric spectra, which in turn not only helps to identify the phase but also provide a great deal of information about structure and properties of the phase.

As described earlier, the Sm-A^* phase is characterized by divergence of the dielectric strength ($\Delta\epsilon$) and the relaxation frequency (f_{max}) as the system approaches transition towards SmC^* phase.

In the case of chiral smectic-C^* phases, the most prominent polarization process is the Goldstone mode of the helical Sm-C^* phase. Since the helix is relatively easily distorted, even a small applied electric field E will tend to align P_S along the field, thereby creating a large induced macroscopic polarization. The relaxation frequency of the Sm-C^* helix distortion mode depends on the material parameters as [41]:

$$f_{max} = \frac{2\pi K_\varphi}{\gamma_\varphi p^2} \tag{2.34}$$

where K_φ and γ_φ are the elastic constant and viscosity, respectively, relevant for phase-angle fluctuations. The strength of the mode is given by [42]:

$$\Delta\epsilon = \frac{1}{8\pi^2 K_\varphi}\left(\frac{P_s p}{\theta}\right)^2 \tag{2.35}$$

In the case of the chiral smectic-C^* phases which have a multi-layer repeating unit, the measuring field (which in dielectric spectroscopy is weak, in the mV to V range) couples not to the macroscopic polarization P_s, but to the polarization of the layers constituting the phase. Only when this is non-zero can the field induce helix distortion and therefore the Sm-$C^*_A(1/2)$ and Sm-C^*_A phases exhibit no prominent dielectric response.

In Sm-$C^*_A(1/3)$, on the other hand, the polarization is only partially cancelled out and this phase thus exhibits a helix distortion type mode. Due to the long pitch, the value of f_{max} is much lower than in the Sm-C^* phase. The strength is normally somewhat smaller than in Sm-C^*, a fact that can be attributed to the partial polarization cancellation within the repeating unit.

Since Sm-C^*_α is structurally equivalent to an extreme short-pitch Sm-C^* phase it exhibits a helix distortion mode response just like in Sm-C^*, only weaker and at much higher frequencies because of the tight pitch. Experimental observation show that the behavior is only noticed by a change in the slope of the soft mode temperature dependence [43, 44].

Experimental evidence of the relaxation processes in variant chiral smectic-C^* phases are presented and discussed in Chapter 8.

2.3 Optical spectroscopy (UV-VIS-NIR)

Optical Spectroscopy is a technique for measuring light intensity in the UV-, VIS-, NIR- and IR-region. Spectroscopic measurements are being used in many different applications, such as colour measurement, concentration determination of chemical components or electromagnetic radiation analysis.

A spectrometer instrument generally consists of an entrance slit, collimator, a dispersive element (such as a grating or prism), focusing optics and detector. In a monochromator system there is normally also an exit slit, and only a narrow

portion of the spectrum is projected on a one-element detector. In monochromators, the entrance and the exit slits are in a fixed position and can be changed in width. Rotating the grating scans the spectrum.

Development of micro-electronics during the 90's in the field of multi-element detectors, such as Charged Coupled Devices (CCD) Arrays and Photo Diode (PD) Arrays, enabled the production of low cost scanners, CCD cameras. The same CCD and PDA detectors are used in the **Avantes-2048** fiber optic spectrometers used for the experiments in this thesis, enabling fast scanning of the spectrum, without the need of a moving grating. Because of the need for fiber optics in communication technology, low absorption silica fibers have been developed. Similar fibers can be used as measurement fibers to transport light from the sample to the optical bench of the spectrometer. The easy coupling of fibers allows a modular build-up of a system that consists of a light source, sampling accessories and fiber optic spectrometer. Advantages of fiber optic spectroscopy are the modularity and flexibility of the system.

2.3.1 Spectrometer optical bench

The heart of the AvaSpec fiber optic spectrometer is an optical bench with 45, 50 or 75 *mm* focal length, developed in a symmetrical Czerny-Turner design [45].

Light enters the optical bench through a standard SMA905 connector and is collimated by a spherical mirror. A plane grating diffracts the collimated light; a second spherical mirror focuses the resulting diffracted light. An image of the spectrum is projected onto a one dimensional linear detector array. The optical bench has a number of components installed inside, allowing for a wide variety of different configurations, depending on the intended application. Sensitivity, resolution, bandwidth and stray light are further discussed in reference [45].

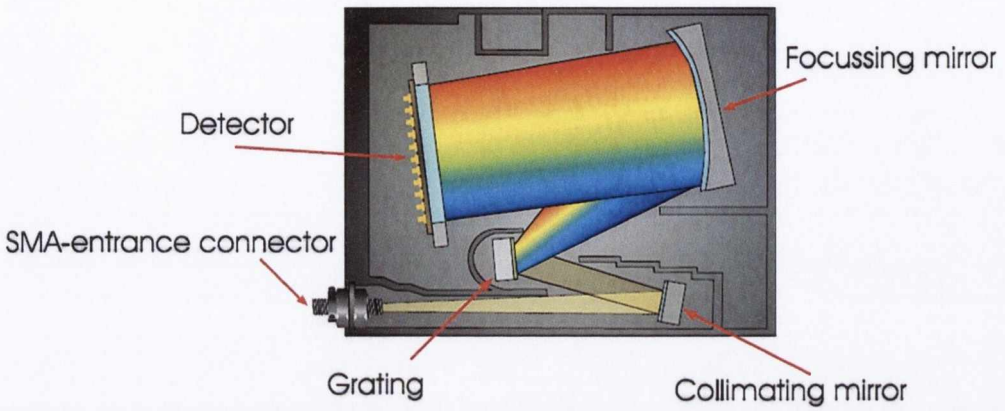

Figure 2.7: Design of the optical bench.

2.3.2 Measurement of birefringence using optical spectroscopy

The light transmitted through the cell between crossed polarizers as a function of the wavelength can be expressed as:

$$T = A \sin^2 \left(\frac{\pi \Delta n_{eff} d}{\lambda} \right) + B \tag{2.36}$$

Where A is a scaling factor that depends on the orientation of the optical axis of the cell with respect to the polarizer and the intensity of the light source, d is the cell thickness, λ is the wavelength of light, Δn_{eff} is the effective birefringence and B is an offset signal. The transmitted light was coupled into the AvaSpec-2048 optic fibre and routed to a spectrometer, which was connected to a PC where the spectrum was processed. To ensure a proper fitting, we must consider the dependence of Δn on wavelength. The extended Cauchy equation [46] was used for the fitting of the data on the transmitted intensity as a function of the

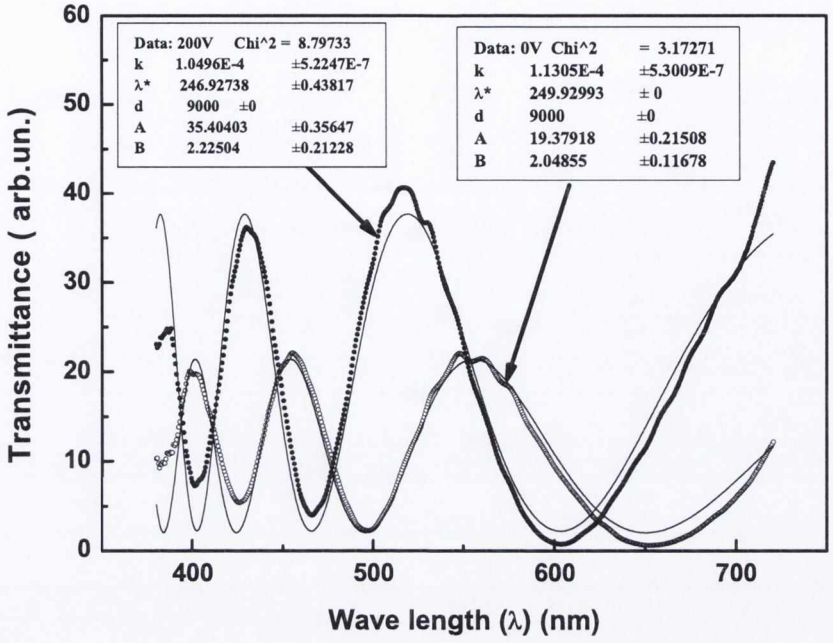

Figure 2.8: Optical Spectra and fitting curves for 0 V and 200 V.

wavelength.

$$\Delta n_{eff}(\lambda) = k_{eff}\left(\frac{\lambda^2\lambda^{*2}}{\lambda^2 - \lambda^{*2}}\right) \tag{2.37}$$

The parameters k_{eff} and λ^* were determined from the fitting of the optical spectrum at a large enough electric field. During the fitting of the optical spectra in the absence of the electric field, the dispersion parameter λ^* was fixed and the only fitting parameter was the scaling factor k_{eff}. In the absence of the electric field the effective birefringence Δn_0 is always lower than Δn, but the dispersion is the same. Therefore during the fitting of the optical spectra in the absence of the electric field, the dispersion parameter λ^* was fixed and the only fitting parameter was the scaling factor k_{eff}. From a comparison of the values of the birefringence in the undisturbed phase (without applied field) (Δn_0) and saturated birefringence (with applied field) (Δn), we may estimate the tilt angle using the expression [22]:

$$\frac{\Delta n_0}{\Delta n} \equiv \frac{k_0}{k} = 1 - \frac{3}{2}\sin^2\theta_m, \tag{2.38}$$

where $k_{eff} = k_0$ in the absence of the electric field and $k_{eff} = k$ in the presence of the electric field are obtained from the fitting of the spectra for zero and high values of the electric field respectively as shown in Fig. 2.8. Finally, we can easily determine the molecular tilt angle θ_m by using the following algebraic equation based on Eq. (2.38):

$$\theta_m = \arcsin \sqrt{\frac{2}{3}\left(1 - \frac{k_0}{k}\right)} \tag{2.39}$$

2.4 X-Ray diffraction from a set of planes

Bragg visualized the scattering of X-rays by a crystal in terms of reflections from sets of lattice planes, as shown in Fig. 2.9*a*. From one particular set of planes, constructive interference between rays reflected by successive planes will only occur when the path difference, $2d\sin\theta$, equals an integral number of wavelengths:

$$2d\sin\theta = n\lambda, \tag{2.40}$$

where d is the separation of the planes, θ is the angle of incidence, n is an integer and λ is the wavelength. Note that the diffraction angle is 2θ.

To observe a particular diffraction peak, labelled n in Fig. 2.9*b*, we must align the planes at an angle θ_n to the incident beam. The incident and diffracted beam directions are specified, as shown in Fig. 2.9*c*, by their wave vectors k_i and k_s, whose moduli are $|k_i| = |k_s| = \frac{2\pi}{\lambda}$. Note that since the scattering is elastic, the magnitudes of the wave vectors are equal. The diffracted intensity is most conveniently plotted as a function of the scattering vector $\mathbf{Q}$, where $\mathbf{Q} = (k_s - k_i)$, that is, it represents the change in wave vector of the diffracted beam. Its modulus is given by

$$|\mathbf{Q}| \equiv Q = \frac{4\pi\sin\theta}{\lambda} \tag{2.41}$$

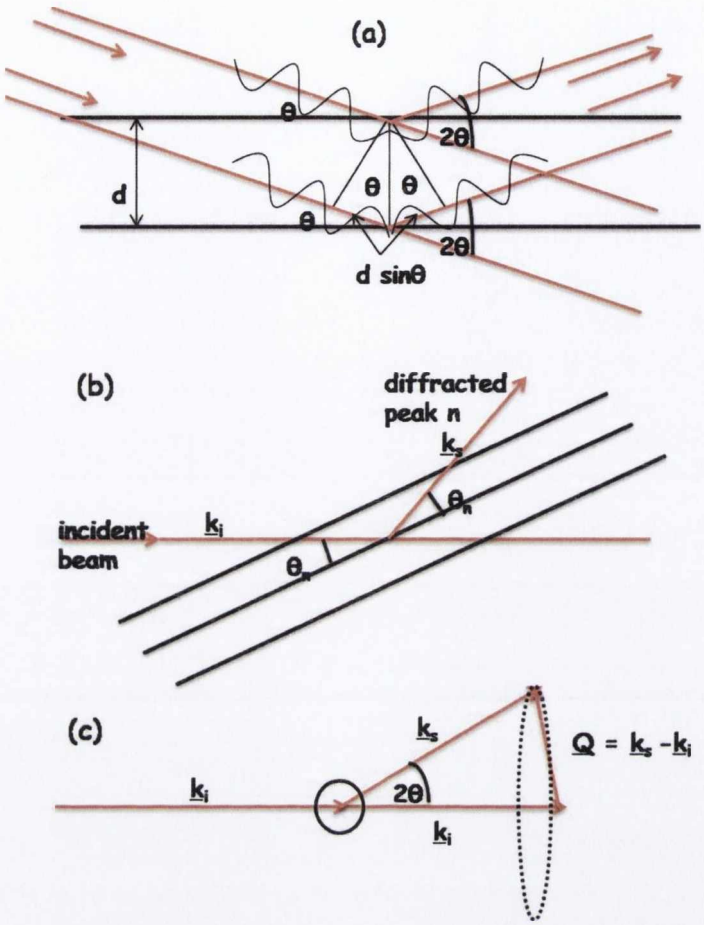

Figure 2.9: (a) Bragg's law of diffraction, (b) Reflection from parallel planes, and (c) definition of the scattering vector $\mathbf{Q}$.

An equlivalent statement of Bragg's law is then

$$Q_n = n\left(\frac{2\pi}{d}\right) \tag{2.42}$$

For a set of equally spaced planes, the scattering intensity $\mathbf{I}(\mathbf{Q})$ is everywhere zero except where Bragg's law is satisfied, and the diffraction pattern consists of a set of equally-spaced Bragg peaks, $2\pi/d$ apart, along a direction normal to the planes.

X-ray diffraction from smectic materials in device-like cells is used to determine the layer structure within the cells. X-ray diffraction can determine directly

the orientation of the layers within a cell. It has been used to demonstrate the formation of a chevron structure [17, 47] in a thin cell containing Sm-C^* material and the twisting of the layers within a cell (known as horizontal chevron formation). Many materials form a Sm-C^* on cooling from a Sm-A^* and it is believed that the reduction in layer thickness is the primary driving force for the formation of these chevron structures. Indeed, chevron formation has been observed in the Sm-A^* phase for materials whose layer thickness reduces on cooling through the Sm-A^* phase [48]. The standard method for observing the tilt of layers within a device using X-rays is to set the detector at twice the Bragg angle for the layer reflections and rotate the sample. The X-ray beam is only reflected into the detector when the angle of incidence onto the smectic layers is equal to the Bragg angle. Thus a plot of diffracted intensity vs. sample angle (known as a rocking curve) represents the distribution of layer normals as a function of their tilt angle. The original methodology has been modified to measure and display the full distribution of layer normals as a function of tilt and twist [49]. The full effect of material and boundary conditions may be seen by inspecting the layer normal distributions.

However, in this thesis the X-ray diffraction (at the Synchrotron Radiation Facility at the ESFR, France) is used only to measure the smectic layer thickness d of the Sm-A^* and Sm-C^* phases. The experimental results are discussed in Chapter 4 in proper context.

2.5 Polarization measurement in smectic liquid crystals

The major physical parameters which define the speed of response for smectic liquid crystal electro-optical devices are the polarization P_s and the rotational viscosity γ_φ. There are three basic approaches to measure the polarization: (i) the pyroelectric method [50], (ii) the Sawyer-Tower procedure [51], and (iii) a set of methods based on the measurements of the repolarization current of a liquid

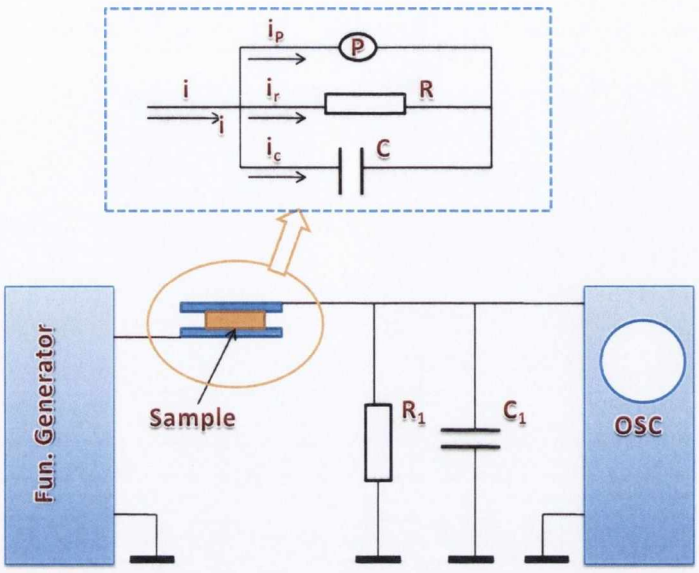

Figure 2.10: Schematic diagram of the polarization measurement system.

crystal cell [52]. The first of these approaches offers the highest accuracy for measurement of $P_s(T)$, especially for low values of polarization. But it is complicated to implement and the measurement process is time consuming. The second one is rapid but complicated to implement. The third group of methods involves measuring the area under the curve for the repolarization current and thus require additional time to process the results. In this thesis, a novel procedure is used for measuring the polarization of smectic liquid crystals, originally proposed by Vaksman and Panarin in 1992 [53]. This method allows not only to measure polarization, but additionally measures the rotational viscosity, azimuthal pretilt angle, and dielectric permittivity. Here the process of measuring the polarization in a smectic liquid crystal cell is described.

A Schematic diagram of the system used for measuring the polarization of the smectic liquid crystal cell is shown in Fig. 2.10. The current, i passing thorugh the smectic liquid crystal cell is integrated by a capacitor C_1 connected in series with the cell and a voltage generator. During measurement of the polarization P_s, a rectangular form alternating voltage was applied. Let us assume that a smectic liquid crystal is orientated in such a way that the smectic layers are perpendicular to the electrodes. When a voltage U is applied to the electrodes of the cell, the

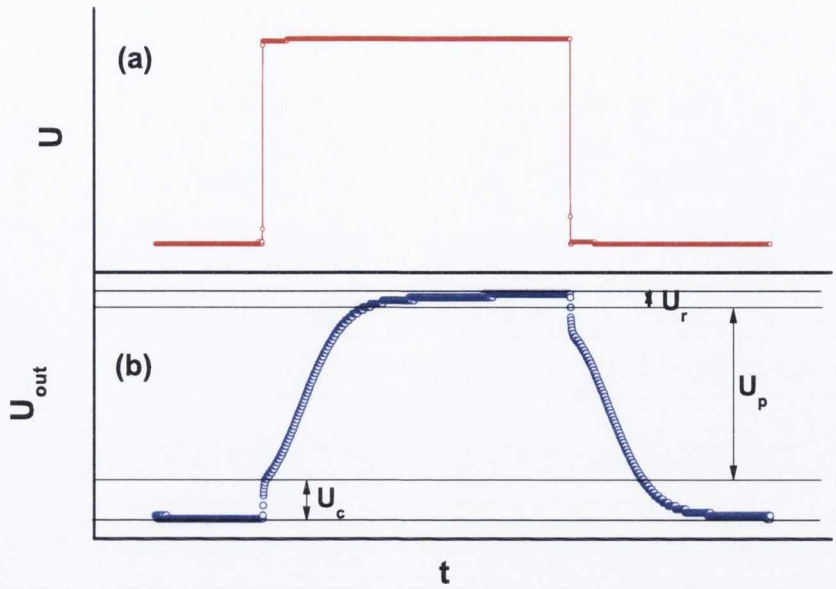

Figure 2.11: Ossilograms for (a) the driving voltage and (b) output signal from the capacitor C_1.

polarization vector tends to lie in the direction of the electric field E, while the azimuthal angle φ between them tends to zero. In the process of reorientation of P_s, there occurs a repolarization current i_p associated with the change in the surface charge on the electrodes. In addition, through the cell, there passes a current i_r which is associated with the ionic conduction of the liquid crystal. The third component is the displacement current i_c, related to the cell capacity. Thus, the instantaneous value for the total current through the cell can be presented as the the sum of three currents as:

$$i = i_r + i_c + i_p = \frac{U}{R} + C\frac{dU}{dt} + S\frac{dP_s}{dt}, \tag{2.43}$$

where C is the capacitance of the cell. d, S and R are the thickness, area and resistance of the cell, respectively. U is the applied voltage across the cell. The instantaneous value for the voltage across the capacitor C_1 will be:

$$U_{out} = -\frac{1}{C_1}\int_0^t idt = \frac{U}{RC_1}t + \frac{2UC}{C_1} + \frac{P_s S}{C_1}\cos(\varphi(t)) = U_r + U_c + U_p, \tag{2.44}$$

where t= 0 represents the moment of reversing the sign of the electric field across

the cell. Fig. 2.11 shows (a) oscillograms of the driving voltage from the function generator,a nd (b) the output voltage across the capacitor C_1. The voltage generator time constant is much shorter than the oscilloscope sweep time, as a result, the oscillogram shows U_c as an instantaneous jump. U_C is followed by a smooth growth in the voltage due to integration of the repolarization current i_p and the conductivity current i_r. i_r is due to the ionic conduction current. The effect of i_r can be eliminated by introducing a variable resistance R_1 into the measuring circuit as shown in Fig. 2.10. By measuring the value of U_p and we can find the polarization by using the formula:

$$P_s = \frac{U_p C_1}{2S} \tag{2.45}$$

The experimental results of the polarization measurements are shown in Chapter 6. Here the input capacitance of the Oscilloscope is neglected, since the input capacitance of the Oscilloscope is between 10 to 25 pF, whereas the value of C_1 is around 0.1 μF.

Chapter 3

Electro-optic properties of electroclinic liquid crystals

"In this chapter, *the results of optical texture, birefringence and tilt angle of the Sm-A^* phase exhibiting Sm-C^* and Sm-C^*_A transitions are presented. The results of optical texture, birefringence and the tilt angle measurements suggest that a part of the Sm-A^* phase is of de Vries type, since an increase in the tilt angle with decreasing temperature results in a reduction in the value of the birefringence in the Sm-A^* phase, whereas the birefringence increases significantly while making a transition to Sm-C^* phase"*

3.1 Introduction

Liquid crystalline molecules are normally translationally anchored with an almost constant smectic layer spacing within the Sm-A^* phase. At the transition from Sm-A^* to Sm-C^* or to Sm-C^*_A phases, the director tilt that induces smectic layer spacing shrinkage which starts at the transition into the Sm-C^* or Sm-C^*_A

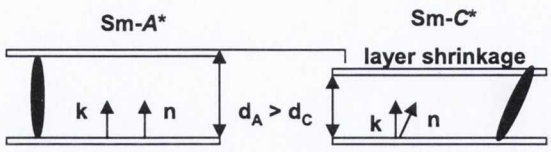

Figure 3.1: The origin of layer shrinkage at the Sm-A^*-Sm-C^* transition. At the transition from Sm-A^* to Sm-C^* phase, the director tilt induces a shrinkage in the smectic layer spacing starting at the transition into the Sm-C^* phase.

phase as shown in Fig. 3.1. This is normally the case except some exceptional cases that have been reported recently [54]. The layer shrinkage along with the surface anchoring of the molecules lead to the formation of chevrons. The chevrons of opposite fold directions are separated by zigzag defects which in turn degrade the quality of electro-optic devices based on FLCs [17, 55]and AFLCs [56, 57]. As a result, the interest in zero or low layer shrinkage materials has increased significantly due to their potential use in displays and photonic devices [58].

Recently several research groups [22–27, 59–66] observed 'de Vries-type' behavior in Sm-A^* phase using different techniques namely x-ray diffraction, electro-optical techniques, dielectric, Raman and infrared spectroscopy. But, still there are different views and models that exists in explanianing this behavior. This chapter presents the results of optical texture, optical birefringence, and the tilt angle of the Sm-A^* phase of

(*i*) an electroclinic liquid crystal (ELC) compound TSiKN65 exhibiting Sm-C^* transition,

(*ii*) an antiferroelectric liquid crystal MC-881 exhibiting Sm-C_A^* transition, and

(*iii*) mixtures of MC-881 and a ferroelectric liquid crystal MC-815, 80MC881 exhibiting Sm-C^* transition. The phase sequence of all the liquid crystal materials are presented in Table 3.1.

The results of these measurements suggest that a part of Sm-A^* phase is of de Vries-type as described in the next Sections.

3.2 Experimental details

The chemical structure of the ELC compound TSiKN65, AFLC compound MC-881 and FLC compound MC-815 [24, 67, 68], used for the experiments are shown in *Appendix-A*. For optical texture, birefringence and tilt angle measurements, in each case a cell of 9 μm thickness with planar alignment were used. The phase sequence of the materials used for the experiments and their order of transitions are shown in Table 3.1. The cells were made of two chemically etched ITO coated glass plates with sheet resistance of 30 $\Omega/\square$. For planar alignment, the conducting inner surfaces were spin coated with a polyimide RN 1175 alignment layer and rubbed parallel. The cells are filled with liquid crystals in the isotropic state and then cooled down slowly. The cells were kept in a hot stage, the temperature of which was controlled by Eurotherm-2604 temperature controller with an accuracy better than 10 mK. The hot stage was mounted on the rotating table of an Olympus microscope. The apparent tilt angle (θ_A) was measured by applying a low frequency field and rotating the sample in the polarizing microscope from the dark state to the bright state. As described in *Chapter-2*, the birefringence measurements were based on the spectral measurement of the light transmitted through the liquid crystal cell placed between the crossed polarizers [61, 63, 69]. The transmitted light was coupled into a fiber optic and routed to a AVASPEC 2024 spectrometer which was connected to a PC where the spectrum was processed.

Table 3.1: Phase sequence of the materials used for the experiments and their order of transitions.

TSiKN65	Sm-C^* $\frac{2nd}{27°C}$ Sm-A^* $\frac{1st}{57°C}$ Is
MC-881	Sm-C^*_A $\frac{1st}{112.5°C}$ Sm-A^* $\frac{1st}{120°C}$ Is
MC-815	Sm-C^* $\frac{1st}{96°C}$ Is
80MC881 (20% MC-815 + 80% MC-881)	Sm-C^* $\frac{2nd}{110°C}$ Sm-A^* $\frac{1st}{120°C}$ Is

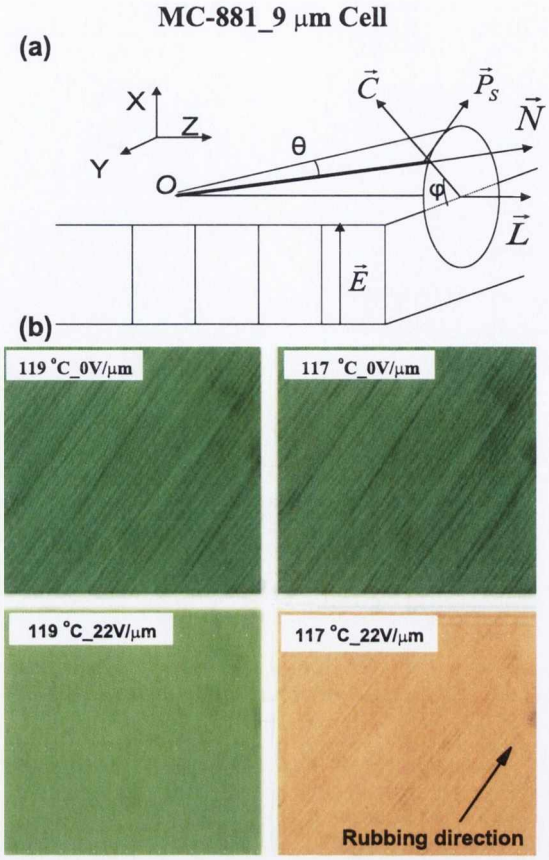

Figure 3.2: (*a*) The geometry of the studied sample. (*b*) Planar texture of MC-881 at 119 °C and 117 °C with and without applied voltage. At 119 °C, application of the external electric field yields only a change in the transmitted light intensity while the color of the texture remains about the same. At 117 °C, application of the external electric field produces a change in the birefringence, confirms the existence of the de Vries-type Sm-A^* phase.

3.3 Optical texture; Evidence of de Vries behavior

The optical textures were recorded to study the properties of Sm-A^* phase in MC-881. Fig. 3.2*a* shows the geometry of the studied sample; (X, Y, Z) is the coordinate system, N is the molecular director, L is the smectic layer normal, C is the c director, θ is the tilt angle, and φ is the azimuthal angle; the plane YZ is that of the glass plate. Fig. 3.2*b* shows micrographs for planar cells taken at two different temperatures of 119 °C and 117 °C after applying electric field of $E =$

10 $V/\mu m$ to obtaining better alignment on cooling the sample from the isotropic phase. When placed between the two crossed polarizers, the planar cell filled with the AFLC compound in the Sm-A^* phase at 119 °C shows a uniform dark green color due to a finite birefringence. The application of an electric field parallel to the smectic layer induces a thermodynamic tilt with the same symmetry as Sm-C^*. However this does not change the birefringence but only the intensity of light. As a result, there is only a change in the transmitted light intensity while the color of the texture remains almost the same. Conversely, at a lower temperature of 117 °C, the cell shows different behavior. The application of an external electric field produces a significant change in the color of the planar texture as shown in Fig. 3.2*b*. This can be explained in terms of de Vries scenario of the diffuse cone model. In the de Vries Sm-A^* phase, the molecules though significantly tilted but these are azimuthally disordered. The external electric field produces a bias in the distribution of the tilt directions with the same symmetry as Sm-C^* through an azimuthal ordering of the already tilted molecules. This results in a significantly better alignment and a change in the birefringence and therefore a change in the spectrum of the transmitted light, and change in the color of the planar texture.

The stripe texture is observed in Fig. 3.2*b* and Fig. 3.2*c* in both cases parallel to the rubbing direction. It can be suggested that these stripes are induced first at 119 °C by the electric field applied parallel to the smectic layers. These stripes possibly arise from a reduction in the smectic layer spacing due to the thermodynamic tilt by the electroclinic effect and a consequent smectic layer buckling induced by the electric field [70–72]. These stripes are rather stable and continue persisting even after the electric field is turned off in the Sm-A^* phase [70] and even in the Sm-C^* phase [73]. As observed in our experiments these stripes persist even when the sample is cooled down to Sm-C^*_A phase. This makes it almost impossible to compare a change in the stripe textures in the conventional and de Vries-type Sm-A^* phases as observed in our case.

3.4 Optical birefringence and tilt; Evidence of de Vries behavior

In this section, the results of the optical birefringence and tilt angle measurements of the Sm-A^* phase exhibiting Sm-C_A^* and Sm-C^* transitions are presented. Before doing so, let us discuss the relationship between S order parameter and the optical birefringence in the Sm-A^* phase, and the behavior of optical birefringence at the Sm-C^* or Sm-C_A^* phase while making a transition from Sm-A^* phase. These will help us a great deal in explaining the experimental observations.

3.4.1 Relationship between the order parameter and the birefringence in Sm-A^* phase

It is possible to determine the relationship between the S order parameter and the optical birefringence of the material in its Sm-A^* phase by using a general statistical theory which relates the physical properties of the molecules to the macroscopic properties of the liquid crystal phases [10, 74]. If $k_{\alpha\beta}$ is a molecular second rank tensor property, the principal componenets of which are $k_{xx}^{(m)}$, $k_{yy}^{(m)}$ and $k_{zz}^{(m)}$ defined in a molecular axis system, then using the transformation rule for second rank tensors, the property in laboratory frame is:

$$k_{\alpha\beta} = a_{\alpha\gamma} a_{\beta\delta} k_{\gamma\delta}^{(m)} \tag{3.1}$$

Ignoring the effect of molecular interactions, the macroscopic response $\chi_{\alpha\beta}$ measured in a laboratory axis frame will be the molecular property multiplied by the number density, averaged over all possible orientations of the molecules:

$$\chi_{\alpha\beta} = N \langle k_{\alpha\beta} \rangle = N \langle a_{\alpha\gamma} a_{\beta\delta} \rangle k_{\gamma\delta}^{(m)} \tag{3.2}$$

The average over which the products of direction cosine matrices contains the orientational order parameters, and in terms of the principal components $\chi_{||}^{(a)}$ and

$\chi_{\perp}^{(a)}$ of the anisotropic part of the macroscopic tensor property for the uniaxial phase become

$$\chi_{||}^{(a)} = \frac{2N}{3}[S[k_{zz}^{(m)} - \frac{1}{2}(k_{xx}^{(m)} + k_{yy}^{(m)})] + \frac{D}{2}(k_{xx}^{(m)} - k_{yy}^{(m)})] \tag{3.3}$$

$$\chi_{\perp}^{(a)} = -\frac{N}{3}[S[k_{zz}^{(m)} - \frac{1}{2}(k_{xx}^{(m)} + k_{yy}^{(m)})] + \frac{D}{2}(k_{xx}^{(m)} - k_{yy}^{(m)})], \tag{3.4}$$

where the order parameters S and D are defined as $S = \left\langle \frac{1}{2}(3cos^2\theta - 1) \right\rangle$ and $D = \left\langle \frac{3}{2}(sin^2\theta cos2\psi) \right\rangle$. Where θ and ϕ are two of the Euler's angles.

Using the results of the transformation of the second rank tensor properties as described above, the average polarizablities corresponding to the three refractive indices $\langle \alpha_{zz} \rangle, \langle \alpha_{yy} \rangle$ *and* $\langle \alpha_{xx} \rangle$ of the uniaxial phase can be expressed in terms of molecular components and orientational order parameters along the z, y and x principal axes of the electric permittivity tensor respectively.

$$\langle \alpha_{zz} \rangle = \alpha + \frac{2}{3}[\Delta\alpha S + \frac{\Delta\alpha_{\perp}}{2} D]$$
$$\langle \alpha_{xx} \rangle = \langle \alpha_{yy} \rangle = \alpha - \frac{1}{3}[\Delta\alpha S + \frac{\Delta\alpha_{\perp}}{2} D], \tag{3.5}$$

where $\Delta\alpha = \left[\alpha_{nn} - \frac{1}{2}(\alpha_{ll} + \alpha_{mm})\right]$ and $\Delta\alpha_{\perp} = (\alpha_{ll} - \alpha_{mm})$. l, m and n are the principle axes of the molecular polarizability tensor.

For anisotropic liquid crystals, the principal refractive indices can be written as

$$n_i^2 = \frac{N}{3\epsilon_o}(n^2 + 2)\langle \alpha_{ii} \rangle + 1 \tag{3.6}$$

The polarizablity component $\langle \alpha_{ii} \rangle$ is the average value along the direction of the principal refractive index n_i, and $n^2 = \frac{1}{3}(n_x^2 + n_y^2 + n_z^2)$ is the mean refractive index, where n_x, n_y and n_z are the three principal refractive indices along the three principal axes x, y and z respectively.

For uniaxial phase, the birefringence can be defined as $\Delta n = n_z - n_x$. Combining Eq. 3.5 and Eq. 3.6, we get the expression for birefringece in terms of order parameters as

$$\Delta n = n_z - n_x = \frac{N}{3\epsilon_o}\left(\frac{n^2+2}{n_z+n_x}\right)\left(\Delta\alpha S + \frac{\Delta\alpha_\perp}{2}D\right) \tag{3.7}$$

For uniaxial molecules, we can assume the angular distribution functions of the two shorter molecular axes are identical, as a result D becomes zero. Hence the expression for the birefringece can be written in terms of S order parameter as

$$\Delta n = \frac{N}{3\epsilon_o}\left(\frac{n^2+2}{n_z+n_x}\right)(\Delta\alpha S) \tag{3.8}$$

$i, e\ \Delta n \propto S$. It is shown that the S order parameter is proportional to the optical birefringence Δn for uniaxial phase.

3.4.2 Theory of optical birefringence at the Sm-A^* to Sm-C^* or Sm-C_A^* transition

The optical properties of a tilted, helicoidally modulated smectic liquid crystal in the first order can be approximated by the optical properties of an uniaxial Sm-A^* phase [75, 76]. The space-averaged dielectric tensor of the chiral ferroelectric Sm-C^* or Sm-C_A^* phase is an uniaxial tensor and given by

$$\langle\epsilon\rangle = \begin{vmatrix} \langle\epsilon\rangle_{xx} & 0 & 0 \\ 0 & \langle\epsilon\rangle_{yy} & 0 \\ 0 & 0 & \langle\epsilon\rangle_{zz} \end{vmatrix},$$

where

$$\begin{aligned}\langle\epsilon\rangle_{xx} &= \frac{1}{2}[(\epsilon_1+\epsilon_2)+(\epsilon_3-\epsilon_2)\sin^2\theta \\ \langle\epsilon\rangle_{yy} &= \frac{1}{2}[(\epsilon_1+\epsilon_2)+(\epsilon_3-\epsilon_2)\sin^2\theta \\ \langle\epsilon\rangle_{zz} &= \epsilon_3-(\epsilon_3-\epsilon_1)\sin^2\theta. \end{aligned} \tag{3.9}$$

Here, ϵ_1 and ϵ_2 are the components of the dielectric tensor of the paraelectric Sm-A^* phase in two directions perpendicular to the long molecular axis and ϵ_3 is the dielectric constant, measured along the long molecular axis. The corresponding average refractive indices are tilt angle (θ) dependent. In the limit of small tilt angles, the birefringence of the Sm-C^* phase is given by

$$\bar{n}_z - \bar{n}_x \cong (n_z - n_x) - C \quad \sin^2\theta \tag{3.10}$$

Here, C is a constant. Therefore, the birefringence of the Sm-C^* or Sm-C^*_A phase is always smaller than the birefringence of the Sm-A^* phase as found in experiments [75].

3.4.3 Experimental results for Sm-A^*-Sm-C^*_A transition

As mentioned above the de Vries materials show a large variation in the birefringence with electric field and therefore the optical spectra under an applied electric field changes. As the color changes, the spectrum peak move to a different wavelength within the range of visible light. This property can be used to determine the optical birefringence (Δn) and thermodynamic tilt angle (de Vries tilt angle, θ_{dV}) in the uniaxial Sm-A^* phase [61, 63, 69] as described in *Chapter-2.*

At a large enough electric field, the molecules of the de Vries structure are confined to $\varphi = 0$ on the smectic cone and $cos\varphi \approx 1$ and $cos^2\varphi \approx 1$ and the effective birefringence ($\Delta n \equiv \Delta n_{eff}(E_{high})$) is maximal, where φ denotes the azimuthal angle as shown in Fig. 3.2*a* . In the absence of the electric field the effective birefringence of the de Vries phase (Δn_0) is always lower than Δn, but the

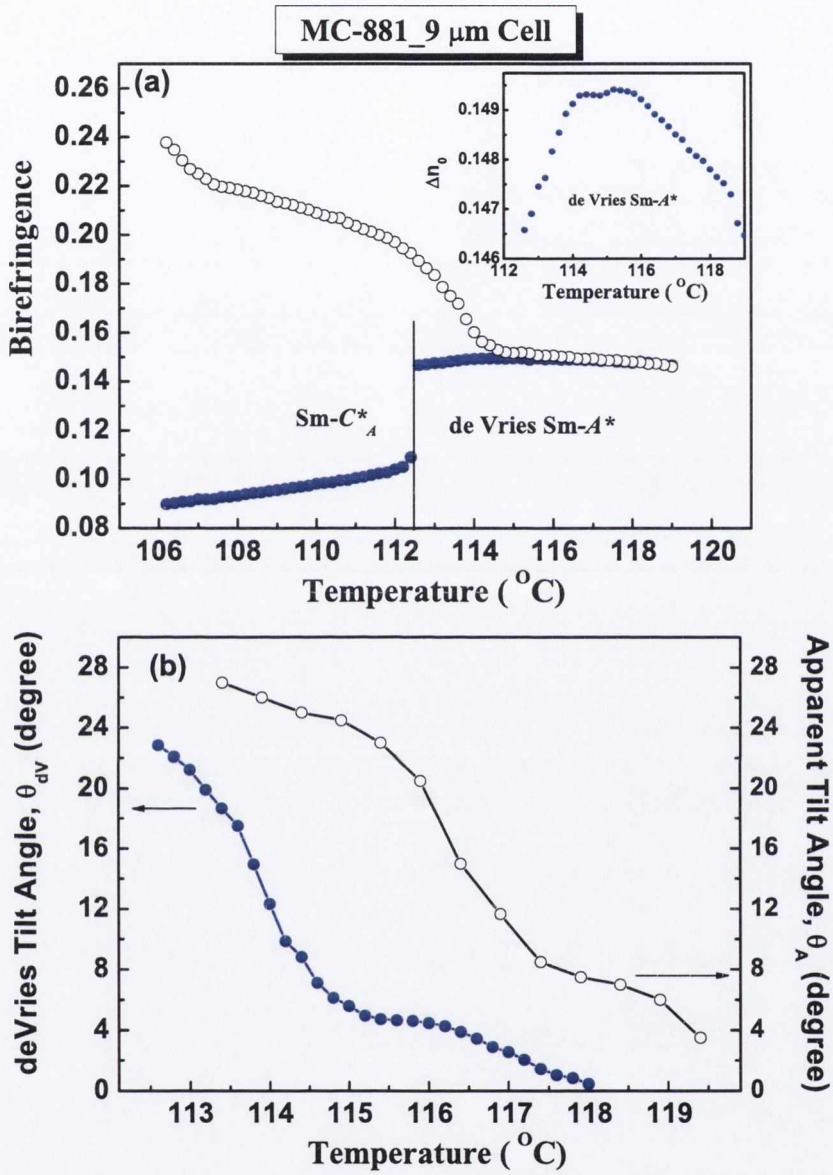

Figure 3.3: (*a*) Temperature dependence of the birefringence with and without voltage in the Sm-A^* phase and Sm-C^*_A phase. The inset in the figure shows the temperature dependence of the birefringence only within the Sm-A^* phase without voltage. (*b*) Temperature dependence of the tilt angle in the Sm-A^* phase for MC-881. The results confirm the existence of the de Vries-type Sm-A^* phase within the Sm-A^* phase.

dispersion is the same. Fig. 3.3*a* shows results of the birefringence measurement in the Sm-A^* phase of MC-881 with and without applied field. On cooling the sample from the isotropic phase to the Sm-A^* phase, in the absence of the electric field, the birefringence increases as expected, but then begins to saturate and finally begins to decrease within the Sm-A^* phase as shown in the inset in Fig. 3.3*a*. On further cooling from the Sm-A^* phase to the Sm-C_A^* phase, in the absence of the electric field, the birefringence goes down drastically near the transition and then continues to decrease slowly with decreasing temperature. The same measurements with applied voltage ($E = 22.22\ V/\mu m$) show a continuous growth of the birefringence in the entire temperature range corresponding to the Sm-A^* phase and the Sm-C_A^* phase. The birefringence is determined by the molecular distribution of the material in a phase confined within the cell. Eq. 3.8 suggests that $\Delta n \propto S$. Thus, a change in the orientational order parameter S can easily be detected by a change in the birefringence. Even in the biaxial phases, the biaxiality is usually much smaller than the birefringence, and Eq.3.8 is approximately valid. In the transition from de Vries-type Sm-A^* to Sm$-C_A^*$, the orientational order parameter may always show sudden decrease independent of the presence of the helical structure because of the anticlinic alignment between the neighboring layers.

In the temperature range corresponding to the conventional Sm-A^* phase, the birefringence increases with decreasing temperature due to an increase in the orientational order parameter. In the temperature range corresponding to the de Vries-type Sm-A^* phase, the macroscopic order parameter, measured by the birefringence is lower than in the conventional Sm-A^* phase due to molecular tilt and a distribution of the azimuthal angle. The disorder in the azimuthal angle with a tilt results in a reduction in the value of the birefringence with decreasing temperature. Furthermore, application of the electric field in the de Vries-type Sm-A^* phase, forces these molecules to align in the same direction perpendicular to the electric field, which increases the birefringence; whereas in the conventional Sm-A^* phase, an application of the electric field induces only an in-plane tilt of the in-layer director, birefringence remains the same. However, both the conventional Sm-A^* phase and de Vries-type Sm-A^* phase possess uniaxial

symmetry, there is no distinct step in the birefringence, rather it's continuous. So it's difficult to determine the exact transition temperature. The crossover point between the conventional Sm-A^* phase and de Vries-type Sm-A^* phase was determined by observing a change in the color of the planar texture with the application of maximum available external voltage field (200 V) corresponding to 22.22 $V/\mu m$. It is necessary to mention that the crossover point moves to lower temperatures with a decrease in the applied voltage. Therefore we can anticipate that it will move to higher temperatures by applying higher voltages. This means that the threshold voltage at which the de Vries structure starts to unwind strongly depends on the temperature. Therefore a crossover point is not the transition temperature between the de Vries-type Sm-A^* and the conventional Sm-A^*. It may correspond to phase transition only when unlimited (or sufficiently high) electric field is applied, which is not the case in our experiment, thus we can not determine the phase transition temperature. Moreover, we can not state whether such a transition exists in the sample or not.

The temperature dependence of the de Vries tilt angle, θ_{dV} calculated by using Eq. 2.39 and the apparent tilt angle (θ_A) are plotted in Fig. 3.3*b*. In a conventional Sm-A^* phase, the measured (apparent) tilt angle (θ_A) is mainly due to the electroclinic effect, $\theta_A = \theta_E$. In the de Vries-type Sm-A^* phase, the apparent tilt angle is due to the biasing of the molecular azimuthal distribution in the direction perpendicular to the electric field plus that caused by the electroclinic effect. Hence at a sufficiently large electric field, the apparent tilt angle must be saturated if the contribution of the electroclinic effect is small. In practice, however the apparent tilt angle continues to grow slightly with an increase in the electric field arising from the conventional electroclinic effect [24]. In de Vries-type Sm-A^* phase, we thus have: $\theta_A = \theta_{dV} + \theta_E$, where θ_{dV} is the de Vries tilt angle (thermodynamical tilt angle) and θ_E is the induced tilt angle (electroclinic tilt angle). A parameter ('tiltness') is introduced to measure the de Vries properties of Sm-A^* materials: $t_A = \theta_{dV}/\theta_A$. For conventional Sm-$A^*$ compounds, $t_A = 0$, while for ideal de Vries materials, $t_A = 1$. For MC-881, at the temperature just

above the de Vries-type Sm-A^* to Sm-C_A^* (or Sm-C^*) phase transition, we found $t_A = \theta_{dV}/\theta_A = 18.63/27 = 0.69$.

3.4.4 Experimental results for Sm-A to Sm-C^* transition

The electroclinic liquid crystal TSiKN65 and the mixture of the antiferroelectric liquid crystals MC-881 and the ferroelectric liquid crystals MC-815, 80MC881 were studied with and without applied field. The phase sequences of the compounds are shown in Table 3.1. The compounds exhibit direct Sm-A^*-Sm-C^* transition rather than Sm-A^*-Sm-C_A^* transition as in the pure antiferroelectric liquid crystalline compound MC-881. The birefringence and the tilt angle measurements based on the spectral measurements of light transmitted through the liquid crystal, and the optical textures were recorded for the samples as well.

The experimental results for TSiKN65 are shown in Fig. 3.4. Fig. 3.4*a*, Fig. 3.4*b* and Fig. 3.4*c* show the optical textures of the Sm-A^* and Sm-C^* phases on cooling the sample from isotropic phase. Fig. 3.4*d* shows the birefringence measurement with and without applied field. On cooling the cell from the isotropic to the Sm-A^* phase, in the absence of the electric field, the birefringence increases as expected, but then begins to saturate and finally begins to decrease within the Sm-A^* phase as shown in the inset in Fig. 3.4*d*, as in the case of pure AFLC, MC-881. But, on further cooling the sample from Sm-A^* to the Sm-C^* phase, in the absence of the electric field, the birefringence goes up approximately 43% near the transition temperature and then continues to decrease slowly with decreasing temperature.

The experimental results for 80MC881 are shown in Fig. 3.5. Fig. 3.5*a*, Fig. 3.5*b* and Fig. 3.5*c* show the optical textures of the Sm-A^* and Sm-C^* phases on cooling the sample from isotropic phase. Fig. 3.5*d* shows the birefringence measurement with and without applied field. On cooling the cell from the isotropic to the Sm-A^* phase, in the absence of the electric field, the birefringence increases as expected, but then begins to saturate and finally begins to decrease within the

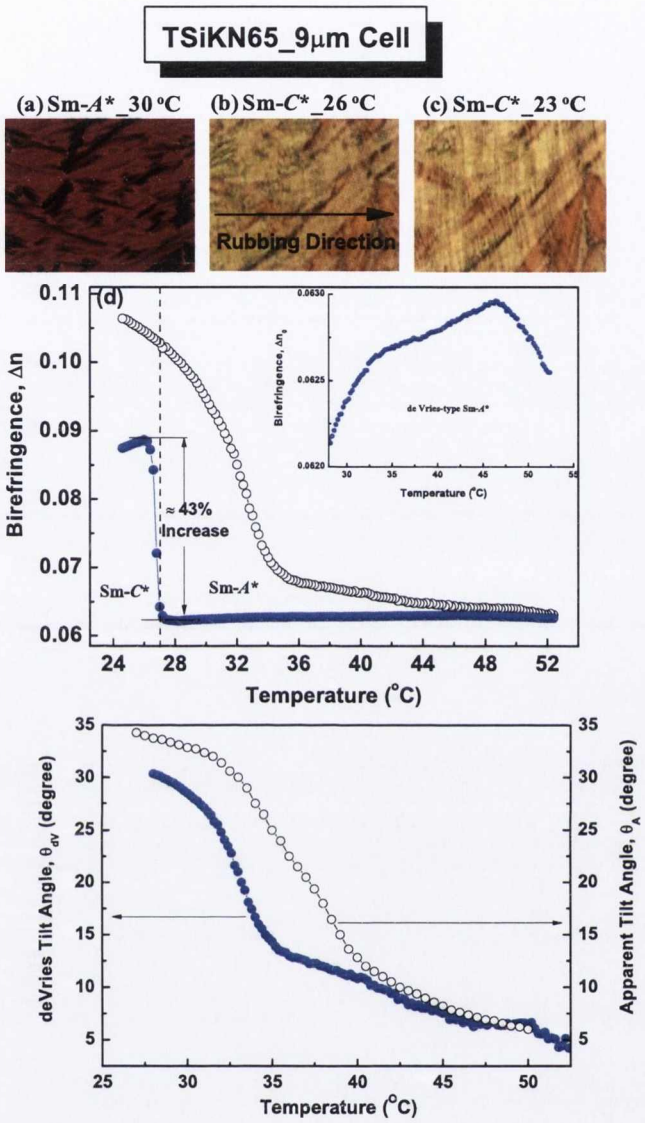

Figure 3.4: Optical textures of SmA^* phase at a temperature of 30 °C (a), SmC^* phase at 26 °C (b) and SmC^* phase at 23 °C (c). In the SmC^* phase at 23 °C, disclination lines perpendicular to the rubbing direction due to helical structure are observed, whereas at 26 °C no such lines in the SmC^* phase are observed. (d) Temperature dependence of the optical birefringence with(blue filled circle) and without (black open circle) the electric field in the SmA^* and SmC^* phases. The inset in the figure shows the temperature dependence of the birefringence only within the Sm-A^* phase without voltage. (*e*) The temperature dependence of the tilt angle in Sm-A^* phase. The results confirm the existence of de Vries-type Sm-A^* phase in TSiKN65.

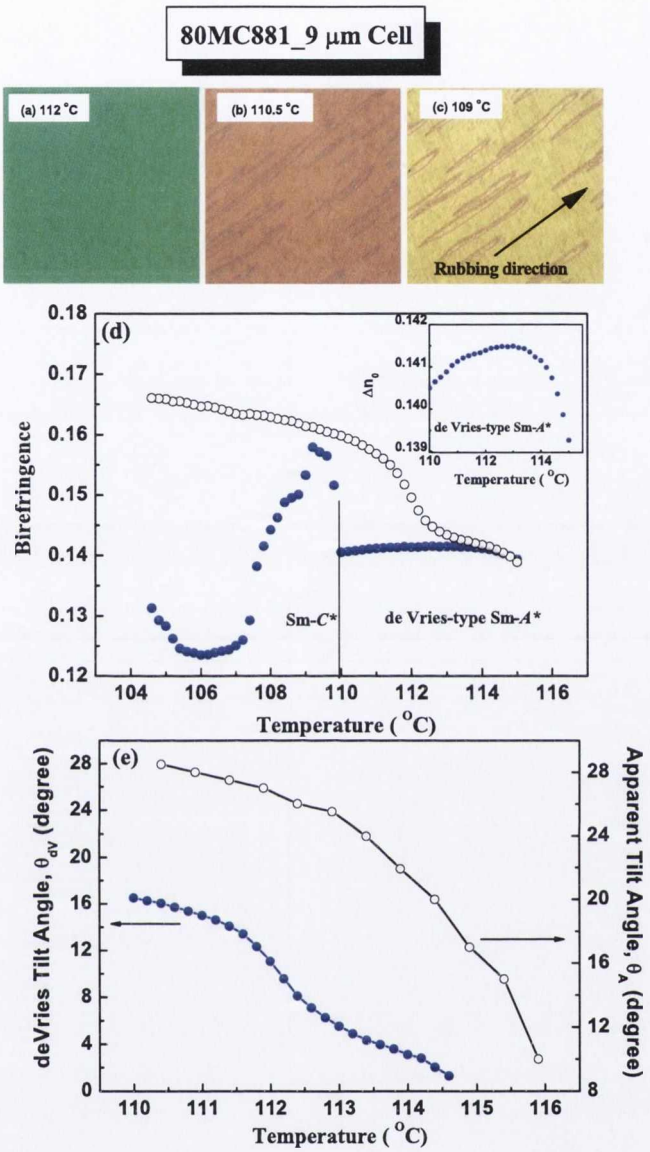

Figure 3.5: The optical micrographs of Sm-A^* phase at 112 °C (a), Sm-C^* phase at 110.5 °C (b) and the Sm-C^* phase at 109 °C (c). In the Sm-C^* phase at 109 °C (c), the disclination lines perpendicular to the rubbing direction due to helical structure are observed, whereas in the Sm-C^* phase at 110.5°C (b), there is no such line. (d) The temperature dependence of the birefringence in the Sm-A^* and Sm-C^* phases with (○) and without (•) voltage. The inset in the figure shows the temperature dependence of the birefringence only within the Sm-A^* phase without voltage. (e) The temperature dependence of the tilt angle in Sm-A^* phase. The results confirm the existence of de Vries-type Sm-A^* phase in 80MC881.

Sm-A^* phase as shown in the inset in Fig. 3.5*d*, as in the case of TSiKN65 and pure AFLC, MC-881. As in the case of TSiKN65, on further cooling the sample from Sm-A^* to the Sm-C^* phase, in the absence of the electric field, the birefringence goes up approximately 12.7% near the transition temperature and then continues to decrease slowly with decreasing temperature.

This is quite different from what is expected from a conventional Sm-A^*-Sm-C^* transition. In which case the spacial averaging of the optical properties, resulting from the helix formation, radically decreases the birefringence in the helical state as describes in *Section 3.4.2*. In the surface-stabilized state, at a conventional Sm-A^*-Sm-C^* transition, one may expect a small increase of birefringence due to the transition from a uniaxial state to a biaxial state, but the magnitude of this change is rather too small. On the other hand, the observed behavior can be very well explained by a de Vries-type Sm-A^*-Sm-C^* transition. In the transition from de Vries Sm-A^* to Sm-C^*, if the helical structure is suppressed by the surface anchoring, which is usually the case in planar cells, S order parameter hence, the optical birefringence (since i, e $\Delta n \propto S$ as described by Eq. 3.8) may show a sudden increase because the randomly distributed liquid crystalline molecules in de Vries Sm-A^* phase align along the same direction in the Sm-C^* phase. However, if the helical structure is not suppressed, S may decrease. If Sm-A^* phase is not a de Vries phase but a conventional Sm-A^* phase, S may not show any sudden change, but show a little change or a slow decrease. This explanation is confirmed by the optical textures shown in Figs. 3.4$(a-c)$- 3.5$(a-c)$, where at the transition from Sm-A^* phase (a) to the Sm-C^* phase at 23 °C of Fig. 3.4*c* of TSiKN65, and at 109 °C of Fig. 3.5*c* of 80MC881, one can see the appearance of disclination lines due to the appearance of the helical structure. The arrows in the figures represent the rubbing direction. The domain boundaries due to the surface-stabilized state appear along the rubbing direction, whereas, the disclination lines due to the helical structure appear perpendicular to the rubbing direction. But in the Sm-C^* phase at 26 °C of Fig. 3.4*b* of TSiKN65, and at 110.5 °C of Fig. 3.5*b* of 80MC881, there are no such lines. The birefringence measurement with applied voltage ($E = 22.22\ V/\mu m$) show a continuous growth of the birefringence in the

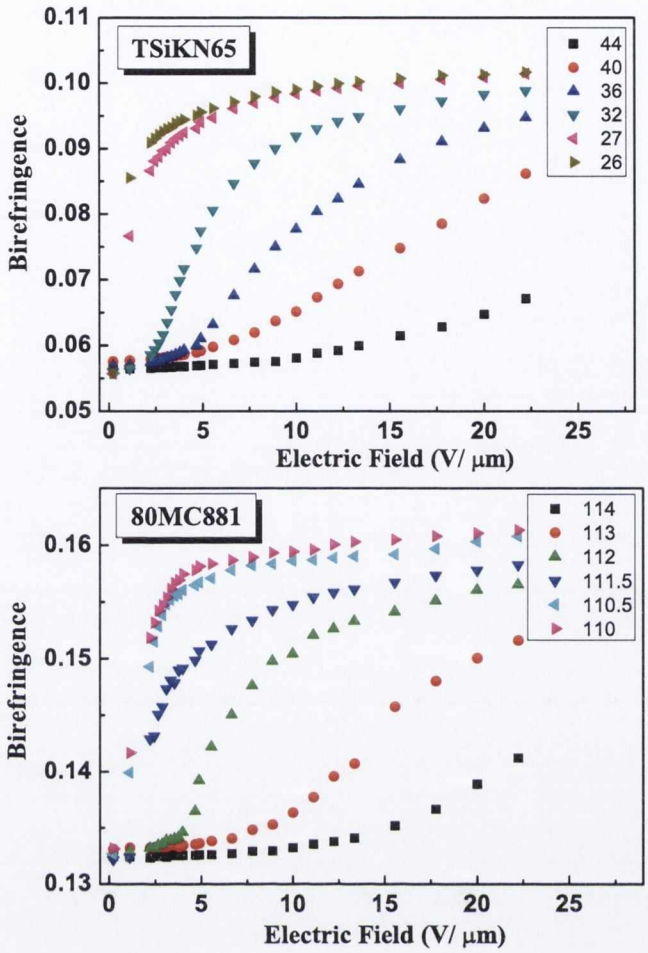

Figure 3.6: Electric field dependent birefrinfence for different temperatures in the Sm-A^* phase of TSiKN65 and 80MC881

entire temperature range corresponding to the Sm-A^* and the Sm-C^* phases, as in the case of pure AFLC, MC-881. This confirms the existence of a de Vries-type Sm-A^* phase in TSiKN65 and 80MC881. The temperature dependence of the de Vries tilt angle, θ_{dV} calculated by using Eq. 2.39 and the apparent tilt angle (θ_A) are plotted in Fig. 3.4*e* for TSiKN65 and in Fig. 3.5*e* for 80MC881 . The 'tiltness' of the de Vries-type Sm-A^* materials at the temperature just above the de Vries-type Sm-A^* to Sm-C^*) phase transition, are supposed to be $t_A = \theta_{dV}/\theta_A = 30.35/33.76 = 0.90$ for TSiKN65, and t_A $16.03/28.50 = 0.56$ for 80MC881.

The results of the electric field dependent birefringence for different temperatures in the Sm-A^* phase of TSiKN65 and 80MC881 are shown in Fig. 3.6.

The measurements show that the birefringence depends sensitively on temperature near the Sm-A^*Sm-C^* phase transition. A systematic model was developed by Selinger *et.al.* for the orientational distribution in de Vriestype materials through a series of manipulations of the dielectric tensor, which predict field dependent the optical tilt as well as the birefringence as [27] below.

For $E \rightarrow 0$,

$$\theta(0) = 0 \tag{3.11}$$

$$\Delta n(0) = \sqrt{\epsilon_a \sin^2\theta_A + \epsilon_c \cos^2\theta_A} - \sqrt{\frac{\epsilon_a \cos^2\theta_A + \epsilon_c \sin^2\theta_A + \epsilon_b}{2}} \tag{3.12}$$

For $E \rightarrow \infty$,

$$\theta(\infty) = \theta_A \tag{3.13}$$

$$\Delta n(\infty) = \sqrt{\epsilon_c} - \sqrt{\epsilon_a} \tag{3.14}$$

Here, the high-field limit shows that maximum possible birefringence, which comes from the difference between the dielectric constant ϵ_c along the long axis of the molecule and the dielectric constant ϵ_a perpendicular to the long axis. The low-field limit shows a lower birefringence, because it mixes the dielectric components in a rotational average. This model can be fitted to the ensemble of data for tilt and birefringence as functions of field and temperature. Furthermore, comparison between theory and experiment allows to extract an important theoretical parameter, the effective dipole moment, as a function of temperature. It is also found that this quantity scales as a power law near the Sm-A^*Sm-C^* transition [27]. However, in this thesis, the Langevin theory of field induced director orientation has been adopted to calculate the variation of effective dipole moment with temperature as discussed in *Chapter 6.*

3.5 Conclusions

The existence of de Vries-type Sm-A^* phase in an electroclinic liquid crystals, a pure AFLC comound and its mixtures with an FLC compound is confirmed by observing a change in the color of the planar texture with external electric field, and a reduction in the value of the optical birefringence with decreasing temperature within the Sm-A^* phase. It is also shown that at the transition temperature from de Vries Sm-A^* to Sm-C^*_A, the birefringence decreases because of the anti-clinic alignment between the neighboring layers in the Sm-C^*_A. At the transition from de Vries-type Sm-A^* to Sm-C^* phase, the birefringence increases significantly, as the helical structure is suppressed by the surface anchoring in the Sm-C^* phase. The thermodynamic tilt of the de Vries-type Sm-A^* phase are also calculated to confirm the existence of comparatively higher apparent tilt of the phase in comparison to the conventional Sm-A^* phase.

Chapter 4

X-ray diffraction study of electroclinic liquid crystals

"In this chapter, *the results of the smectic layer spacing measurements from the synchrotron radiation x-ray diffraction experiment are presented to clarify de-Vries like behavior in the mixtures of the AFLC compond MC-881 and FLC compound MC-815. The temperature dependence of the smectic layer thickness of thick free-standing films of TSiKN65 is also studied using a high-resolution film thickness measurement technique."*

4.1 Introduction

With regard to the application of liquid crystals with large electroclinic coefficient in displays, the most important characteristic of a de Vries-type material is the practical absence of layer shrinkage at the Sm-A^* to Sm-C^* transition. De Vries's 'diffuse cone' model was based on the x-ray experiments on Sm-A phase of a number of achiral compounds carried out by Diele *et al.* [21], where

the smectic layer spacing d_A was 5-10% lower than the calculated length L of the mesogenic molecules which led to a constant layer spacing with decreasing temperature. Starting in the 1990s the search for de Vries-type FLC materials led to a few compounds, the best investigated of which are TSiKN65, 3M 8422[2F3], FA-006, and PSiO-2 [5, 24, 25] where the temperature-dependent smectic layer spacings $d(T)$ was found to be much smaller than conventional Sm-A^* materials. Detailed analysis of the diffuse wide-angle x-ray scattering (WAXS) pattern, showed not only the layer spacing but also the underlying radial distribution function remained basically unchanged during the de Vries-Sm-A^* to Sm-C^* transition [25].

4.2 ID2 High brilliance beamline at ESRF

The beamline ID2 at the European Synchrotron Radiation Facility (ESRF) consists of primarily a combined small-angle and wide-angle scattering instrument [77]. The high brilliance of an undulator source is exploited to probe the microstructure and non-equilibrium dynamics of soft matter and related systems from a few Angstroms to micron scale, and down to millisecond time range.

This setup uses the monochromatic, highly collimated, and intense beam in a pinhole configuration. Combined SAXS and WAXS provide a wide q-range (0.01 nm^{-1} to 40 nm^{-1} at 0.1 nm wavelength) with high angular resolution. Both SAXS and WAXS employ area detectors, and the SAXS detector distance can be varied from 1 m to 10 m. At 10 m the q-resolution is about 0.003 nm^{-1} for a wavelength of 0.1 nm and a beam size and detector resolution of 100 μm. The high degree of collimation of the undulator beam and widely separated optical components provide a very low background. All the measured intensities can be normalised to an absolute intensity scale. The samples were contained in 1.5 mm diameter Lindemann glass tubes and their temperature was controlled by a thermostatted jet of nitrogen gas.

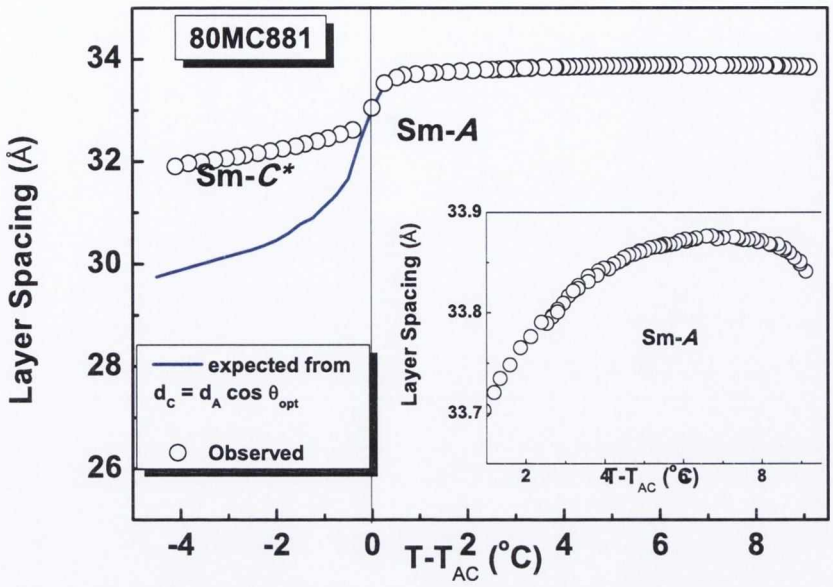

Figure 4.1: Temperature dependent smectic layer spacing d of 80MC881. The actual d values experimentally observed by SAXS are compared with the hypothetical values which are expected from the optical tilt angle in the Sm-C^* phase according to Eq. 1.14. The inset shows the temperature dependent smectic layer spacing in the Sm-A^* phase.

4.3 Variation of smectic layer spacing: Evidence of de Vries behavior

The result of the temperature dependent smectic layer spacing measurement of the sample 80MC881 is shown in Fig. 4.1. The smectic layer spacing of the compound 80MC881 is compared to the layer spacing that would be expected according to Eq. 1.14 when the optically observed tilt angle is taken into account. The comparison illustrates that the layer shrinkage is occurring in this material. However, the layer shrinkage is smaller than the shrinkage which is expected by the conventional picture of 'tilting rodlike molecules'. This confirms that the material under study (80MC881) can be classified as a 'de Vries-type' material. The inset of Fig. 4.1 shows the variation of smectic layer spacing in the temperature range corresponding to the Sm-A^* phase. Initially, the layer spacing increases with decreasing temperature due to an increase in the orientational order parameter. In the temperature range corresponding to the de Vries-type Sm-A^* phase, the

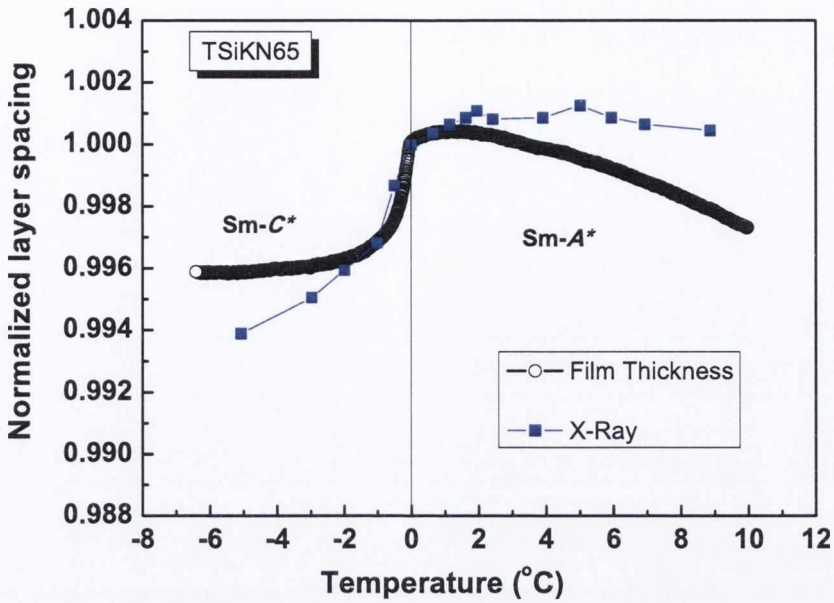

Figure 4.2: Temperature dependent smectic layer spacing of TSiKN65. The layer spacing is measured based on a high resolution film thickness measurement [78] and compared with the x-ray data of the literature [24].

macroscopic order parameter, measured by the layer spacing is lower than in the conventional Sm-A^* phase due to molecular tilt and a distribution of the azimuthal angle. The disorder in the azimuthal angle with a tilt results in a reduction in the value of the layer spacing with decreasing temperature. This is in agreement with the temperature dependent birefringence measurement in the Sm-A^* phase described in *Chapter-3*.

Among the de Vries-type materials reported to date, TSiKN65 has the lowest layer shrinkage ($\approx 0.06\%$) and is regarded as a prototype de Vries material. Fig. 4.2 shows the smectic layer spacing data of TSiKN65 measured using x-ray diffraction [24] and film thickness measurement. Recently, a high-resolution free-standing film thickness measurement technique based on using a fiber-optic spectrometer was developed in our Laboratory [78]. The liquid crystalline films are stretched across a 3 mm diameter hole drilled in a 0.3 mm thick steel plate mounted within a hot stage with a temperature resolution of 0.01 ^oC. A special algorithm gives fast and reliable fitting of the interference fringes formed on reflection from the film in order to obtain the film thickness. The optical thickness nd (where n

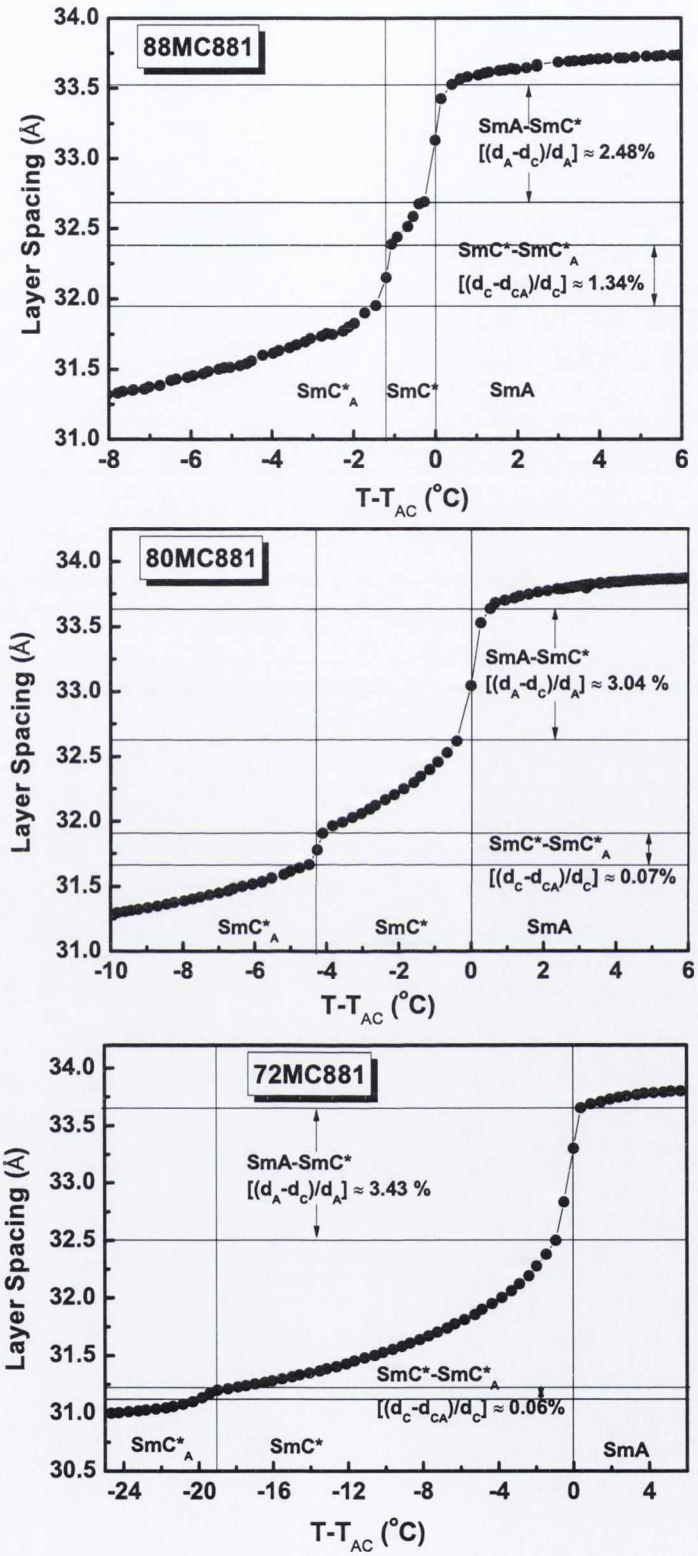

Figure 4.3: Layer shrinkage at the Sm-A^* to Sm-C^* and Sm-C^* to Sm-C^*_A transitions with increased (decreased) ferroelectric (antiferroelectric) component in the mixture.

Table 4.1: The compositions, phase sequences and order of transitions of different mixtures of MC-881 and MC-815.

88MC881 (12% MC-815 + 88% MC-881)	Sm-C_A^* $\frac{2nd}{109.3°C}$ Sm-C^* $\frac{2nd}{110.5°C}$ Sm-A^* $\frac{1st}{120°C}$ Is
80MC881 (20% MC-815 + 80% MC-881)	Sm-C_A^* $\frac{2nd}{105.7°C}$ Sm-C^* $\frac{2nd}{110°C}$ Sm-A^* $\frac{1st}{120°C}$ Is
72MC881 (28% MC-815 + 72% MC-881)	Sm-C_A^* $\frac{2nd}{89°C}$ Sm-C^* $\frac{2nd}{108°C}$ Sm-A^* $\frac{1st}{120°C}$ Is

is an effective refractive index and d is the mechanical film thickness) is measured in the range of a few tens of micrometers with a resolution better than 0.01%. The temperature dependent smectic layer spacing measured from film thicknees measurement techniqe is compared with result from x-ray diffraction in Fig. 4.2. The result confirms TSiKN65 has a negligible layer shrinkage.

4.4 Smectic layer spacing of different mixtures

Smectic layer spacing of the three different mixtures of the ALFLC MC-881 and FLC MC-815 were also studied with increased (decreased) composition of the ferroelectric (antiferroelectric) compound in the mixtures. The compositions and the phase sequences of the mixtures are shown in Table 4.1.

The results of the smectic layer spacing of the three different mixtures are shown in Fig. 4.3. For 88MC881, 80MC881 and 72MC881 the layer shrinkages at the Sm-A^* to Sm-C^* transition are around 2.5%, 3% and 3.5%, whereas the layer shrinkages at the Sm-C^* to Sm-C_A^* transition are 1.3%, 0.07% and 0.06% respectively. Hence, it is noted that with increased ferroelectric (or decreased antiferrielectric) component in the mixtures, the layer shrinkage at the Sm-A^* to Sm-C^* transition increases because of a strong coupling between the tilt and the layer thickness, whereas the layer shrinkage at the Sm-C^* to Sm-C_A^* transition decreases. These results will be useful in explaining the behavior of soft mode dielectric response and associated Landau parameters of the Sm-A^* to Sm-C^* transition of these mixtures in *Chapter* 5.

4.5 Conclusions

It has been shown that the sample 80MC881 exhibits de Vries-type Sm-A^* phase, since the layer shrinkage at the Sm-A^*-Sm-C^* transition is smaller than the shrinkage which is expected by the conventional picture of 'tilting rodlike molecules' in this material. It has also been shown that with increased ferroelectric component in the mixtures of the AFLC MC-881 and FLC MC-815, the layer shrinkage at the Sm-A^*-Sm-C^* transition increases.

Chapter 5

Dielectric properties and Landau parameters of electroclinic liquid crystals

"In this chapter, *the soft mode relaxation strength, the Landau coefficient of the temperature dependent term, and other related parameters of the de Vries-types Sm-A∗-Sm-C^*_A and Sm-A∗-Sm-C^* transitions are determined using Landau theory of the second order phase transition. For the Sm-A*-Sm-C^* transition, it is observed that the soft mode relaxation strength decreases, the Landau coefficient increases and the Curie-Weiss temperature range decreases with an increased ferroelectric composition in the mixture. These observations can be explained by the experimental observation that with increased ferroelectric composition in the mixture, the layer shrinkage at the de Vries Sm-A*-Sm-C^* transition increases. For the low layer shrinkage materials, the restoring force of the tilt-angle fluctuations is smaller, which describes the observed behavior. "*

5.1 Introduction

In the Sm-A^* phase the molecules are aligned in a direction parallel to the layer normal. The stability of this structure is governed by an elastic constant which keeps the long molecular axis parallel to the smectic layer normal. However, due to the thermal energy the director will be fluctuating, giving locally an instantaneous tilt angle between the director and the smectic layer normal. If the Sm-A^* phase is cooled down and allowed to approach the Sm-A^*-Sm-C^* transition temperature T_c, the elastic constant controlling the tilt fluctuation gets soft. Hence, for conventional Sm-A^* phase, soft-mode fluctuations are connected to the elastic energy associated with local fluctuations of the smectic layer thickness d. In contrast, for de vries-type Sm-A^* phase, the soft mode fluctuations are connected to the fluctuations in the molecular tilt directions, as a result, the soft mode strength is decoupled from variations of the layer thickness. Krueger *et. al*, showed that this is the case indeed, since remarkably strong soft-mode absorptions were observed in low layer shrinkage materials in comparison to those of conventional materials [62]. Huang *et. al*, detected quite unusual critical fluctuations in the de Vries transition a by high-resolution ac calorimetry [79]. Since fluctuations of the director tilt angle in Sm-A^* and Sm-C^* are coupled to variations in the magnitude of the spontaneous polarization, they also appear in the dielectric spectrum as a pronounced soft-mode absorption. Recently, Panarina *et al.* found two peaks in the temperature interval corresponding to the de Vries-type Sm-A^* phase [63]. They suggested one peak is the usual soft mode; whereas the other peak is due to the phase angle fluctuations.

The antiferroelectric compound MC-881 exhibiting a direct de Vries-type Sm-A^*- Sm-C^*_A transition, and its mixture with the ferroelectric compound MC-815 exhibiting a direct de Vries-type Sm-A^*- Sm-C^*, were investigated using broadband dielectric spectroscopy. The phase sequences and the order of transitions of MC-881 and MC-815, and their mixtures are shown in Table 3.1 and Table 4.1. The cells were made of two chemically etched ITO coated glass plates with sheet resistance of 30 $\Omega/\square$. For planar alignment, the conducting inner surfaces were

spin coated with a polyimide RN 1175 alignment layer and rubbed parallel. The cells are filled with liquid crystals in the isotropic state and then cooled down. Dielectric measurements in the frequency range ranging from 1 Hz to 10 MHz were carried out by using the Novocontrol Alpha High Resolution Dielectric Analyzer. During dielectric measurements, the system allowed us to superimpose dc bias voltages up to 40 V on an ac voltage of 0.03 V_{rms}.

5.2 Dielectric study of the de Vries-type Sm-A^*-Sm-C_A^* transition

5.2.1 The Soft-mode fluctuations

Fig. 5.1 shows the dependence of the dielectric relaxation strength ($\Delta\epsilon$) and the relaxation frequency (f_{max}) on temperature of MC-881 for 20 μm cell without any dc-bias voltage. The $\Delta\epsilon$ and f_{max} are found by fitting the dielectric spectra to the Havriliak-Negami equation using WINFIT fitting program. The Havriliak-Negami equation for n relaxation processes is given by

$$\epsilon^*(\omega) = \epsilon' - i\epsilon'' = \epsilon_\infty + \sum_{j=1}^{n} \frac{\Delta\epsilon_j}{[1 + (i\omega\tau_j)^\alpha]^\beta} \tag{5.1}$$

where ϵ_∞ is the high-frequency permittivity, j is a variable denoting the number of the relaxation processes up to n, τ_j is the relaxation time of jth relaxation process, α and β are the fitting parameters and $\Delta\epsilon_j$ is the dielectric relaxation strength for the jth process. In the temperature range corresponding to the de Vries-type Sm-A^* phase, only one relaxation mode (the soft mode), which corresponds to the fluctuations of the primary order parameter, the tilt angle, is detected. Whereas, in the Sm-C_A^* phase two relaxation modes are detected [80]. We will restrict ourselves to the considerations of the soft mode as we are mainly interested in the fluctuations of the tilt angle in the de Vries-type Sm-A^* phase. Sometimes there may be some differences in the soft mode fluctuations of regular and de Vries type

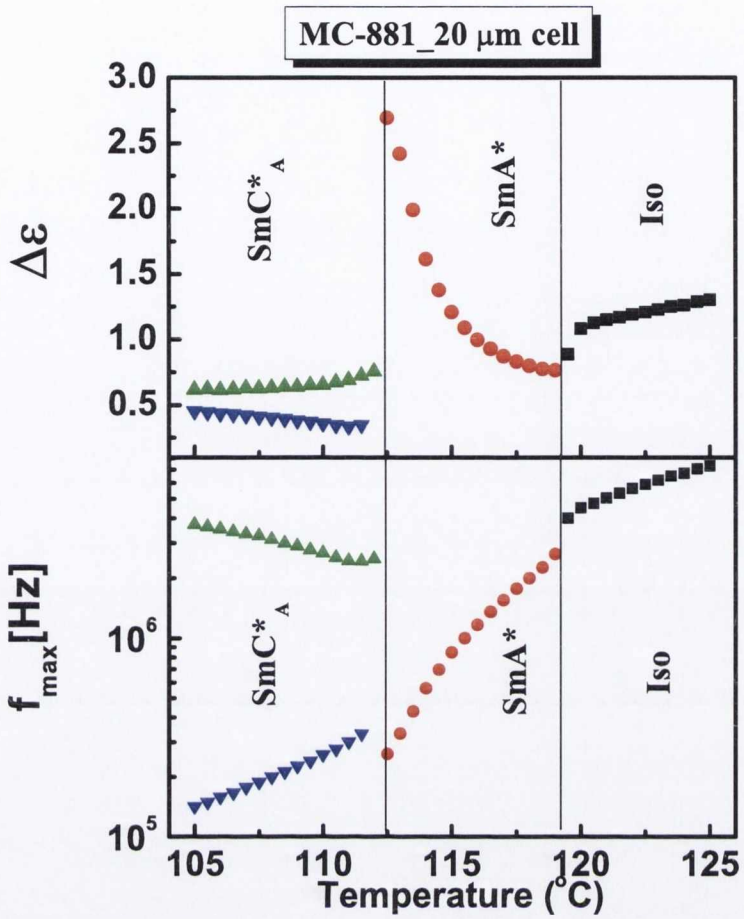

Figure 5.1: Dependence of the dielectric relaxation strength ($\Delta\epsilon$) spectra and the relaxation frequency (f_{max}) on temperature of MC-881 for 20 μm cell thickness. The collective mode appearing around the de Vries-type Sm-A^*- Sm-C^*_A transition corresponds to the fluctuations of the tilt angle of the director.

materials. Since fluctuations of the director tilt angle in the Sm-A^* and Sm-C^* are coupled to the variations in the magnitude of the spontaneous polarization, they also appear in the dielectric spectrum as a pronounced soft mode absorption.

5.2.2 The Landau Parameters

The generalized Landau expansion of the Sm-A^*-Sm-C^* transition, where the nonsingular part of the free energy, $f - f_0$, is given in the vicinity of the Sm-A^*-Sm-C^* transition by a power series expansion in terms of the primary (Θ) and

secondary (P) order parameters, proposed by Žekš in 1984 [81] is given by

$$f - f_0 = \frac{1}{2}\alpha(T - T_c)\Theta^2 + \frac{1}{4}b\Theta^4 + \frac{1}{6}c\Theta^6 - CP\Theta + \frac{1}{2\chi\epsilon_0}P^2 - \frac{1}{2}\Omega P^2\Theta^2 + \frac{1}{4}\eta P^4 - PE \tag{5.2}$$

The first three terms represent the free energy of the Sm-C^* phase with Landau coefficients α, b and c. The polarization-tilt coupling is reflected in the bilinear ($-CP\Theta$) and biquadratic ($-\Omega P^2\Theta^2/2$) coupling terms, introducing the coefficients C and Ω. The $P^2/2\chi\epsilon_0$ term is entropic in origin, related to a decrease in the entropy due to the polar ordering in the material. The last term describes the contribution due to a nonzero electric field. The individual properties of a certain ferroelectric material are reflected by its Landau expansion coefficients, *i,e.*, α, b, c, C, χ and Ω in the above equation.

The temperature dependence of the soft-mode relaxation frequency and the dielectric strength in the Sm-A^* phase on approaching the Sm-A^*-Sm-C^* transition can be calculated from the above free energy expression as [82]

$$f_{max} = \frac{\alpha(T - T_c)}{2\pi\gamma}, T > T_c \tag{5.3}$$

$$\Delta\epsilon_s = \frac{\epsilon_0(\chi_f C_f)^2}{\alpha(T - T_c)}, T > T_c, \tag{5.4}$$

where f_{max} and $\Delta\epsilon_s$ are the relaxation frequency and the dielectric strength of the soft mode, α is the Landau coefficient of the temperature dependent term in the free energy expression, γ is the viscosity connected with the soft mode, supposed to be temperature independent, ϵ_o is the permittivity of free space, χ_f is the susceptibility of the ferroelectric amplitude mode, C_f is the coupling constant between the polarization and the tilt angle of the ferroelectric amplitude mode, T_c is transition temperature of Sm-A^*-Sm-C^* transition, defined as the frequency for which $1/\Delta\epsilon_s$ is a minimum. Eq. 5.4 shows that in the Sm-A^* phase, the inverse of the dielectric strength ($1/\Delta\epsilon_s$) varies linearly with temperature, called the Curie-Weiss

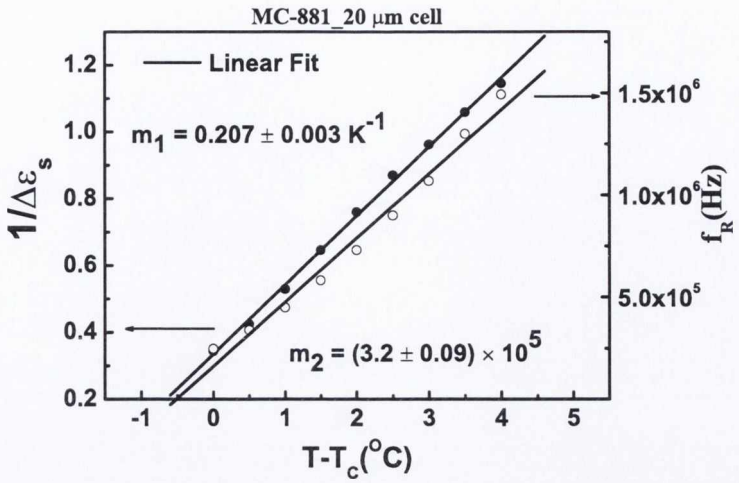

Figure 5.2: Transition temperature dependence of the relaxation frequency and the inverse of the soft mode relaxation strength in the de Vries-type Sm-A^* phase in MC-881.

law. According to Žekš and Čepič [12], we may expect two amplitude modes in Sm-A^* phase, one ferroelectric and another antiferroelectric. The antiferroelectric mode does not contribute to the dielectric permittivity and therefore we neglect it. Frequencies of two amplitude modes tend to zero (softening) at different temperatures. If the ferroelectric amplitude mode condenses at higher temperature than the antiferroelectric amplitude mode ($T_f > T_a$), the Sm-A^*-Sm-C^* phase transition occurs. If the reverse is true ($T_f < T_a$), the Sm-A^*-Sm-C_A^* transition occurs. The dielectric response in the Sm-A^* phase exhibiting a Sm-C_A^* transition should be similar to the dielectric response of the Sm-A^* phase exhibiting a Sm-C^* transition as the equations describing the electroclinic effect (linear coupling of the electric field to the ferroelectric order parameter) and the dynamics of the ferroelectric amplitude mode are the same [83–85]. We apply the Landau theory of the dielectric response of the conventional second order Sm-A^*-Sm-C^* transition to de Vries-type Sm-A^*-Sm-C_A^* transition to determine the Landau parameters associated with the de Vries-type Sm-A^*-Sm-C_A^* transition.

The linear electroclinic response to the applied field in the paraelectric Sm-A^* phase can be written as $\theta = eE$, where the e is the electroclinic coefficient and

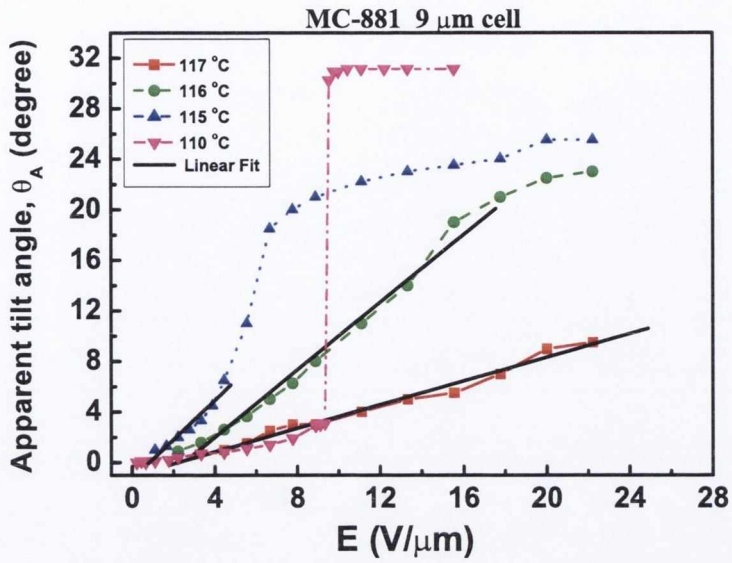

Figure 5.3: Apparent tilt angle as a function of the applied field at different temperatures for the cell thickness of 9 μm. In the de Vries-type Sm-A^* phase linear regime is observed for low values of the measuring field.

Table 5.1: Numerical results obtained by fitting the theoretical expressions for MC-881 for a cell thickness of 20 μm.

$\chi_f C_f = (1.44 \pm 0.09) \times 10^8 V m^{-1} rad^{-1}$
$\alpha = (38 \pm 2.59) k N m^{-2} rad^{-2} K^{-1}$
$\gamma = (1.9 \pm 0.18) \times 10^{-2}$

is given by [86]

$$e = \frac{\epsilon_0 \chi_f C_f}{\alpha(T - T_c)} \tag{5.5}$$

Fig. 5.2 shows the temperature dependence of the relaxation frequency (f_{max}) and the inverse of the soft mode relaxation strength ($1/\Delta\epsilon_s$) in de Vries-type Sm-A^* phase for 20 μm cell thickness. The slope of the temperature dependence of f_{max} and $1/\Delta\epsilon_s$ are also calculated to find different Landau parameters at the de Vries-type Sm-A^*-Sm-C_A^* transition. Fig. 5.3 shows the dependence of the apparent tilt angle as a function of the applied field at different temperatures for cell thickness of 9 μm. A strong increase in the dielectric amplitude of the soft

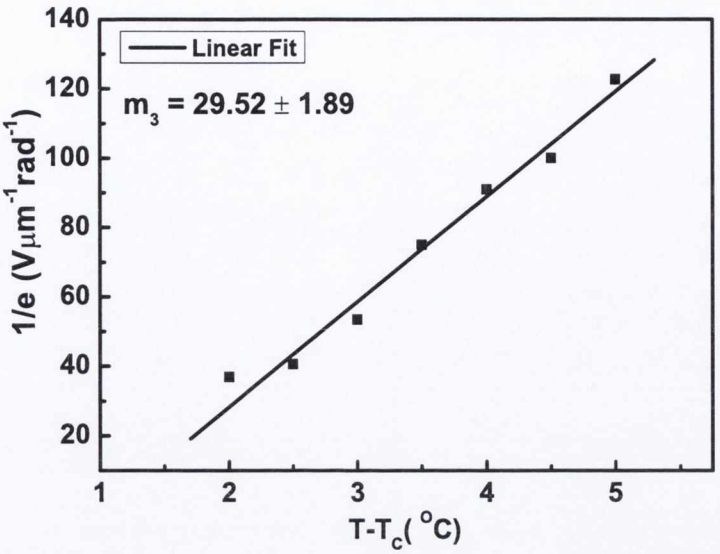

Figure 5.4: Inverse electroclinic coefficient as a function of the transition temperature.

mode, when approaching de Vries-type Sm-A^*-Sm-C_A^* transition, indicates a tilt induced by the field. At a lower temperature in the de Vries-type Sm-A^* phase, a strong electric field induces an apparent tilt angle that can nearly be of the same order as the saturation tilt angle in the Sm-C_A^* phase. For low values of E, the tilt angle varies linearly with the electric field in the de Vries-type Sm-A^* phase as shown using linear fit in Fig. 5.3. Above a certain value of the field, the linear relation is no longer valid and at this stage a phase transition from de Vries-type Sm-A^* phase to the Sm-C^* phase is possible. Fig. 5.3 also suggests that the field dependence of the apparent tilt angle in de Vries-type phase Sm-A^* is changing from a 'Langevin' type in the Sm-A^* phase at 117 °C to a discontinuous one at 115 °C. The electronic coefficient e has been determined from the linear part of the $\theta(E)$ curves. The temperature dependence of the reciprocal value of the electroclinic coefficient $1/e$ in de Vries-type Sm-A^* phase is shown in Fig. 5.4. In the studied temperature range above T_c, the temperature dependencies of the quantities characterizing the soft mode of de Vries-type Sm-A^* phase namely; $1/\Delta\epsilon_s$, f_{max}, and $1/e$, shown in Fig. 5.2 and Fig. 5.4 confirm the simple linear description given by the expressions in equations Eqs. 5.3-5.5. From slopes of those dependencies and using equations Eqs. 5.3-5.5 the Landau parameters α,

$\chi_f C_f$, γ are calculated and given in Table 5.1.

With an exception of the viscosity coefficient, γ, which is very low, different Landau parameters for de Vries-type Sm-A^*-Sm-C_A^* transition are found to be of the same order of magnitude as those obtained for a conventional Sm-A^*-Sm-C_A^* transition [1].

5.3 Dielectric study of the de Vries-type Sm-A^*-Sm-C^* transition

5.3.1 The Soft mode fluctuations

Dielectric measurements were carried out for three mixtures: 88MC881, 80MC881, and 72MC881 with and without dc-bias field applied across a 20 μm planar cell. As the mixtures exhibit de Vries-type Sm-A^*-Sm-C^* transition, the soft mode is made visible by applying an external dc-bias field since suppression of the Goldstone absorption by dc-bias is far more effective than the suppression of the soft mode [40]. Fig. 5.5 shows the dependence of the dielectric loss spectra (ϵ') of the mixtures 88MC881, 80MC881, and 72MC881 (The compositions and phase sequences are given in Table 4.1) on temperature for a 20 μm cell under an applied dc bias of 2 V/μm. The dielectric loss spectra with and without applied dc bias for the various mixtures are fitted to the Havriliak-Negami equation (Eq. 5.1) to find the $\Delta\epsilon$ at the de Vries-type Sm-A^*-Sm-C^* transition. Fig. 5.6*a* shows the dependence of the $\Delta\epsilon$ on temperature with and without applied dc-bias for these mixtures: 88MC881, 80MC881, and 72MC881. It is noted that the $\Delta\epsilon$ at de Vries-type Sm-A^*-Sm-C^* transition goes up with increased ferroelectric composition in the mixtures as the Goldstone mode becomes gradually stronger in the mixture [87]. But the experimental observations become interesting when the Goldstone mode is suppressed by applying the dc-bias. With the application of the dc-bias, only the soft mode is visible at the de Vries-type Sm-A^*-Sm-C^*

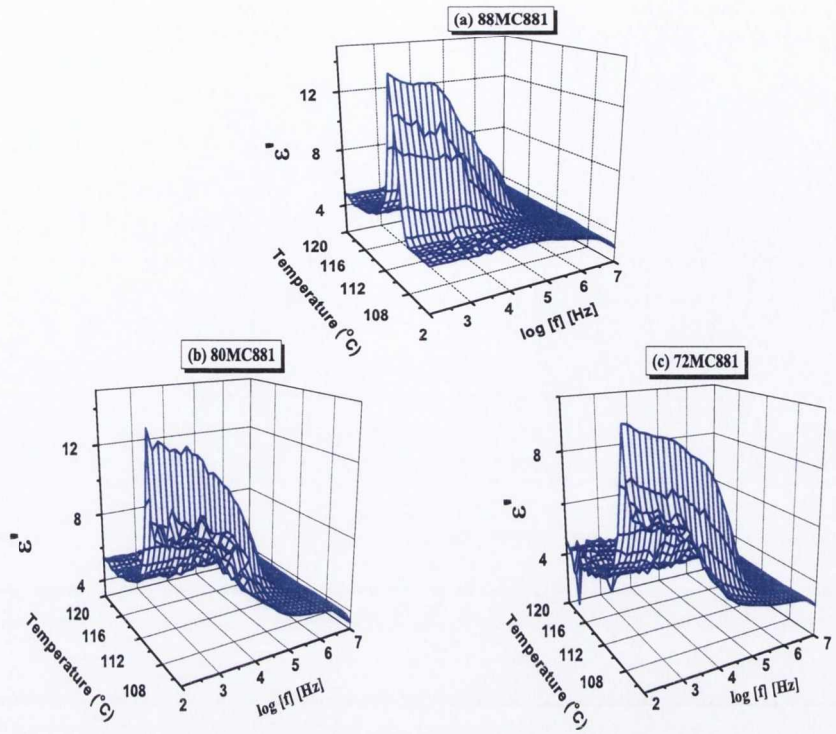

Figure 5.5: Dependence of the dielectric spectra (ϵ') on temperature and frequency of (*a*) 88MC881, (*b*) 80MC881, and (*c*) 72MC881 under applied dc bias of 2 V/μm for 20 μm cell. DC bias of 2 V/μm is applied to suppress the Goldstone mode at de Vries-type Sm-A^*-Sm-C^* transition.

transition and it is observed that the soft mode strength ($\Delta\epsilon_s$) at the de Vries-type Sm-A^*-Sm-C^* transition temperature decreases by increasing the ferroelectric composition in the mixture as shown in figure Fig. 5.6*a*. The spectra of the real (ϵ') and imaginary parts (ϵ'') of the dielectric permittivity for all the mixtures at the de Vries-type Sm-A^*-Sm-C^* transition temperature (with applied dc-bias) are plotted as a function of frequency in Fig. 5.6*b*. It is observed that the amplitudes of ϵ' and ϵ'' decrease with increasing ferroelectric composition in the mixture at the transition temperature. The values of $\Delta\epsilon$ for different mixtures are listed in Table 5.2.

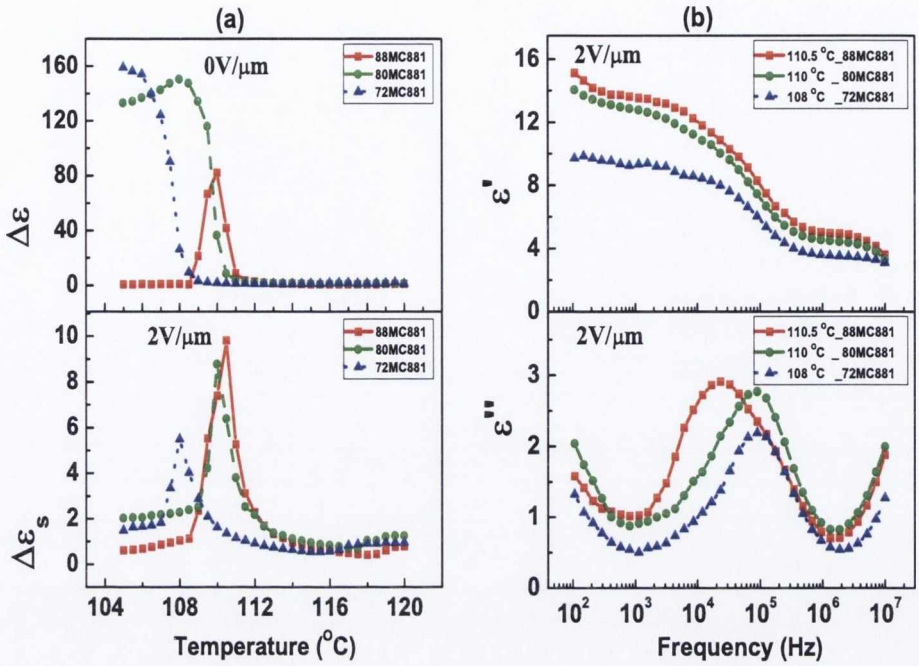

Figure 5.6: (*a*) Dependence of the dielectric relaxation strength with and without dc bias on temperature for different compositions of MC-815 and MC-881 mixtures in 20 μm cell and (*b*) the real and the imaginary parts of the dielectric permittivity with dc bias at de Vries-type Sm-A^*-Sm-C^* transition temperatures of different compositions of MC-815 and MC-881 mixture for 20 μm cell thickness.

5.3.2 The Landau parameters

The amplitude mode in de Vries-type Sm-A^* phase exhibiting Sm-C^* transition can be described by Eq. 5.3 and Eq. 5.4. The Curie-Weiss plot of the inverse dielectric strength $(1/\Delta\epsilon_s)$ as a function of the difference between the measured temperature and transition temperature, Curie point $T - T_c$ for the three mixtures is shown in Fig. 5.7. This shows a Curie-Weiss plot at de Vries-type Sm-A^*-Sm-C^* transition for a 20 μm cell. From the linear fits of f_{max} and $1/\Delta\epsilon_s$ as a function of a difference in the temperature from the transition temperature and the plots of the apparent tilt angle as a function of the applied field in de Vries-type Sm-A^* phase of all the three mixtures, we can calculate the different Landau parameters for de Vries-type Sm-A^*-Sm-C^* transition, similar to those found for de Vries-type Sm-A^*-Sm-C^*_A transition as described earlier. These are listed in Table 5.2.

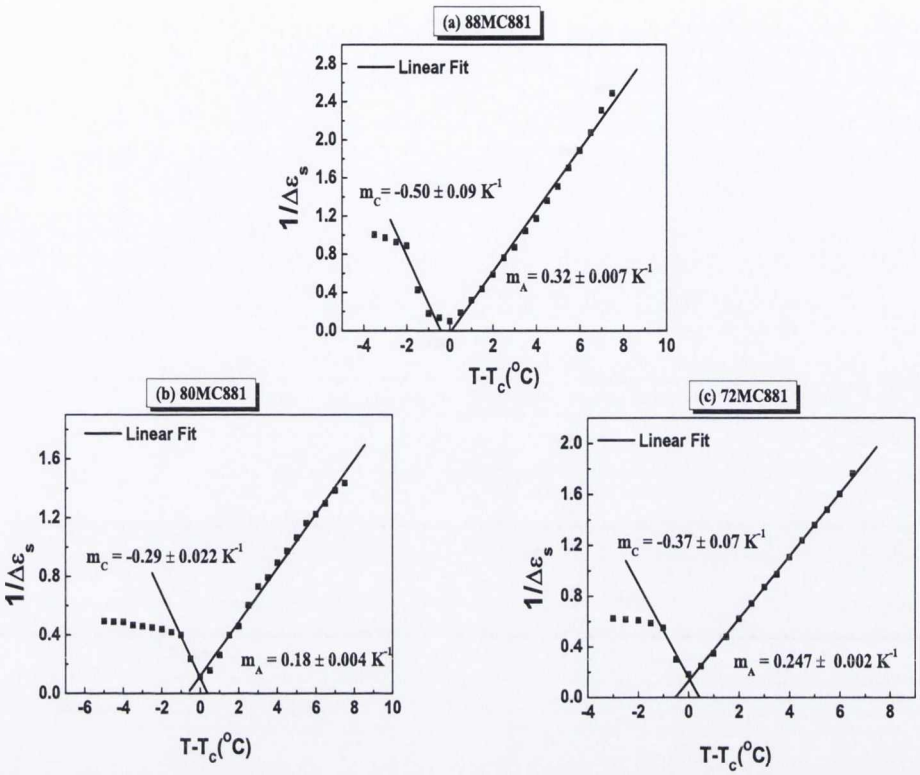

Figure 5.7: Curie-Weiss plot at the de Vries-type Sm-A^*-Sm-C^* transition of (a) 88MC881, (b) 80MC881 and (c) 72MC881 for 20 μm cell.

Table 5.2: Comparison of different parameters of different compositions of MC-815 and MC-881 mixture.

Landau parameters	Mixture-1	Mixture-2	Mixture-3
$\Delta\epsilon_s$	9.8	8.8	5.5
α $(kNm^{-2}rad^{-2}K^{-1})$	(7.8 ± 0.4)	(33.5 ± 2.4)	(51.8 ± 2.9)
$\chi_f C_f$ $(V\mu m^{-1}rad^{-1})$	(52.3 ± 2.7)	(144.9 ± 7.8)	(153.8 ± 7.3)
γ (pa)	$(6 \pm 0.5) \times 10^{-3}$	$(2.6 \pm 0.2) \times 10^{-2}$	$(3.2 \pm 0.5) \times 10^{-2}$
$C - WRegime(K)$	9.5	8	7.5

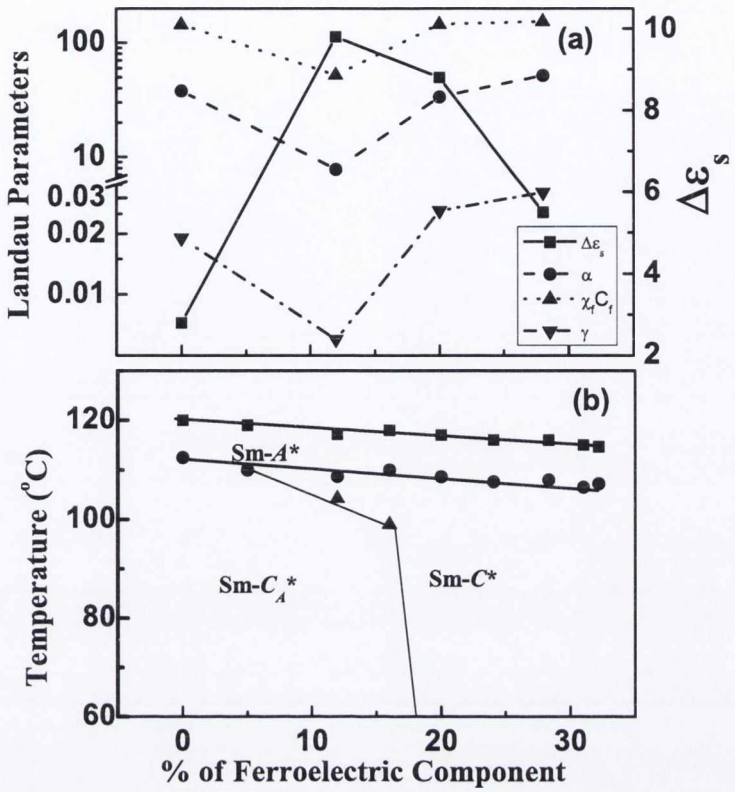

Figure 5.8: (*a*) Variation of the soft mode dielectric strength and different Landau parameters with increased ferroelectric component in the mixtures. (*b*) The phase diagram of the ferro- and antiferroelectric liquid crystal mixture for thin cells.

Fig. 5.8*a* shows the variation of the $\Delta\epsilon_s$, α, $\chi_f C_f$ and γ for increased percentage of the ferroelectric component in the mixture. We see that the soft mode strengths at the de Vries-type Sm-A^*-Sm-C^* transition temperature are 9.8, 8.8 and 5.5 for 88MC881, 80MC881, and 72MC881 respectively, which means that the soft mode strength is reduced by 10% for 80MC881 and 44% for 72MC881 compared to the strength of the 88MC881, which is the opposite to what happens when the ferroelectric composition of the mixture increase. We also note that the value of the Landau coefficient α increases with increased ferroelectric composition of the mixture. The theoretical value of the ratio of the slopes of the Sm-C^* phase and the de Vries-type Sm-A^* phase (m_{C^*}/m_{A^*}) in the Curie-Weiss plot is -2 over a certain temperature range [40], called the mean-field regime where the Curie-Weiss law is valid. The mean-field regime, also called the Curie-Weiss regime is characterized

by the following equation [62]:

$$T_c - T_o \approx \frac{3b^2}{4\alpha c} \tag{5.6}$$

T_0 is the crossover temperature from the mean-field to the tri-critical behavior and α , b, and c are the coefficients of the Landau expansion for the free energy density as described earlier. We see that the Curie-Weiss temperature interval is slightly narrower for 72MC881 ($\approx 7.5K$) and 80MC881 ($\approx 8K$) compared to 88MC881 ($\approx 9.5K$). This is the opposite to what happens when the ferroelectric composition of the mixture increase. Values of the Curie-Weiss temperature interval are calculated by subtracting the temperature up to which the $1/\Delta\epsilon_s$ vs $T - T_c$ plot is linear in Sm-C^* phase up to linearity in the Sm-A^* phase. Assuming that the coefficients b and c should be of the same order of magnitude for all the mixtures, according to Eq. 5.6, a larger value of the Landau coefficient α will lead to a narrower Curie-Weiss temperature range supported by our experimental observations. The major part of the restoring force to the tilt angle fluctuations (soft mode fluctuations) generally should be the elastic energy associated with tilt-induced changes of the smectic layer spacing. The smaller the elastic energy needed to change the director tilt and, consequently, the smaller is the restoring force to the tilt-angle fluctuations. In other words, the weaker the coupling between tilt and layer spacing, the stronger the soft mode fluctuations [62]. In Chapter 4, the x-ray diffraction measurement showned that with increased ferroelectric composition in the mixture, the layer spacing at the de Vries-type Sm-A^*-Sm-C^* transition increases. As a result, the soft mode dielectric relaxation strength decreases, Landau coefficient α increases and the Curie-Weiss regime decreases with increased ferroelectric composition in the mixture. We also note that the value of the Landau coefficient of the temperature dependent term α decreases much more for the low layer shrinkage materials compared to other Landau parameters.

The phase diagram of the studied ferro- and antiferroelectric liquid crystal mixtures for thin cells is shown in Fig. 5.8*b*. It is observed that the soft mode

dielectric strength and other related Landau parameters of the de Vries-type Sm-A^* phase exhibiting transitions to the Sm-C_A^* as well as to Sm-C^* phases are of the same order of magnitude except for the composition where on the phase diagram the phase sequence is I-Sm-A^*-Sm-C^*-Sm-C_A^*. This may be related to the fact that the molecular fluctuations in the Sm-A^* are large, as both Sm-C^* and Sm-C_A^* are stable leading to a large soft mode amplitude and consequently α, $\chi_f C_f$ and γ decreases. The interlayer molecular interactions in such a case could be responsible for this observation.

5.4 Conclusions

The Landau parameters associated with the Sm-A^*-Sm-C_A^* transition in the pure AFLC and Sm-A^*-Sm-C^* transition in different mixtures with increased ferroelectric composition are calculated using Landau theory of the second order phase transition from dielectric measurements. It is noted that as the soft mode dielectric relaxation strength decreases, the Landau coefficient α increases and the Curie-Weiss temperature range decreases at the de Vries-type Sm-A^*-Sm-C^* transition with increased ferroelectric composition in the mixture. These can be explained by the observation that with increased ferroelectric composition in the mixture, the layer shrinkage at the de Vries-type Sm-A^*-Sm-C^* transition increases, as a result of strong coupling between the tilt and the layer thickness. For low layer shrinkage materials, the restoring force of the tilt-angle fluctuations is smaller. As a result, the soft mode dielectric relaxation strength decreases, Landau coefficient α increases and the Curie-Weiss regime decreases with increased ferroelectric composition in the mixture.

It is also found that the soft mode dielectric strength and other related Landau parameters of the de Vries-type Sm-A^* phase exhibiting transitions both to the Sm-C_A^* and to Sm-C^* phases are of the same order of magnitude except where

the phase sequence on the phase-diagram is I-Sm-A^*-Sm-C^*-Sm-C^*_A. Measurements on mixtures close to an almost vertical line separating the phases Sm-C^*_A and Sm-C^* on the phase diagram may lead to further interesting results.

Chapter 6

Electric field dependent dielectric response and response time in an electroclinic liquid crystal

"In this chapter, *the results of the electric field dependent dielectric strength, relaxation frequency and response time in TSiKN65 are presented. The dielectric strength and the response time are shown to increase, and the relaxation frequency decrease over a large temperature range up to a certain value of the electric field in the smectic-A* phase. This behavior contrasts to that observed in a conventional smectic-A*, but can be explained in terms of de Vries scenerio. On assuming that the reorientation of the molecular dipoles with electric field to be of the Langevin type in the de Vries smectic-A*, it is found that around 1300 molecules, corresponding to a minimum correlation length of* $\xi_\perp \approx 45$ *nm in a single layer, cooperatively respond to the applied field. "*

6.1 Introduction

Landau theory of smectic phases was developed to show that de Vries behavior occurs in materials with unusually small orientational order [66], which has been experimentally demonstrated [25, 59, 88]. It was also shown that a decrease in the layer shrinkage increases the soft mode strength and decreases the Landau coefficient at the de Vries SmA^*-SmC^* transition [62, 69]. Application of an electric field parallel to the smectic layers orders the azimuthal orientation, such that an average director is tilted away from the layer normal. But it has been an issue of discussion in recent years as to how this azimuthal ordering is achieved in these materials with the application of an electric field. It has been suggested that the de Vries materials with sufficiently high polarization density exhibit large analog optical axis rotation($> 30^o$) accompanied by increased birefringence, as found by the electro-optic measurements. These can be modeled by the Langevin theory of field induced director orientation on assuming the molecules in the SmA^* phase are confined to a tilt cone [22]. Another systematic model for the orientational distribution in de Vriestype materials through a series of manipulations of the dielectric tensor predicts the dependence of the optical birefringence and tilt angle on electric field and temperature assuming the local order is slightly biaxial [27]. It has also been suggested that perhaps there is some type of modulation or spatial periodicity in the azimuthal angles associated with the tilt directions [89]. This model predicts the microscopic origin of the electroclinic effect, one that shares some of the macroscopic characteristics of the de Vries scenario, specifically, no layer contraction and field dependent birefringence. It is assumed that a Sm-A^* phase in some materials close to the Sm-C^* to Sm-A^* transition, could in fact be a modulated version of the smectic-C^* phase, a network of defects, walls, and lines, but one where the spacing between the defects is in the subvisible range. This modulated phase would have no long-range azimuthal order or net polarization in the absence of an electric field. Thus, to the eye, this phase would appear to be a Sm-A phase. However, the application of an electric field distorts the structure of the defect array and leads to a large electroclinic effect.

6.2 Electric field dependent dielectric response in conventional smectic-A^* phase

As described in previous *Chapters*, an electric field applied in the Sm-A^* phase, induces a tilt in the system, known as the electroclinic effect. If this tilt is linear with the applied field, the restoring torque acting on the system is associated with a harmonic potential. The force constant of the potential is proportional to the inverse of the slope of the induced tilt versus bias field. It is well known that adding a constant force to a harmonic potential displaces the equilibrium of the system leaving the eigen frequency unchanged. Thus, we do not expect any influence on the relaxation frequency of the system as long as the electroclinic effect shows a linear behavior with the field. But, when the electroclinic effect is non-linear, the torque acting on the system can no longer be associated with a harmonic potential but with some more general form. However, for a given bias field, as we are studying only small oscillations around the equilibrium position, we can approximate the potential with a harmonic one, the force constant of which is proportional to the inverse of the slope of the induced tilt versus bias field. Thus, an increasing bias field is associated with a decreasing slope, the force constant of the system and thus the relaxation frequency will increase with increasing bias field. Qualitatively, an increased stiffness of the system results in a smaller response and so we expect the dielectric strength to behave in the opposite way to that of the relaxation frequency. Gouda *et. al.* [90] developed a mean field model to describe electric field dependent dielectric behavior of the soft mode in the Sm-A^* phase. Kalmykov *et. al* [91] simplified this model to obtain analytical solutions for the dielectric strength ($\Delta\epsilon$) and relaxation frequency f_{max} of the electric field dependent dielectric response in the in the Sm-A^* phase. The field dependent $\Delta\epsilon$ and f_{max} are dependent on the electroclinic coupling and the nonlinear field dependence of the induced tilt, and are described by two sets of equations.

For low fields:

$$\Delta\epsilon \cong \Delta\epsilon^0 - 4\pi C_1 E^2 \tag{6.1}$$

$$f_{max} \cong f^0_{max} + \gamma_S (A/2\pi c\chi)^2 C_1 E^2 \tag{6.2}$$

and for higher fields:

$$\Delta\epsilon \cong C_3 E^{-2/3} \tag{6.3}$$

$$f_{max} \cong (C_2/2\pi) E^{2/3}, \tag{6.4}$$

where $\Delta\epsilon^0 = 4\pi(\chi c)^2/A$ and $f^0_{max} = A/2\pi\gamma_S$ are the dielectric strength and the relaxation frequency in the absence of the field, respectively. A, C_1, C_2 and C_3 are constants. χ is a generalized susceptibility, c is the electroclinic coupling constant and γ_S is rotational viscosity associated with the rotation of the director. Fig.6.1(b) shows the dependence of $\Delta\epsilon$ and f_{max} on electric field in the conventional SmA^* phase for Felix-18.

6.3 Electric field dependent dielectric response in TSiKN65

The liquid crystalline compound TSiKN65 (SmC^* 27 ^{o}C SmA^* 57 ^{o}C I, 4-[3'-nitro-4'-((R)-1-methylhexyloxy) phenyl] phenyl 4 -(6-heptylmethyltrisiloxyhexyloxy), used for the experiments is a recently reported prototype de Vries material having small layer contraction with temperature and electric field, large electroclinic effect and small orientational order parameter [24, 27, 59]. For planar alignment, the conducting inner surfaces of the liquid crystalline cell were spin coated with a polyimide RN 1175 (Nissan Chemicals, Japan) alignment layer and rubbed parallel. Dielectric measurements in the frequency range from 1 Hz to 10 MHz were carried out by using the Novocontrol Alpha High Resolution Dielectric Analyzer. During measurements, the system allowed us to superimpose dc bias voltages up

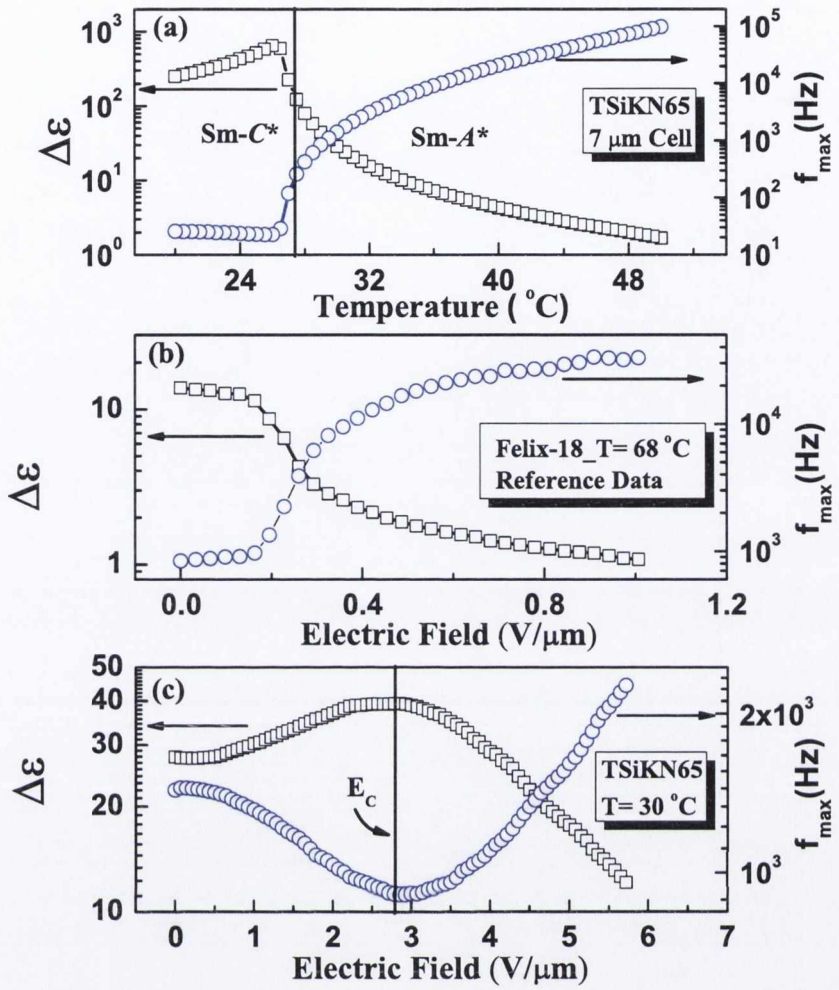

Figure 6.1: (a) Dependence of the dielectric strength ($\Delta\epsilon$) and relaxation frequency (f_{max}) on temperature without any electric field for TSiKN65. (b) Dependence of $\Delta\epsilon$ and f_{max} on applied electric field in the SmA^* phase of Felix-18 (Reference data). (c) Dependence of $\Delta\epsilon$ and f_{max} on applied electric field in the SmA^* phase for 30 ^oC temperature of TSiKN65.

to 40 V on an ac voltage of 0.03 V_{rms}. The results of the high resolution dielectric measurements on cooling a 7 μm cell from the isotropic phase with and without the external electric field in TSiKN65 and Felix-18 (SmC^* 67 ^{o}C SmA^*, Hoechst, Germany) are shown in Fig.6.1. Fig.6.1(a) shows the dependence of $\Delta\epsilon$ and f_{max} on temperature without any electric field for TSiKN65. These are found by fitting the dielectric spectra to the Havriliak-Negami equation. It is found that $\Delta\epsilon$ and f_{max} start to diverge as the system approaches transition towards SmC^* phase.

Eqs. 6.1-6.4 suggest that by increasing the electric field E, $\Delta\epsilon$ decreases and

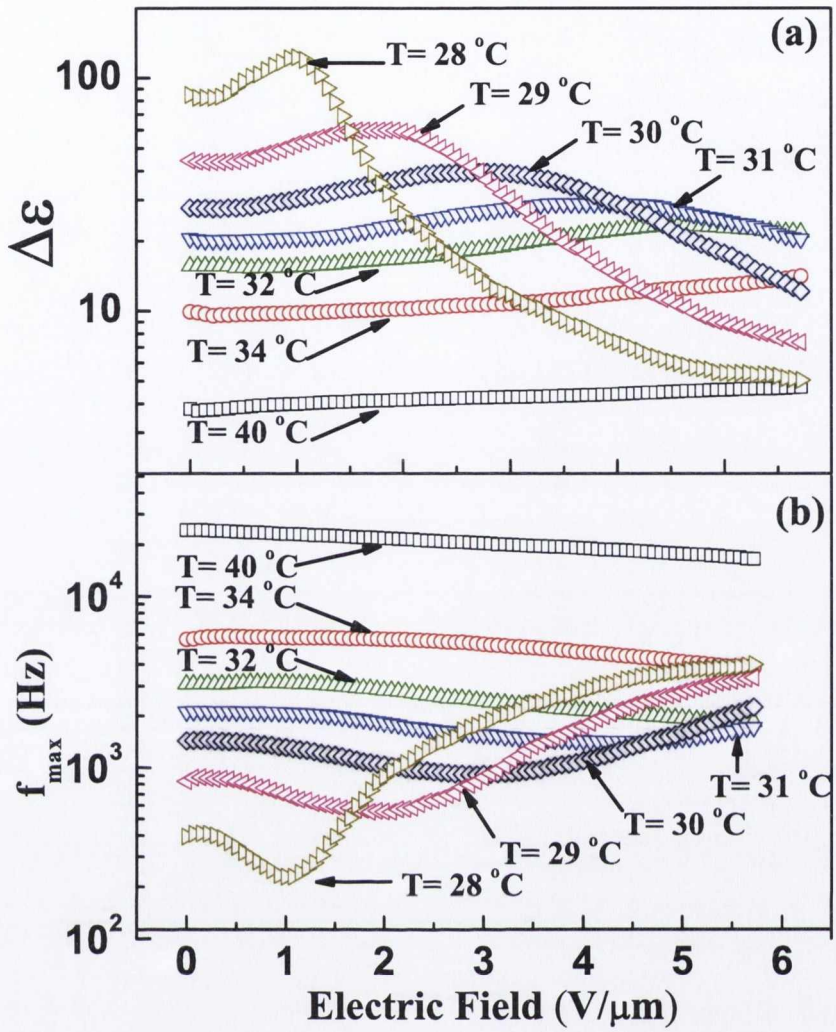

Figure 6.2: Dependence of the (a) $\Delta\epsilon$ and (b) f_{max} on applied electric field for different temperatures in the SmA^* phase in TSiKN65.

f_{max} increases in the SmA^* phase as shown in Fig.6.1(b) for Felix-18. Whereas, Fig.6.1(c) shows that on increasing the electric field, $\Delta\epsilon$ increases and f_{max} decreases up to a certain value of the electric field ($E_C \approx 2.8\ V/\mu m$ at 30 ^oC) in the SmA^* phase of TSiKN65. On further increasing the electric field, $\Delta\epsilon$ starts to decrease and f_{max} starts to increase. Fig. 6.2(a and b) shows the dependence of $\Delta\epsilon$ and f_{max} on the applied electric field at various temperatures in the SmA^* phase of TSiKN65. It is found that for all these temperatures, $\Delta\epsilon$ initially increases and then decreases, and f_{max} initially decreases and then increases. The maximum value of $\Delta\epsilon$ and the minimum value of f_{max} depend on the temperature. For lower temperatures, the maximum value of $\Delta\epsilon$ is higher, whereas the minimum value of

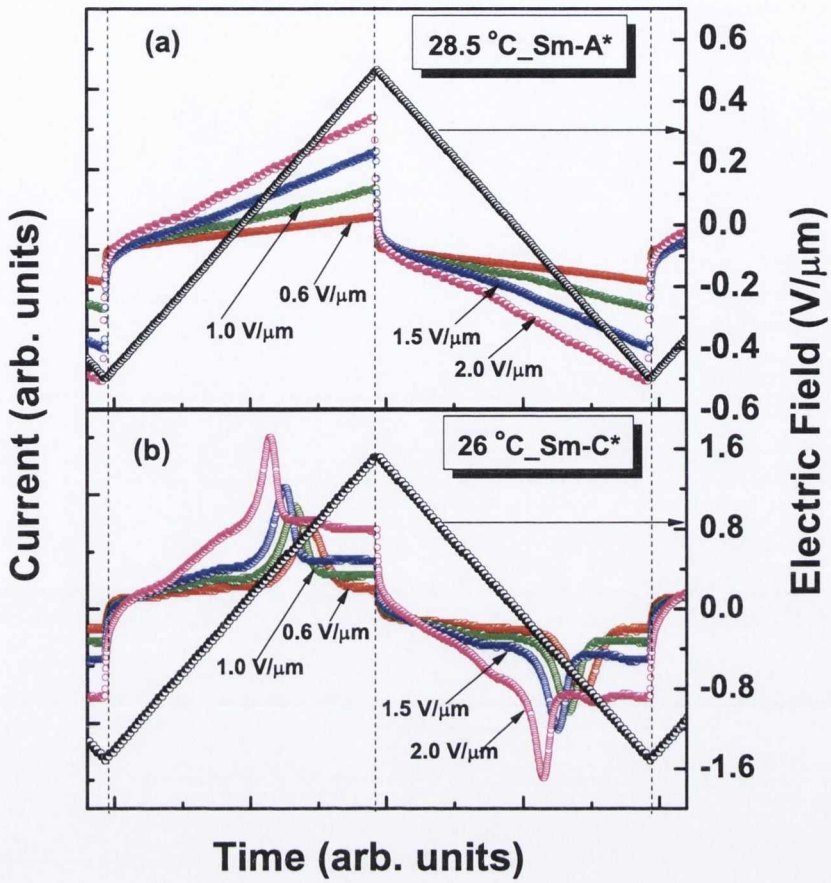

Figure 6.3: The current response to an applied triangular wave of the sample kept at the conditions for maximally unusual dielectric response, T = 28.5 ^oC and 0.5-2.0 $V/\mu m$ field strength.

f_{max} is lower. E_C also depends on temperature, which is lower for lower temperatures. For temperatures of 34 and 40 ^oC the value of the applied field was not high enough to obtain E_C. A similar behavior was observed for a a very narrow range of temperatures ($\approx$ 0.8 ^oC) in the SmA^* phase of C-7, undergoing a first order transition transition to SmC^* phase due to a shift in SmA^*-SmC^* transition temperature [92]. Such a possibility is excluded by measuring the current response to an applied triangular wave in the Sm-A^* phase of TSiKN65 kept at temperature of 28.5 ^oC (1.5 ^oC above the transition temperature). This is a temperature where the maximum unusual dielectric response is observed. It is noted that no polarization peaks are visible in the Sm-A^* phase of TSiKN65 for different values of applied triangular voltage as in Fig. 6.3*a*, whereas, polarization peaks are visible in the Sm-C^* phase of TSiKN65 for different values of applied triangular voltage as

in Fig. 6.3*b* . Moreover, the electric field induced tilt angle and polarization curves always show a continuous increase in contrast to discontinuous increase in C-7. However, this unusual field dependent dielectric response can well be explained by the de Vries scenario on assuming the reorientation of the molecules by azimuthal angle fluctuations with the application of electric field as discussed *Section* 6.5.

6.4 Electric field dependent response time in TSiKN65

For response time measurements, the aligned cell was placed on a hot-stage which is controlled to a temperature with an accuracy better than $\pm$ 0.01 K. In this configuration, the transmitted light intensity through the cell varies as

$$I = I_0 \sin^2[2(\theta + \theta_0)], \tag{6.5}$$

where θ is the field induced tilt angle and θ_0 is the angle between the liquid crystalline optic axis and the polarizer at zero field. After determining the dark state, θ_0 was set to 22.5^o for optimum sensitivity. We measured the response time (rise time) of the transmitted optical power (10 % $\rightarrow$ 90 %) detected with a photodiode whose output was amplified and monitored on an oscilloscope subject to a DC balanced 10 Hz square wave. The characteristics response time in the SmA^* phase is given by

$$\tau = \eta_\theta / \alpha_0 (T - T_C), \tag{6.6}$$

where η_θ is the rotational viscosity associated with the θ motion. Fig.6.4 presents dependence of the response time on electric field in the SmA^* phase for TSiKN65 at various temperatures. We find that the response time increases which continues to be the case up to a certain value of the electric field (E_c) for all temperatures. On further increasing the electric field, the response time decreases. This behavior contrasts with that for a conventional SmA^* phase, where τ is independent of E in

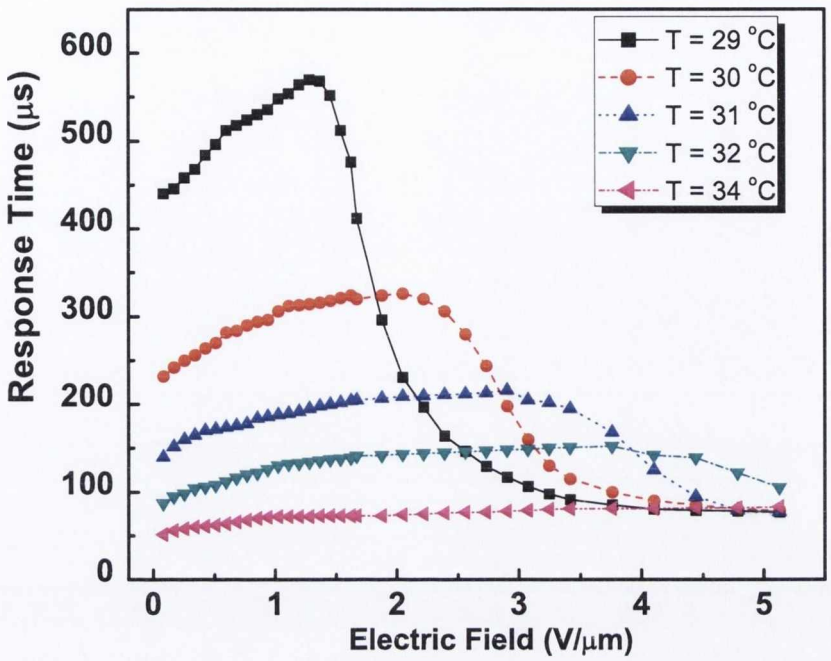

Figure 6.4: Electric field dependent response time in the SmA^* phase of TSiKN65 for various temperatures.

the small θ approximation and has a small dependence on electric field for larger θ [93, 94] as observed in KN125 [95, 96]. For higher temperatures within SmA^* phase in TSiKN65, it was found that the response time increases to a certain value of the electric field [93, 95], but the reasons were not given nor was it highlighted as an anomalous property of the material. The observed unusual behavior of the field dependent response time can well be explained by the de Vries scenario on assuming that the reorientation of the molecular dipoles with the electric field is of the Langevin type and by considering an increase in the effective dipole moment (μ_{eff}) with increasing field as discussed below.

6.5 Langevin theory; Electric field induced polarization in TSiKN65

With the application of E in the de Vries SmA^*, and on assuming a uniform molecular distribution $f(\varphi) = 1/2\pi$ on a cone in a single layer, the local polarization P_l couples φ to the applied field with an energy $U_P = -\pi d(\xi_\perp/2)^2 P_l.E = \mu_{eff} E\cos\varphi$, where $\xi_\perp$ is the temperature dependent molecular correlation length in a single layer and

$$\mu_{eff} = \pi d(\xi_\perp/2)^2 P_l, \tag{6.7}$$

is the effective dipole moment. This equation is introduced to calculate the temperature dependence of the correlation length. With the application of E, the apparent optic axis orientation increases from zero (with $< \cos\varphi >= 0$, $< \cos^2\varphi >= 1/2$) to θ_A (with $< \cos\varphi >\approx 1$, $< \cos^2\varphi >\approx 1$, where θ_A is the smectic cone angle. The averages $< \cos\varphi >$ and $< \cos^2\varphi >$ can be evaluated using the Langevin equation for the azimuthal probablity distribution described by the ratio of an electric aligning energy $\mu_{eff}E$ to the thermal energy k_BT given by

$$P_s = P_l \langle\cos\varphi\rangle = \frac{\int_o^\pi \exp(\frac{\mu_{eff}E\cos\varphi}{k_BT})(P_l\cos\varphi)d\varphi}{\int_o^\pi \exp(\frac{\mu_{eff}E\cos\varphi}{k_BT})d\varphi}, \tag{6.8}$$

where k_B is the Boltzmann constant and P_s is the field induced macroscopic polarization. The electric field induced Langevin-like alignment of the local in-plane dipoles against thermal fluctuations and constraints imposed by surface interfaces, induces the net polarization gradually. Note that the Langevin process described above assumes μ_{eff} as constant for different values of E. Fig. 6.5*a* shows the electric field dependent P_s for different temperatures. The black solid lines in Fig. 6.5*a* are the best fits of the Langevin theory described by Eq. 6.8 to the experimental results. The observed results are well simulated for μ_{eff} varying from approximately 4 to 2000 D depending on the temperature in the de Vries-type SmA^* phase as

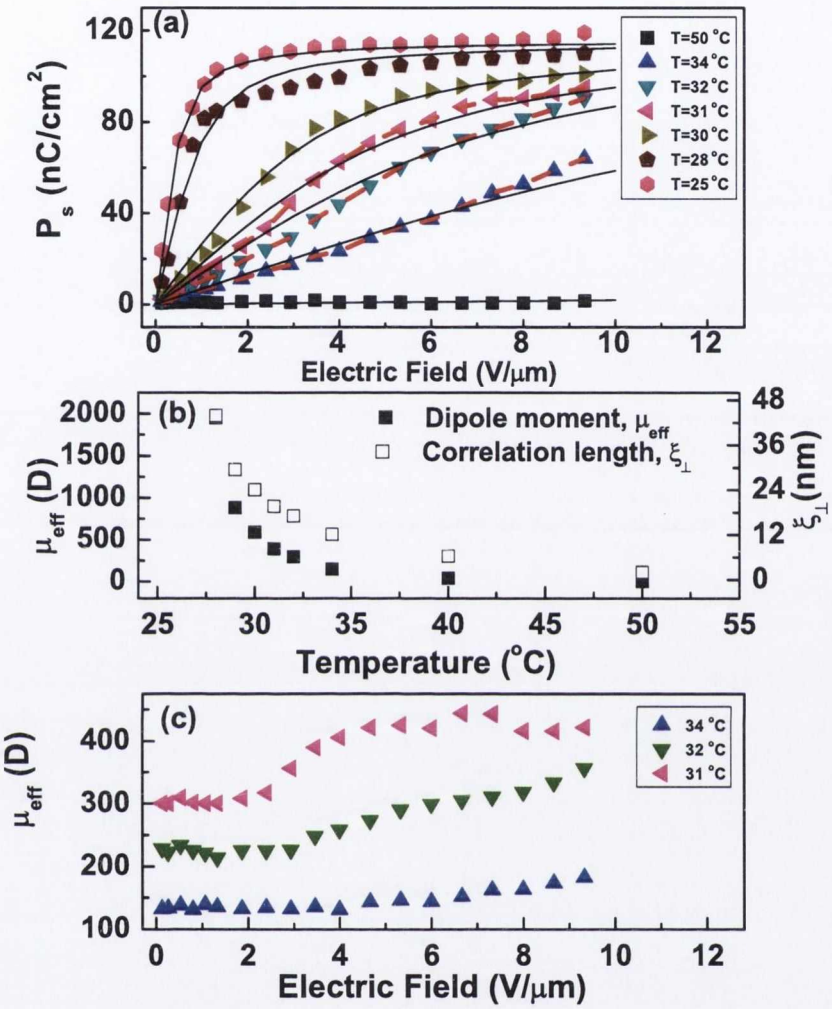

Figure 6.5: (a) represents the electric field induced polarization (P_s) for different values of temperatures in TSiKN65. The solid black lines are the best fit of the data to the Langevin process described in Eq. 6.8. (b) shows the variation of effective dipole moment (μ_{eff}) and correlation length ($\xi_\perp$) with temperature in the de Vries-type SmA^* phase. (c) represents values of the electric field dependent μ_{eff} determined by fitting the electric field dependent P_s as shown by red dashed lines in (a) to the Langevin process considering the increase of μ_{eff} with field.

shown in Fig. 6.5*b*. The magnitude of typical dipole moment of a single molecule is in the order of 1-2 D [97]. On assuming the dipole momemt of a single molecule as 1.5 D, it is found that μ_{eff} corresponds to a maximum of around 1300 molecules at 28 ^{o}C. Thus, the interaction of molecular dipoles and the applied electric field does not involve one molecule, but a maximum of around 1300 molecules cooperatively respond to the applied electric field. Hence, we note that the molecules in the de Vries-type SmA^* phase possess a local order even without the application of electric field. A similar type of behavior has been observed in a non-tilted smectic phase of an asymmetric bent-core liquid crystalline compound [98]. The number of molecules possessing the local order depends upon the temperature. Normally, we need a large electric field to orient randomly distributed dipoles under the action of thermal energy. But, in the case of de Vries-type SmA^*, because of the existing local order of the molecules, a sufficiently low electric field is enough to induce a large polarization. For lower temperatures, the number of molecules possessing the local order is higher, as a result, less electric field is needed to induce a large polarization. As a result, we observe higher $\Delta\epsilon$ and τ, and lower f_{max} for lower temperatures. By inserting the measured saturated value of $P_s = 119\ nC/cm^2 (\approx P_l$ at high field) and by assuming a perfect ordering of dipoles, the minimum value of the correlation length, $\xi_\perp$ for different values of μ_{eff} and d for different temperatures are calculated from Eq. 6.7 as shown in Fig. 6.5b. Note that if the dipolar ordering decreases, $\xi_\perp$ increases. The variation of d with temperature of TSiKN65 is taken from reference [24]. We note that the correlation length, $\xi_\perp$ is of the order of 45 nm for 1300 molecules at 28 ^{o}C. If we consider the local ordering of the molecules is along the layer normal as well as a single layer, the expression for the effective dipole moment becomes $\mu_{eff} = (4\pi/3)(\xi_{||}/2)^3 P_s$, and $\xi_{||}$ becomes 22 nm, the correlation length along the layer normal for the measured value of the P_s.

By applying the Langevin model, in the de Vries SmA^*, it is found that a maximum of around 1300 molecules cooperatively act as a single entity and respond to the electric field. Since the Langevin model describes the field induced molecular reorientation by azimuthal angle fluctuations, we must conclude the

Langevin-type concentration of $f(\varphi)$ on the smectic cone with application of electric field is accompanied by the field dependent dielectric response in the de Vries SmA^*. Thus the field dependent dielectric response corresponds to the azimuthal angle (φ) fluctuations. Moreover, the relaxation frequencies for the lower temperatures in the de Vries SmA^* are much closer to that of typical values of azimuthal angle fluctuations (≈20-5000 Hz) rather than the tilt angle fluctuations (≈ 1-10^4 kHz) [42, 99]. The Langevin process described by Eq. 6.8 does not consider the increase of μ_{eff} with electric field, which is supposed to be the case in the de Vries SmA^* since application of a field tends to align the transverse dipole of these molecules. This is confirmed by achieving a better fitting of the field dependent P_s to the Langevin process as shown for temperatures of 34, 32 and 31 °C by the red dashed line in Fig. 6.5*a* considering the increase of μ_{eff} with field. The values of the field dependent μ_{eff} for which the P_s are simulated are plotted in Fig. 6.5*c* for these temperatures. It is noted that with increasing field, μ_{eff} increases, hence the number of molecules cooperatively responding to the field also increases, and so does the correlation length. As a result, $\Delta\epsilon$ and τ increase, and f_{max} decrease with the application of an increasing field. At $E = E_C$, the de Vries SmA^* assumes the same symmetry as SmC^* through an azimuthal ordering of the already tilted molecules and on further increasing the field, the azimuthal angle fluctuations are suppressed, as a result, $\Delta\epsilon$ and τ start to decrease, and f_{max} starts to increase.

6.6 Conclusions

In conclusion, it is found that (i) the molecules in the de Vries SmA^* possess a local orientational order even without the application of the electric field, *i. e.*, the molecules are not randomly oriented but orient with a finite correlation length which is of the order of a few tens of *nm*, and these molecules cooperatively respond to the applied electric field, (ii) application of an electric field produces a bias in the distribution of the tilt direction, forcing the molecules to reorientate by rotation around their cone angle, (iii) with increasing field, the number of molecules cooperatively responding to the electric field increases, hence the correlation

length, and as a result, $\Delta\epsilon$ and τ increase, and f_{max} decreases with increasing applied field in de Vries SmA^* phase.

Chapter 7

Effect of the cell surfaces on the stability of the chiral smectic-C phases

"**In this chapter,** *the effect of surfaces on the stability of smectic-C^* variant phases is investigated. The results obtained using dielectric spectroscopy by varying the cell thickness show that the temperature ranges of SmC^*_α, $SmC^*_A(1/2)$ and $SmC^*_A(1/3)$ phases decrease with decreasing the cell thickness, and $SmC^*_A(1/3)$ phase is more stable than $SmC^*_A(1/2)$ phase. A relative stability of a phase is found to be due to its large polar anchoring strength and low free energy compared to other phases in a cell. Experimental results are found to agree with the theory.* "

7.1 Introduction

Chandani *et al* [100, 101] discovered antiferroelectric liquid crystals and in particular they discovered the three phases: SmC_A^* and SmC_α^* and SmC_γ^* in 1989. The other phases involving 4 layer periodicity with almost zero spontaneous polarization called AF was discovered by Okabe *et al.* [102]. Gorecka *et al.* [103] and Takezoe *et al.*, [104] proposed the models for SmC_γ^* and AF phases and gave the periodicity of layers as 3 and 4, respectively. Recently Chandani *et al.* [6] also discovered a sub-phase involving a 5 layer periodicity sandwiched in between the two and three layers and which exists over a narrow range of temperatures. This was later confirmed independently by Panov *et al.* [78] using a different optical technique. Several theoretical approaches were considered to explain a variety of these phases based on the Landau model [12, 13] namely: Ising model [105], the clock model [106], the distorted clock model [107, 108] and the discrete flexoelectric model [109, 110]. SmC^* phase is a tilted phase with the director tilted from the layer normal; each layer has a spontaneous polarization directed normal to the plane formed by the director and the layer normal. Due to chirality a helical structure is formed. Application of an electric field aligns the spontaneous polarization of each layer of the SmC^* phase along the field which creates a large induced macroscopic polarization. SmC_α^* phase consists of helical structure as well, but the pitch is extremely short. The structure of the SmC_α^* phase is obtained by minimizing the free energy of the system containing competing interactions between the nearest and the next nearest smectic layers [111].

The liquid crystal devices exploit the phenomenon of alignment by surfaces [112]. It is known for some time that the phase transitions of chiral smectic liquid crystals are controlled by their confinements [99, 113–120] and by their alignment [121]. The results of dielectric spectroscopy and optical texture have been used to compare the antiferroelectric liquid crystal (AFLC) phase behaviors of several compounds confined in cells of different thicknesses [113–115]. The electro-optical and dielectric spectroscopic investigations performed at several different cell gaps on three homologues of the series nOF1M7, where n denotes the

length of the unbranched terminal chain, showed that the bulk thermodynamic phase existed only in samples of cell thickness $> 25\ \mu m$. It was found that the Sm$C_A^*(1/3)$-SmC_A^* transition temperature was pushed downwards as the measurement cell gap was reduced for thin cells. For the thin cell, SmC^* phase completely disappeared and the coexistence of ferroelectric and antiferroelectric phases was observed [116]. It was also found that confinement of AFLC induces the phase transformation from the Sm$C_A^*(1/2)$ and Sm$C_A^*(1/3)$ phases to the frustrated ferroelectric SmC^* phase which showed thresholdless bistable switching [117]. The transition temperature of SmA-SmC^* transition is found to be lowered and the ferrielectric phases are suppressed in pores of nanometer dimensions of the liquid crystalline phases in porous media [118]. The second order transition from SmA-SmC^* is considerably broadened and an additional relaxation process is detected for liquid crystals confined in aerogel pores [99]. The thinner cells exhibit more field induced ferrielectric steps in optical transmission than do thicker cells [119].

7.2 Theory of the stability of smectic-C^* variant phases

The results on the transition temperatures and temperature ranges of SmC^* variant phases have not so far been obtained systematically as a function of the cell thickness and explained by a theory that determines the stability of these phases. This approach may also be applicable to other areas of surface science. We theoretically analyze the effect of surfaces on the stability of these phases by considering the contribution of the surface anchoring energy and the distortion energy of the bulk liquid crystals (LC) contributed by the surfaces to clarify as to how the transition temperatures depend on the cell thickness and as to why the temperature range of the some of the phases decreases rapidly with decreasing the cell thickness. Finally some of the phases are not observed for low cell thicknesses. We present experimental data on the variation of the transition temperatures and temperature ranges of the SmC^* variant phases of a prototype AFLC compound

as a function of the cell thickness in the range 3 to 80 μm. Experimental results also give the extent of the order of the suppression and the nature of the relative stability of the smectic-C^* variant phases with each other. Experimental results are found to agree with the theory. This theory was developed by Dr. Jang-kun Song [122, 123] in our Laboratory.

7.2.1 Depedence of transition temperature on cell surfaces

Orihara *et al.* [13] in 1990 were the first to suggest a phenomenological model based on the Landau theory of the phase transitions applied to the chiral smectic C^* variant phases soon after their discovery. Since then, several phenomenological models have emerged [12, 105–110] to explain the various experimental observations. Landau theory, which is a global method to describe the phase transitions is based on a few basic assumptions. One of these assumptions is that the free energy is analytic and at least one of the analytic terms contains temperature T in it. The temperature dependent term is selected to describe the phase transition phenomenologically. Therefore, despite a variety of phenomenological models based on Landau description having been advanced to date, the basic terms in the models are quite similar. For example the discrete flexoelectric model [109, 110] for explaining the emergence of possible phases/sub-phases given recently uses the free energy equation as below.

$$VF_b = \sum_{i=1}^{N} \Big[\tilde{F}_0(\theta) - \tilde{a}\frac{\Delta T}{T_C}(\cos\varphi_{i-1,i} + \cos\varphi_{i,i+1}) - \widetilde{B} \\ (\cos^2\varphi_{i-1,i} + \cos^2\varphi_{i,i+1}) + f(\mathbf{P}_{i-1}, \mathbf{P}_i, \mathbf{P}_{i+1}) \Big] \tag{7.1}$$

where F_b is the free energy per unit volume, V is the volume of cell, and $i = 1, ..., N$ is the running index of smectic layers for a cell having N layers. $\tilde{F}_0(\theta)$ is the tilt angle (θ) dependent free energy part that governs the non-tilted to a tilted phase transition, that is, the SmA^*-SmC^* phase transition. φ is defined as the angle that $\vec{c}$-director makes with the x-direction on the cell window as shown in Fig. 7.1*b*.

The second and third terms are designed for expressing the synclinic to the anticlinic phase transitions, that is, ferrro- to antiferroelectric layer ordering transition. $\Delta T = T - T_C$, where T_C is the transition temperature between the synclinic and anticlinic smectic-C^* phases in the absence of any intermediate phases. The second term is temperature dependent while other terms are temperature independent. The last term in Eq. 7.1 introduced by Osipov *et al.* [110] is a function of the polarization $\mathbf{P}$, is devised in particular to explain the emergence of the various phases/sub-phases. The last term is dependent on the model and can be controversial. The first three terms however have a clear physical meaning and these appear in slightly different forms in almost all of the phenomenological models based on the Landau free energy expansion. The in-layer molecular directors for the synclinic or anticlinic orderings almost lie in a single plane for positive $\widetilde{B}$. As the temperature increases, the ferroelectric configuration is favored by positive $\widetilde{a}$. Eq. 7.1 can be rewritten as

$$\begin{aligned} F_b &= T\frac{1}{V}\sum_{i=1}^{N}\Big[-\widetilde{a}\frac{1}{T_C}(\cos\varphi_{i-1,i}+\cos\varphi_{i,i+1})\Big] \\ &+\frac{1}{V}\sum_{i=1}^{N}\Big[\tilde{F}_0(\theta)+\widetilde{a}(\cos\varphi_{i-1,i}+\cos\varphi_{i,i+1}) \\ &-\widetilde{B}(\cos^2\varphi_{i-1,i}+\cos^2\varphi_{i,i+1})+f(\mathbf{P}_{i-1},\mathbf{P}_i,\mathbf{P}_{i+1})\Big] \end{aligned} \tag{7.2}$$

Now Eq. 7.2 can be rewritten as

$$\begin{aligned} F_b &= T\langle-\frac{\widetilde{a}}{T_C}(\cos\varphi_{i-1,i}+\cos\varphi_{i,i+1})\rangle + F_O \\ &\equiv AT + F_O, \end{aligned} \tag{7.3}$$

where $A \equiv -\frac{\widetilde{a}}{T_C}\langle\cos\varphi_{i-1,i}+\cos\varphi_{i,i+1}\rangle \equiv -A_O\langle\cos\varphi_{i-1,i}+\cos\varphi_{i,i+1}\rangle$. $\langle\ \rangle$ denotes the average per unit volume, and replaces the summation in Eq. 7.2. Here, F_O denotes the sum of all the other terms in Eq. 7.2 per unit volume and is independent of temperature and dependent on the structure, polarization etc. With a cell

having surface area S and thickness d, the total free energy can be written as

$$F_T = SdF_b + 2SF_s \tag{7.4}$$

$$F_T/Sd \equiv F_t = F_b + 2F_s/d. \tag{7.5}$$

Here, F_s is the free energy contributed by the unit surface. This includes the anchoring energy and the distortion energy of the bulk liquid crystals contributed by the surfaces. Hence, we get $F_t = AT + F_O + 2F_s/d$. Here, since we are considering a small shift in the phase transition temperatures due to the surface effect, F_s is considered to be independent of temperature for a narrow temperature range of temperatures close to the phase transition temperature. We consider the phase transition between the phases 1 and 2 having $q_T = q_1$ (lower temperature) and $q_T = q_2$ (higher temperature) phases. At the bulk transition temperature T_C in the absence of the surfaces, the bulk free energies of two phases are the same. Hence,

$$A_{q1}T_C + F_{O,q1} = A_{q2}T_C + F_{O,q2}. \tag{7.6}$$

The transition temperature, T by including the surface effect can be found as

$$A_{q1}T + F_{O,q1} + 2F_{s,q1}/d = A_{q2}T + F_{O,q2} + 2F_{s,q2}/d. \tag{7.7}$$

Hence, the transition temperature's dependence on the surfaces is given as:

$$T = T_C - \frac{2(F_{s,q1} - F_{s,q2})}{d(A_{q1} - A_{q2})} = T_C - \frac{2\Delta F_{s,(q1,q2)}}{\Delta A_{q1,q2}} \frac{1}{d} \tag{7.8}$$

We find from Eq. 7.8 that a shift in the transition temperatures due to the surface interactions is inversely proportional to the cell thickness, and it depends on the ratio of the differences in the coefficient of the temperature dependent term for the free energy (ΔA) and the surface energy (ΔF_s). The effect of surfaces can therefore be calculated using this equation. ΔA can be calculated using Eq. 7.3 and if phase 1 is the lower temperature phase then ΔA is always positive. Hence

the sign of the coefficient of the last term in Eq. 7.8 is determined by ΔF_s. If ΔF_s is positive, i.e., the surface energy of phase 1 is higher than for phase 2, the transition temperature decreases with decreasing the cell thickness. On the contrary, if ΔF_s is negative, that is, the surface energy of phase 1 is lower than of phase 2, the transition temperature increases by decreasing the cell thickness.

Free energy parameter A can be found from Eq. 7.3 for the transitions among SmC^*, Sm$C^*_A(1/2)$, Sm$C^*_A(1/3)$ and SmC^*_A phases. However, for the transitions among SmA^*, SmC^*_α and SmC^*, the first term in Eq. 7.1 contributes significantly to the phase transition. That is, close to the SmA^*-SmC^* transition, the tilt angle θ changes sharply with temperature, and the free energy is mostly governed by the tilt angle dependent term. Note that the Landau expansion for the second-order SmA^* to SmC^* transition is described as

$$F_{AC} = f_0 + a_0(T - T_{AC})\theta^2 + a_4\theta^4 + ... \tag{7.9}$$

Thus, for the transitions among SmA^*, SmC^*_α and SmC^*, $A \equiv a_0\theta^2$. Here, a_0 is the Landau coefficient of the temperature dependent term. a_0 is much greater than $A_0 = \widetilde{a}/T_C$, since the energy difference between SmA^* and SmC^* is 10^3 times to that between SmC^* and SmC^*_A [110], $\widetilde{a}$ is the coefficient of the second term in Eq. 7.1. Therefore, in Eq. 7.8, ΔA for the transitions among SmA^*, SmC^*_α and SmC^* is much higher than those among SmC^*, Sm$C^*_A(1/2)$, Sm$C^*_A(1/3)$ and SmC^*_A. This means that the transition temperatures between SmA^*, SmC^*_α and SmC^* phases are found to be largely insensitive to the cell thickness.

In order to calculate ΔF_s for the phase transitions among the variant SmC^*, we consider the surface energy F_s in detail. We assume that the phase transition occurs in the bulk liquid crystal as well within the interface of the cell with the liquid crystal (LC). The surface energy induces a distortion in the bulk LC. F_s can be separated into three different types of energies; the surface anchoring energy W_s, the distortion energy of helix $d\overline{\varphi}/dz$ and the in-layer distortion along the thickness direction $d\overline{\varphi}/dy$. These energies are actually coupled to each other, and hence the total energy F_s written below can be calculated from different components with

justifiable approximations.

$$F_s = W_s + \frac{1}{S}\int \left[K_1 \left(\frac{d\overline{\varphi}}{dz} - \overline{\varphi}_0 \right)^2 + K_2 \left(\frac{d\overline{\varphi}}{dy} \right)^2 \right] dV, \tag{7.10}$$

$\overline{\varphi}$ is the azimuthal angle of the director of the last layer of a single period of the structure in each phase, *i.e* $\overline{\varphi}$ is the angle of every forth layer, third layer and the second layer in Sm$C^*_A(1/2)$, Sm$C^*_A(1/3)$ and SmC^*_A phases, respectively. For SmC^*, $\overline{\varphi} = \varphi$. $\overline{\varphi}_0 = 2\pi/p$ (p is the pitch) is the wave vector. W_s can be written as [124],

$$W_s = -w_1\langle \cos\varphi_1 - \cos\varphi_2 \rangle - w_2\langle \cos^2\varphi_1 + \cos^2\varphi_2 \rangle, \tag{7.11}$$

where w_1, w_2 are the polar and the non-polar coefficients of the anchoring energies respectively, and φ_1, φ_2 are values of φ at surfaces 1 and 2 respectively. When w_2 is sufficiently large, φ_1 and φ_2 should be either 0 or π. $\langle\ \rangle$ in Eq. 7.11 denotes the average over the unit surface.

7.2.2 Director distribution in smectic-C^* variant phases

The director distributions for different cells with AFLC in different phases based on the works [31, 125] for SmC^* are plotted in Fig. 7.1. In the SmC^*_A and Sm$C^*_A(1/2)$ phases the number of layers of $\varphi = 0$ is the same as that of $\varphi = \pi$ in the unwound state resulting in zero spontaneous polarization, whereas in the of SmC^* and Sm$C^*_A(1/3)$ phases the number of layers with $\varphi = 0$ and $\varphi = \pi$ is not the same in the unwound state resulting in non-zero spontaneous polarization. In the SmC^*_A and Sm$C^*_A(1/2)$ phases, W_s does not depend on whether $\overline{\varphi} = 0$ or π. However in SmC^* and Sm$C^*_A(1/3)$ phases, it depends strongly on whether $\overline{\varphi} = 0$ or π. When the thickness is large, the in-layer distortion energy is rather small, consequently W_s is the most dominant term in F_s. So, $\overline{\varphi}_1$ and $\overline{\varphi}_2$ are determined to have a minimum W_s, hence $\overline{\varphi}_1$ should be opposite to $\overline{\varphi}_2$ as shown in Fig. 7.1(a). However, when the thickness is low, the in-layer distortion energy increases, and in order to reduce F_s, as in Eq. 7.10, the inlayer distortion energy has to be

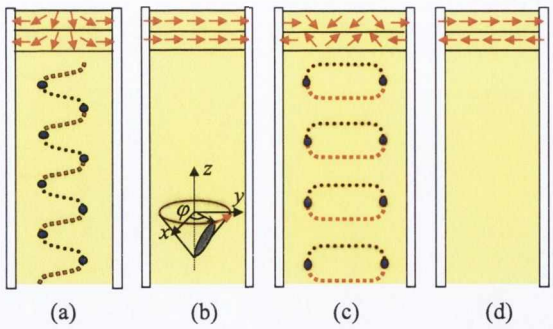

Figure 7.1: Schematic for the director distribution in SmC^* variant phases based on the works of Brunet [31] and Glogarova [125]. The director distribution of SmC^* phase for a thick cell (a) and for a thin cell (b), where number of layers with $\varphi = 0$ and $\varphi = \pi$ is not the same in the unwound state resulting in a non-zero spontaneous polarization. The red arrows in upper part represent the spontaneous polarization along th y direction for the first two layers (twist structure), black and red dotted lines in the center denote the directors having $\overline{\varphi} = \pi/2$ and $-\pi/2$ respectively, and blue circles denote defects. The director distribution in the Sm$C^*_A(1/3)$ phase follows the same distribution of (a) and (b) for thick and thin cells respectively except the director of the third layer is opposite to the first two layers. The director distribution in SmC^*_A phase for a thick cell (c) and thin cell (d), where the number of layers of $\varphi = 0$ is the same as of $\varphi = \pi$ in the unwound state resulting in a zero spontaneous polarization phases. The director distribution of the Sm$C^*_A(1/2)$ phase follows the same distribution of (c) and (d) for thick and thin cells respectively except the repeating unit is of four layers. The defects in (a) and (c) induced by the helical structure disappear in a thin cell. In larger cell thicknesses, the twist structure in (a) coexists with the helical structure, whereas for intermediate cell thicknesses only twist structure exists.

reduced, in which case $\overline{\varphi}_1$ is the same as $\overline{\varphi}_2$ creating a uniform state as shown in Fig. 7.1(b). Thus, for SmC^* and Sm$C^*_A(1/3)$ phases, there exists a critical thickness d_c, for which W_s changes to reflect a sudden change from a twisted to a uniform state by a change in the direction of the director near one of the surfaces to reduce the inlayer distortion energy. The transition from the twist to the uniform alignment occurs when the anchoring energy difference between the two alignments becomes the same as the distortion energy of the twist. Approximately, it is found that $d_{c,1} = \pi^2 K_2/(2w_1)$ for SmC^* phase and $d_{c,1/3} = 3\pi^2 K_2/(2w_1)$ for Sm$C^*(1/3)$ phase. Thus, $d_{c,1/3}$ is three times thicker than $d_{c,1}$. However, for the SmC^*_A and

Table 7.1: A and F_s for SmA^* and smectic-C^* phases.

	A	$F_s(d < d_c, d_h)$	$F_s(d > d_c, d_h)$
SmC^*	$-2A_0$	$-2w_2 + K_1\overline{\varphi}_{0,1}^2 d$	$-2(w_1 + w_2) + d_h K_1 \overline{\varphi}_{0,1}^2 + \pi^2 K_2/d$
Sm$C_A^*(1/2)$	0	$-2w_2 + K_1\overline{\varphi}_{0,1/2}^2 d$	$-2w_2 + d_h K_1 \overline{\varphi}_{0,1/2}^2$
Sm$C_A^*(1/3)$	$2/3A_0$	$-2w_2 + K_1\overline{\varphi}_{0,1/3}^2 d$	$-2/3w_1 - 2w_2 + d_h K_1 \overline{\varphi}_{0,1/3}^2 + \pi^2 K_2/d$
SmC_A^*	$2A_0$	$-2w_2 + K_1\overline{\varphi}_{0,0}^2 d$	$-2w_2 + d_h K_1 \overline{\varphi}_{0,0}^2$
SmA^*	0	-	$-2w_2$
SmC_α^*	$a_0\theta_\alpha^2$	-	$-2w_2 + d_h K_1 \overline{\varphi}_{0,\alpha}$
SmC^*	$a_0\theta_{\text{ferro}}^2$	$-2w_2 + K_1\overline{\varphi}_{0,1}^2 d$	$-2(w_1 + w_2) + d_h K_1 \overline{\varphi}_{0,1}^2 + \pi^2 K_2/d$

Sm$C_A^*(1/2)$, W_s, does not depend on the direction of $\overline{\varphi}$, so the minimum energy state is determined to have a minimum inlayer distortion energy for the entire range of thicknesses as shown in Fig. 7.1(c), where $\overline{\varphi}_1 = \overline{\varphi}_2$.

Now, we consider the helical and the inlayer deformation energies. When the cell is thin, the inlayer distortion energy is too large to sustain the helical structure, hence the helical structures disappear and a uniform state is obtained. In the uniform state, the helical distortion energy becomes $K_1 d\overline{\varphi}_0^2$ per unit cell area from Eq. 7.10. As the cell thickness increases, a deformed helical structure appears from the center area and enlarges on increasing the cell thickness. From this state, the helical distorting energy may not increase by increasing the cell thickness, since the helical structure in the center area has zero helical distortion energy. Therefore, the helical distortion energy for large cell thicknesses can be expressed as $K_1 d_h \overline{\varphi}_0^2$, where d_h is another critical cell thickness indicating the change from the non-helical structure to the helical structure. Based on this model, the calculated A and F_s for the different phases are listed in Table 7.1. Usually typical domains in the surface stabilized ferroelectric cell, *UP* and *DOWN*, appear approximately for 2 to 4 μm thickness in SmC^* phase. For SmC_α^* phase, $\overline{\varphi}_{0,\alpha}$ is very large, so F_s is mostly governed by $\overline{\varphi}_{0,\alpha}$. The period of a pitch in SmC_α^* is just a few layers, while that in SmC^* is usually a few hundred of layers. The results are calculated from the suggested model for simplified conditions: $d_{c,1} = 2\mu m$, w_1/A_0=5.5 $\times$ $10^6 m$, $a_0\theta_\alpha^2 \sim 1000A_0$, $a_0\theta_{\text{ferro}}^2 \sim 1300A_0$, $\overline{\varphi}_{0,\alpha} \sim 50\overline{\varphi}_{0,1}$, $d_{h,1} = d_{h,0} = 5\mu m$, $d_{h,1/3} = d_{h,1/2} = 100\mu m$, $K_1\overline{\varphi}_{0,1}^2 = K_1\overline{\varphi}_{0,0}^2 = 0.01w_1$ and $K_1\overline{\varphi}_{0,1/3}^2 = K_1\overline{\varphi}_{0,1/2}^2 = 0$.

7.3 Experimental results of the stability of smectic-C^* variant phases

The model is experimentally verified using a prototype AFLC compound 12OF1M7(R)(Kingston Chemicals Hull, UK). The experiments were performed on cooling the sample from 110 ^oC to 70 ^oC. Sample cells consisted of a planar capacitor made of two chemically etched ITO coated glass plates with sheet resistance 20 $\Omega/\square$. For planar alignment, the conducting inner surfaces were spin coated with a polyimide RN 1175 alignment layer and rubbed parallel. The cells were filled with the liquid crystals in the isotropic phase. Dielectric measurements in the frequency range from 1 Hz to 10 MHz were made by using the Novocontrol Alpha High Resolution Dielectric Analyzer with a voltage of 0.03 V_{rms}. The thickness of the liquid crystal cell was measured based on the the measurements of the transmittance spectra of an UV-visible spectrometer (AvaSpec-2048) using the interference fringes caused by the reflection from the two close glass surfaces of the cell.

7.3.1 Determination of transition temperatures using dielectric spectroscopy

The temperature dependence of dielectric strength ($\Delta\epsilon$) and relaxation frequency (f_{max}) for three different cell thicknesses of 50 μm, 10 μm and 3 μm are shown in Fig. 7.2, Fig. 7.3 and Fig. 7.4 respectively. These are found by fitting the imaginary part of dielectric permittivity (ϵ'') to the Havriliak-Negami equation. The Havriliak-Negami equation for n relaxation processes is given by [126]

$$\epsilon^*(\omega) = \epsilon' - i\epsilon'' = \epsilon_\infty + \sum_{i=1}^{n} \frac{\Delta\epsilon_i}{[1 + (j\omega\tau_i)^{\alpha_i}]^{\beta_i}} - \frac{j\sigma_{dc}}{\epsilon_0\omega}, \tag{7.12}$$

where ϵ_∞ is the high-frequency permittivity, i is a variable denoting the number of the relaxation processes up to n, τ_i and $\Delta\epsilon_i$ are the relaxation time and the dielectric strength of the ith process, α_i and β_i are the corresponding fitting parameters.

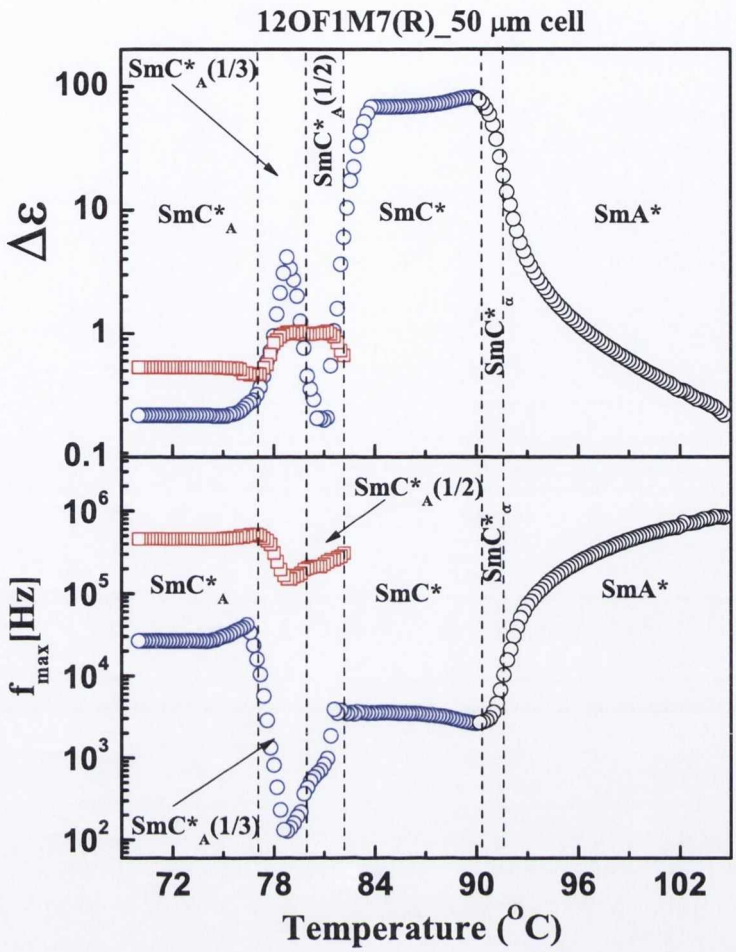

Figure 7.2: The temperature dependence of dielectric strength ($\Delta\epsilon$) and relaxation frequency (f_{max}) of different modes of the smectic-C^* variant phases for cell thickness of 50 μm for 12OF1M7(R).

The term $(-j\sigma_{dc}/\epsilon_0\omega)$ takes account of the dielectric loss due to ionic conduction. Ionic conduction is important at low frequencies. σ_{dc} is the dc conductivity, ω and ϵ_0 are the angular frequency and the permittivity of the free space, respectively. The transition temperatures of different phases are determined by measuring $\Delta\epsilon$ and f_{max} of different collective and non-collective modes in the dielectric spectra over a wide range of frequency from 1 Hz to 10 MHz for eight different cells, thickness ranging from 3 to 80 μm as described below. In SmA^* phase, the molecules in the planar configuration are parallel to the plane of the electrodes. The molecular relaxation mode around the long molecular axis (not shown) and the soft mode (black circles) are both dielectrically active as the dipole moment normal to the

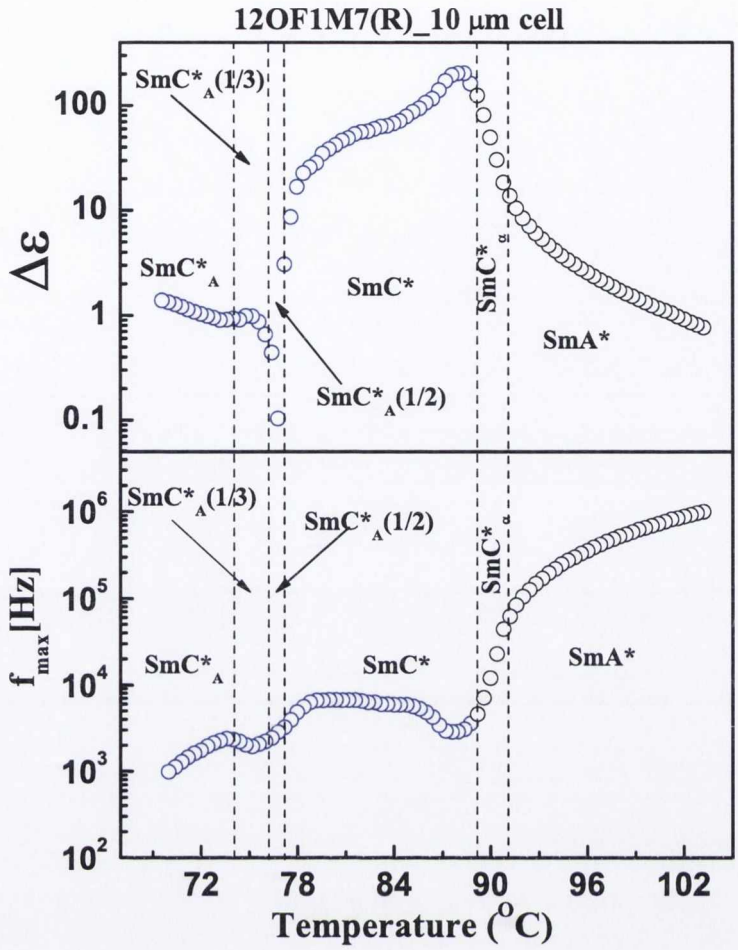

Figure 7.3: The temperature dependence of dielectric strength ($\Delta\epsilon$) and relaxation frequency (f_{max}) of different modes of the smectic-C^* variant phases for cell thickness of 10 μm for 12OF1M7(R).

electrodes fluctuates with electric field in this phase. Close to the transition temperature of the SmC^* phase, the soft mode dielectric strength sharply increases and the relaxation frequency sharply decreases. Based on it, this phase can therefore be easily identified. In the SmC^* phase, ferroelectric Goldstone mode (blue circles) is the most dominant and the phase is characterized mainly by this mode. The helix can easily be distorted by a weak external field and a change in the macroscopic polarization with field is very significant and the relative permittivity is very large. Among the chiral smectic-C^* variant phases which have a multi-layer repeating units, Sm$C^*_A(1/2)$ and SmC^*_A phases do not exhibit significant dielectric response due to a small macroscopic polarization as polarizations almost cancel

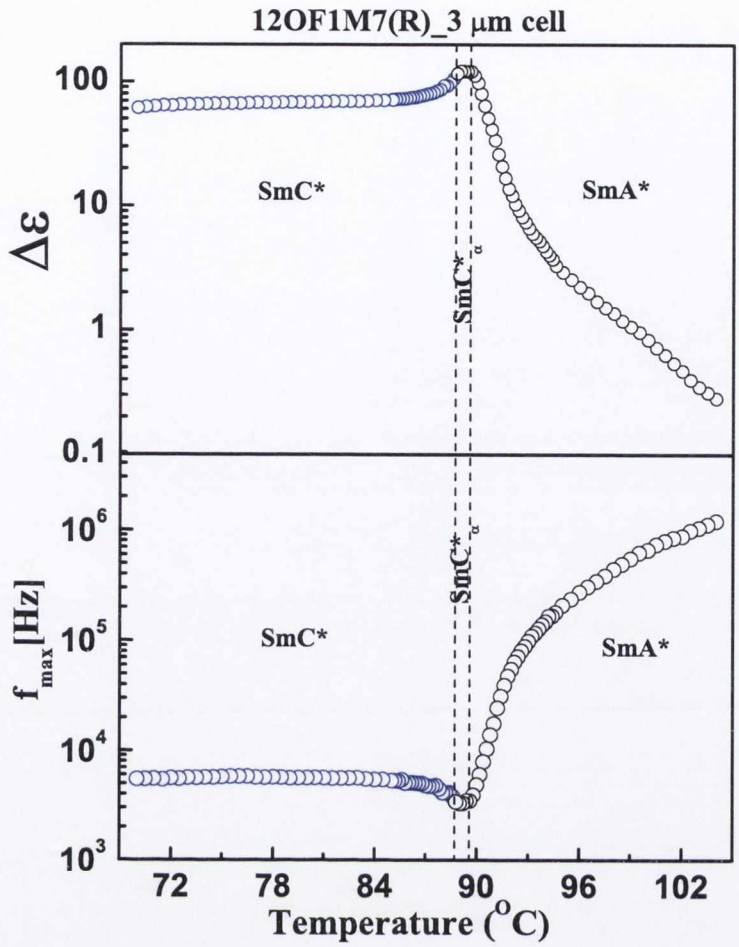

Figure 7.4: The temperature dependence of dielectric strength ($\Delta\epsilon$) and relaxation frequency (f_{max}) of different modes of the smectic-C^* variant phases for cell thickness of 3 μm for 12OF1M7(R).

out in the repeating unit. The transition temperature from SmC^* to Sm$C^*(1/2)$ is determined by a drop in the dielectric strength. In Sm$C^*_A(1/3)$, on the other hand, the polarization is only partially canceled out and this phase thus exhibits a significant dielectric response. Due to its long helical pitch, the value of the relaxation frequency f_{max} in Sm$C^*_A(1/3)$ is much lower than in SmC^* phase. The dielectric strength ($\Delta\epsilon$) is lower than in SmC^* due to a reduced macroscopic plarization. The transition temperature from Sm$C^*_A(1/2)$ to Sm$C^*_A(1/3)$ is determined by an increase in the dielectric strength and decrease in relaxation frequency, whereas the transition temperature from Sm$C^*_A(1/3)$ to SmC^*_A is determined by a drop in the dielectric strength and an increase in relaxation frequency for the low frequency mode. Apart from the above discussed modes, several other modes appear

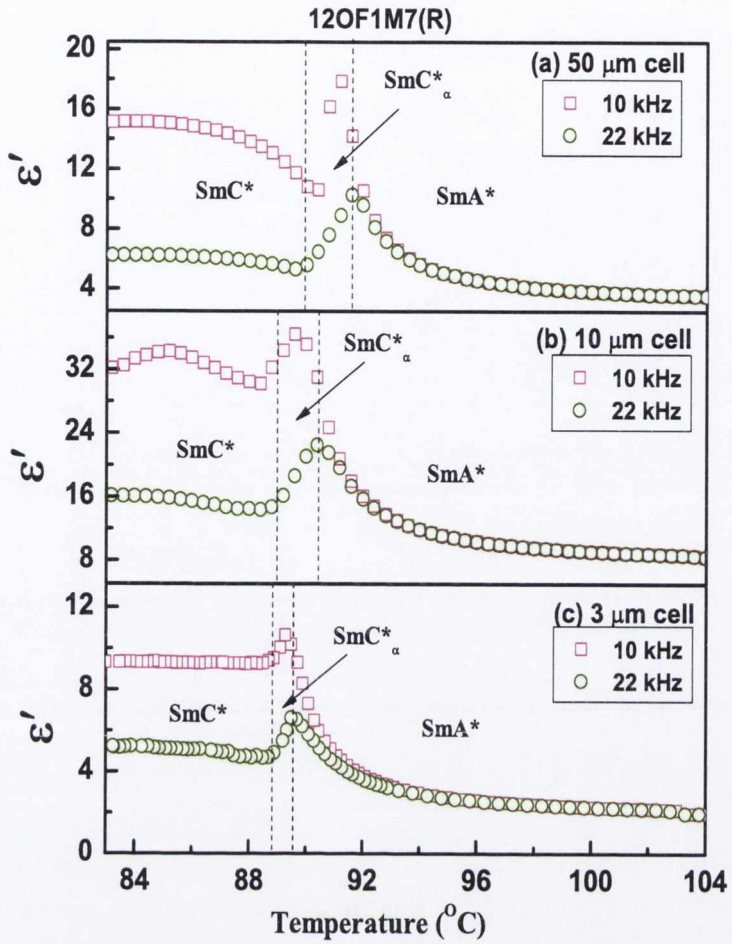

Figure 7.5: The temperature dependence of the real part of the dielectric permittivity (ϵ') in SmC^*_α phase for two frequencies of 10 kHz and 22 kHz for cell thickness of 50 μm (a), 10 μm (b) and 3 μm (c) for 12OF1M7(R).

in the bulk smectic-C^* variant phases as shown by red squares in Fig. 7.2 for 50 μm cell. The characteristic dependence of the dielectric strength and frequency of the different modes for smectic-C^* variant phases are explained by Panarin *et al.* [127, 128] in detail. SmC^*_α phase is structurally equivalent to SmC^* phase but has an extremely short pitch compared to SmC^*. This is characterized by a change in the slope of the real part of the permittivity (ϵ') as a function of temperature [43] shown in Fig. 7.5 for 50 μm (a), 10 μm (b) and 3 μm (c) cells for frequencies of 10 kHz and 22 kHz. The first change in the slope is due to an increase in the amplitude of soft mode close to the SmA to SmC^*_α transition and the second is due to a decrease and then increase in the strength of Goldstone mode

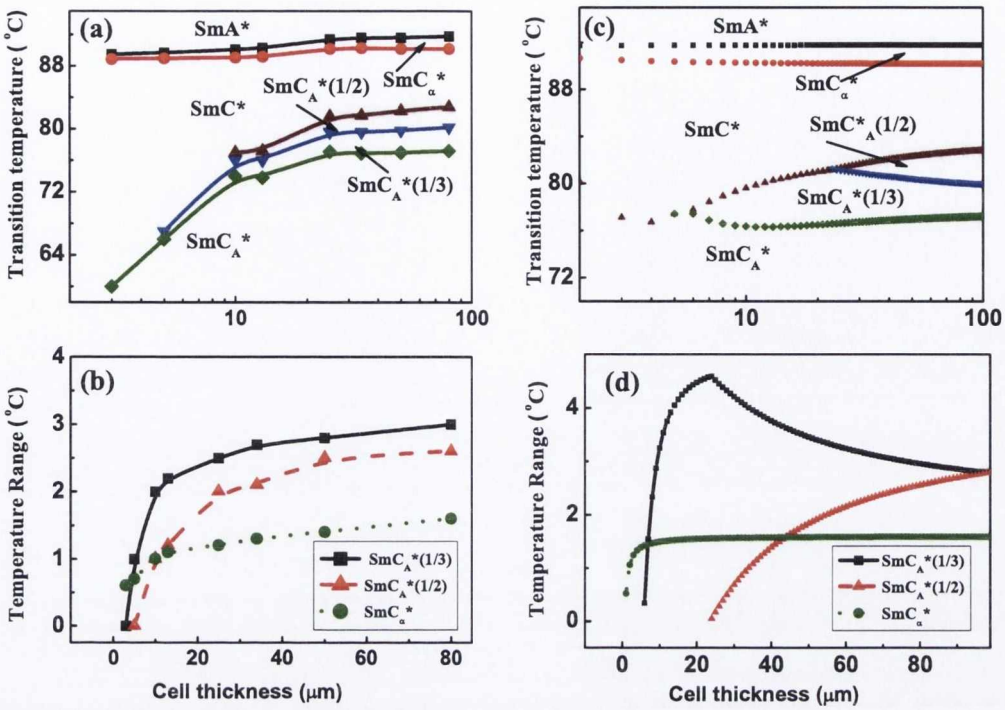

Figure 7.6: The dependence of the (a) transition temperature of the phases and (b) temperature range for which SmC^*_α, Sm$C^*_A(1/2)$ and Sm$C^*_A(1/3)$ phases are stable as a function of the cell thickness that varies from 3 to 80 μm. $(c-d)$ represents the calculated results under the condition: w_1/A_0=5.5 $\times$ $10^6 m$.

at the SmC^*_α to SmC^* transition. Note that for 10 μm cell, the surface-induced mode appears which is not inherent of the phase but is a result of the influence of the cell substrates. This along with the soft mode results in an increased dielectric strength at the SmC^*_α to SmC^* transition compared to that for a 50 μm cell.

7.3.2 Dependence of transition temperatures and temperature ranges in smectic-C^* phases

We note from Figs. 7.2, 7.3, 7.4 and 7.5 that the temperature ranges of SmC^*_α, Sm$C^*_A(1/2)$ and Sm$C^*_A(1/3)$ phases are less for 25 μm than for 50 μm cell. Furthermore Sm$C^*_A(1/2)$ and Sm$C^*_A(1/3)$ are completely suppressed by a thin cell of 3 μm thickness. Fig. 7.6$(a-b)$ show the experimental results for the dependence of the transition temperatures of the phases and the temperature range for

which the phases: SmC^*_α, Sm$C^*_A(1/2)$ and Sm$C^*_A(1/3)$ are stable with the cell thickness varying from 3 to 80 μm. We note that the transition temperatures of almost all phases show a decreasing trend by decreasing cell thickness. We find that on reducing the cell thickness, the Sm$C^*_A(1/2)$ phase disappears prior to the Sm$C^*_A(1/3)$ phase, whereas the SmC^*_α phase is rather stable. For a cell thicknesses greater than 10 μm, the temperature ranges of the phases do not vary to a large extent, whereas for lower cell thicknesses, they decrease rapidly by decreasing the cell thickness to the extent that for a thickness 3 μm, Sm$C^*_A(1/2)$ and Sm$C^*_A(1/3)$ totally disappear. Fig. 7.6$(c-d)$ show the plots of the calculated results from the theoretical model. Here, we may assert that exact determination of the phase transition temperature is rather difficult since the phase transition occurs gradually as the cell thickness is reduced. The phase transition temperatures are also influenced by the coexistence of phases. The results presented in Fig. 7.6 are carried out to gain an understanding of the qualitative behavior of the stability of the smectic-C^* variant phases as a function of the cell thickness. Moreover, we also point out that the experiments are carried out during cooling of the sample, the results therefore include the super-cooling effect. On the contrary the theory given here excludes the super-cooling effect. The intrinsic phase transition temperature, which is usually represented as T_c, is different from the actual transition temperature (represented as T_0) for the first order transition. T_c is the temperature where the free energy of the two phases becomes the same, and T_0 is the temperature where the phase transition occurs including the super cooling effect. Most phenomenological models for the transitions between the tilted smectic phases aim to find T_c, ignoring the super-cooling effect, though the super cooling is actually very large especially for thin cells. Our theory also focuses to find T_c. Note that the super cooling in the phase transitions between the tilted smectics is rather different from the conventional concept of the super cooling, because in the tilted smectics, it is governed mostly by the surface effects while normally it is governed by the free energy barrier between the two the phases. This is the case for most of the phenomenological theories. This is one of the main reasons for slight disagreement in experimental and theoretical results presented in Fig. 7.6$(a-d)$ apart from the

simplifications made in the theoretical calculations. Therefore, as the thickness of the cell is reduced, experimentally measured transition temperatures may be further reduced due to the super-cooling effect [114]. Since the super cooling may occur for all the phases, the temperature range for the stability of each phase may not be affected by this effect. However, the theoretical results are in good qualitative agreement with the experiments considering the significant simplifications made in the calculations. For the Sm$C^*_A(1/3)$ data in Fig. 7.6(d), we note that the temperature range of the Sm$C^*_A(1/3)$ phase is rather constant up to the cell thickness where the Sm$C^*_A(1/2)$ disappears, and then sharply decreases by decreasing the cell thickness. A similar two step stability appears in the experimental results as shown in Fig. 7.6(b).

The suppression of these phases by decreasing cell thickness was also observed by Lagerwall *et al.* [113, 114]. Hiraoka *et al.* [117] found that the temperature range of the Sm$C^*_A(1/2)$ phase increases by decreasing the cell thickness, which is different from our results. This is because in their material, there SmC^* phase is not present, and while the transition temperature between the SmC^*_α and Sm$C^*_A(1/2)$ phase is not significantly affected as explained, the transition between the Sm$C^*_A(1/2)$ and Sm$C^*_A(1/3)$ phases decreases with the cell thickness due to the super cooling effect. Hence, the temperature range of the Sm$C^*_A(1/2)$ increases but it does not contradict the theory. Note that the Sm$C^*_A(1/2)$ and Sm$C^*_A(1/3)$ phases disappear when the cell thickness is decreased further in their results. Panarin *et al.* [120] observed suppression of the subphases by confinement, as w_1 is weak in all SmC^* variant phases of their experiment due to the cell surfaces not having been coated by a polymer. Sm-C^* variant phases therefore are shown to exist down to much lower cell thicknesses than is the case here as the surfaces are coated with a polymer.

7.4 Conclusions

In summary, the stability of SmC^*_α, Sm$C^*_A(1/2)$, Sm$C^*_A(1/3)$ and SmC^*_A phases is investigated by determining the transition temperatures and the temperature range for which these are stable by varying the cell thickness experimentally. A simple theory has explained experimental observations: *i*) Sm$C^*_A(1/3)$ is more stable than Sm$C^*_A(1/2)$ by including the effect due to surfaces. This is due to the reason that Sm$C^*_A(1/2)$ has the highest anchoring energy compared to the adjacent phases due to an absence of the polar anchoring energy. *ii*) The stability is mostly due to a large polar anchoring strength with large spontaneous polarization and a consequent reduction in its surface energy. *iii*) SmC^*_α is rather stable and the transition temperatures between the higher temperature phases are rather unaffected by the surfaces. This arises from the higher temperature dependent coefficient of the free energy. *iv*) The temperature range of Sm$C^*_A(1/3)$ is rather constant up to a thickness for which Sm$C^*_A(1/2)$ exists. Once Sm$C^*_A(1/2)$ disappears, the temperature range of Sm$C^*_A(1/3)$ decreases rapidly by decreasing the cell thickness.

Chapter 8

Effects of confinement and electric field on the dielectric properties of smectic-C^*_α phase

"In this chapter, *Dielectric permittivity measurements are carried out to investigate the effects of confinement and electric field of a chiral smectic liquid crystal on the Sm-C^*_α phase for various cell thicknesses under the influence of electric field. On reducing the cell thickness, the surface-induced mode appears. This is a result of the influence of the cell substrates, and increases the dielectric strength of the Sm-C^*_α phase. The distribution parameter of the relaxation process, α decreases significantly, and in the case of a thin cell, the decrease observed reflects wide symmetric distribution of relaxation process. On increasing the electric field, the dielectric strength decreases and the relaxation frequency increases in the Sm-C^*_α phase. These are explained by the 'helical fracture' model, originally proposed for the Sm-C^* phase.* "

8.1 Introduction

Several theoretical approaches have been considered over the years to explain a variety of liquid crystalline phases based on the Landau model [12, 13], Ising model [105] and clock model [106, 111]. The short pitch helical structure of the frustrated Sm-C^*_α phase was obtained by minimizing the free energy of the system containing competing interactions between the nearest and next nearest smectic layers [111], and the fact that the tilt angle varies with temperature was used to understand the dielectric and dynamical properties of the phase [129, 130]. The Sm-C^*_α phase has been extensively studied by various experimental techniques such as differential scanning calorimetry, x-ray diffraction, electro-optic response, dielectric response and Raman scattering [131–134]. The short pitch helical structure of the Sm-C^*_α phase was experimentally confirmed through resonant x-ray scattering experiments [135, 136]. The switching behavior of the Sm-C^*_α phase was also explained by considering the antiferroelectric aspect of the helical structure recently [137].

Dielectric observations show that the Sm-A^*-Sm-C^*_α transition is identified by a change in slope of the temperature dependence of the dielectric strength of the soft mode [43, 44]. The compound 12OF1M7 has been extensively studied under the name AS-573 to investigate the ferrielectric subphases with high q_T parameter [127], the relaxation processes in antiferroelectric liquid crystalline phases [128], and the field-induced phase transitions [138]. The series of nF1M7 chiral liquid crystalline compounds, where n denotes the length of the unbranched terminal chain, were studied by dielectric spectroscopy for different cell thicknesses showing that the dielectric response is dominated by the surface induced structures if the cell gap is reduced and reflecting that the bulk thermodynamic phases exist in a very thick cell [114]. The optical reflectivity measurement on 12OF1M7(R) was also performed to confirm the existence of the Sm-C^*_α phase with nano-scale helical pitch [139]. The influence of dc bias on the Sm-C^*_α phase was also investigated to confirm the helical structure of the phase, which is strongly modified under dc bias field [44, 140].

8.2 Experimental details

The AFLC sample, 12OF1M7(R) synthesized by Kingston Chemical, Hull, U. K, was investigated for cell thicknesses varying from 3 to 80 μm. The thickness of the liquid crystal cell was measured based on the the measurements of the transmittance spectra of a UV-visible spectrometer (AvaSpec-2048) using the interference fringes caused by the reflection from two parallel glass surfaces of the cell closely separated from each other. The cell thickness was calculated using the following formula:

$$d = \frac{\lambda_k \lambda_{k+n} n}{2(\lambda_{k+n} - \lambda_k)} \tag{8.1}$$

Where λ_k and λ_{k+n} are the wavelengths of two maxima (minima) seperated by n minima (maxima) correspondingly. The electric-field-induced birefringence of 12OF1M7(R) was measured for a 25 μm thick homeotropic cell by applying an in-plane electric field. The gap between the electrodes was 180 μm. The details of the measurement are described elsewhere [6]. The field-induced birefringence at each temperature was measured by changing the applied field in 100 steps. The temperature was lowered at a rate of 0.01 ^oC/min. To assure thermal equilibrium, the sample was kept at each measuring temperature for 1 min before changing the field. The dielectric measurements were performed on cooling the sample from 110 ^oC to 60 ^oC. Sample cells for low frequency (<1 MHz) dielectric measurements consisted of a planar capacitor made of two chemically etched ITO coated glass plates with sheet resistance 20 $\Omega/\square$. For planar alignment, the conducting inner surfaces were spin coated with a polyimide RN 1175 alignment layer and rubbed parallel. The cells were filled with the liquid crystals in the isotropic phase. Dielectric measurements in the frequency range from 1 Hz to 1 MHz were made by using the Novocontrol Alpha High Resolution Dielectric Analyzer with an ac voltage of 0.03 V.

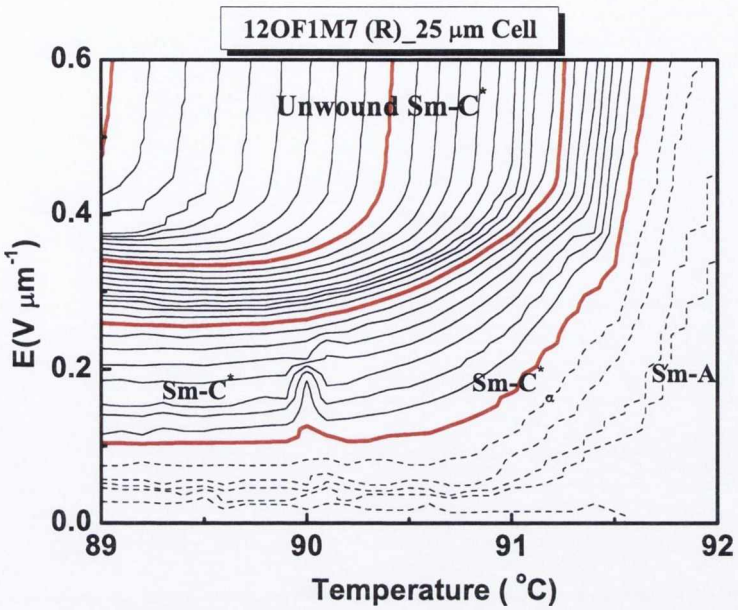

Figure 8.1: Electric-field-induced birefringence measured in the cooling cycle in 25 μm homeotropic cells of nominally pure 12OF1M7(R). This clearly shows the existence of the Sm-C^*_α phase in the cooling process. The birefringence contours drawn in solid lines are at steps of 0.5×10^{-4} and some auxiliary lines in smaller steps are drawn in dotted lines.

8.3 Electric field induced birefringence based on PEM Set Up

The Sm-C^*_α phase was identified by electric field induced birefringence and dielectric spectroscopy measurement in 12OF1M7(R). Fig. 8.1 shows the electric-field-induced birefringence measured in the cooling cycle in 25 μm homeotropic cells of nominally pure 12OF1M7(R) to confirm the existence of the Sm-C^*_α phase in the cooling process. This electric-field-induced birefringence measurement was performed by Dr. Chandani. The field-induced birefringence apparently increases during the unwinding process in the chiral smectic phases. Much more evidently, each phase shows its characteristic pattern of the birefringence contours. When the applied electric field is sufficiently high, all the phases under consideration become unwound Sm-C^*. The birefringence contours in principle are then parallel to the electric field, E-axis, as is obvious from the figure. The electroclinic effect

plays an important role in the Sm-A phase and the birefringence contours linearly rise with an increase in the applied electric field as seen in figure 8.1. In the Sm-C^* phase the helix starts to unwind even at low fields, resulting in a large birefringence, contour lines are horizontal and parallel to the temperature axis at lower field and becomes vertical at higher field when the helix is completely unwound. In contrast, the unwinding process of the ultra short- helical pitch in Sm-C^*_α requires relatively higher field than that required in the ordinary Sm-C^* phase. The phase transition from Sm-C^*_α into unwound Sm-C^* requires relatively high field but becomes lower with falling temperature as the short pitch becomes longer. In the temperature region just below Sm-A, the birefringence contour lines curved up finally becoming vertical in the complete unwound state. According to the above E-T phase diagram there exists Sm-C^*_α below the Sm-A phase in a very narrow temperature range of about 1.2 ^oC. However, the transition from Sm-C^*_α to Sm-C^* apparently occurs continuously indicating a second order phase transition. The photoelastic modulator-based set up was used previously to measure the electric field induced birefringence of the various subphases of 12OF1M7 [141].

8.4 Cell thickness dependent dielectric response in smectic-C^*_α phase

The dielectric response was studied for eight different cell thicknesses ranging from 3 to 80 μm to find the dependence of phase transition temperatures (T_c), dielectric strength ($\Delta\epsilon$) and relaxation frequency (f_{max}) on the cell thickness in the Sm-C^*_α phase. Experimental observations show that the Sm-A^*-Sm-C^*_α phase transition is only noticed by a change in the slope of the temperature dependence of the dielectric strength of the soft mode [43, 44]. The first change in the slope is due to an increase in the amplitude of soft mode close to the SmA to Sm-C^*_α transition and the second is due to a decrease and then increase in the strength of Goldstone mode at the Sm-C^*_α to Sm-C^* transition.

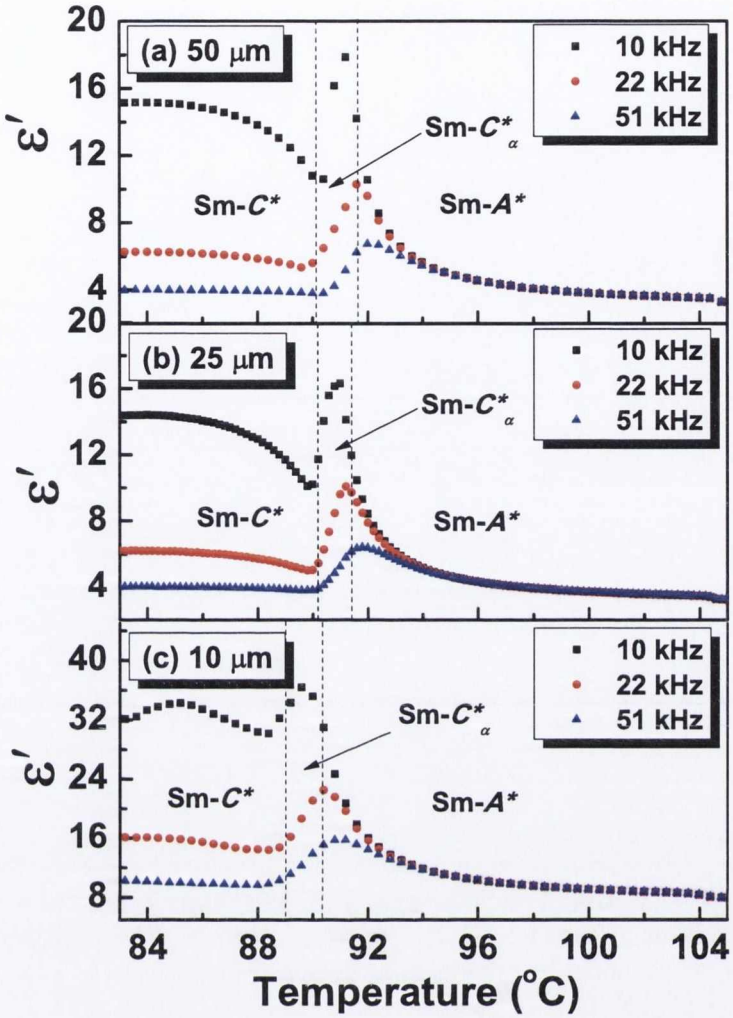

Figure 8.2: Dependence of real part of the dielectric permittivity (ϵ') on temperature for the different frequencies in nominally pure 12OF1M7(R) for cell thickness of 50 (a), 25 (b) and 10 μm (c).

Fig. 8.3 shows the dependence of dielectric strength ($\Delta\epsilon$), relaxation frequency (f_{max}) and distribution parameter (α) on temperature in the Sm-C^*_α phase for thicknesses of 50, 25, and 10 μm. These are found by fitting the imaginary part of dielectric permittivity (ϵ'') to the Havriliak-Negami equation. The Sm-C^*_α phase normally shows a contribution to $\Delta\epsilon$ due to azimuthal angle fluctuations, which indicates that in the Sm-C^*_α phase, we no longer see a pure soft mode, but a mixture of soft and Goldstone modes. On reducing the cell gap, we see the appearance of a mode that is not inherent of the phase but is a result of the influence of the cell substrates. Obviously, such a mode will get stronger the thinner the cell

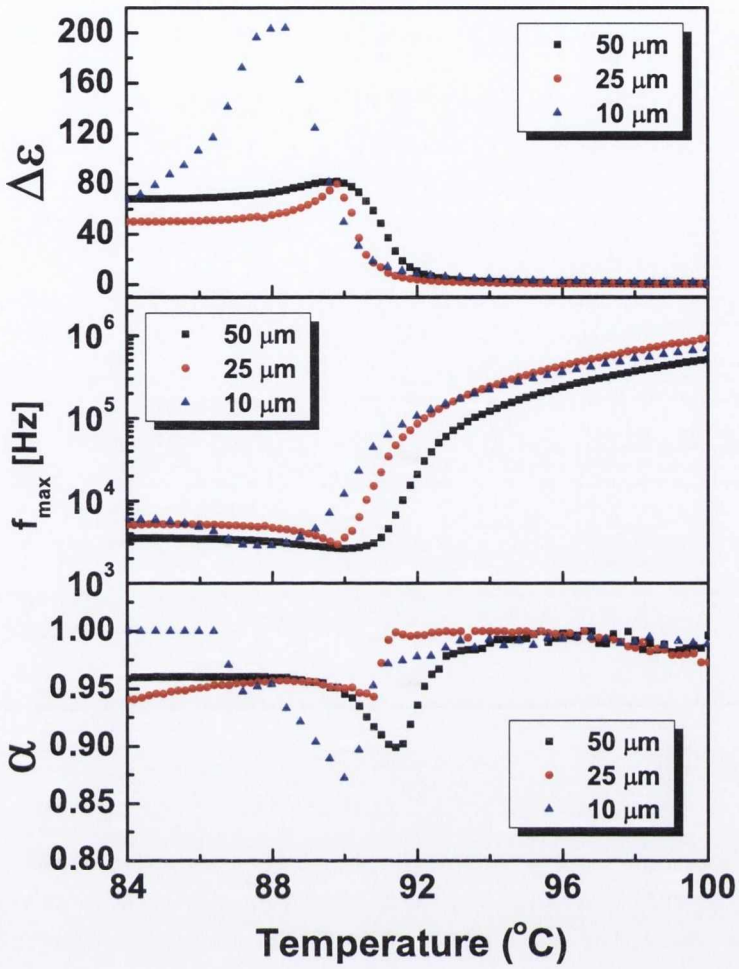

Figure 8.3: Dependence of dielectric strength ($\Delta\epsilon$), relaxation frequency (f_{max}) and distribution parameter (α) on temperature in the Sm-C^*_α phase of 12OF1M7(R) for thickness of 50, 25, and 10 μm

gap, as then the influence of the substrates dominates the response of the whole sample. This is why we get increasing $\Delta\epsilon$ on reducing the cell thickness. We also see that below the phase transition temperature the distribution parameter α decreases in magnitude and the decrease is quite large for 10 μm cell, which leads to a lower maximum value of the relaxation frequency. The decrease in distribution parameter on reducing the cell thickness shows that the mode is no longer a pure Debye relaxation mode. The most likely reason is that the response no longer reflects a single mode, but indeed two modes. One of them is of course the soft mode but the other may be a surface-induced mode and this grows in importance

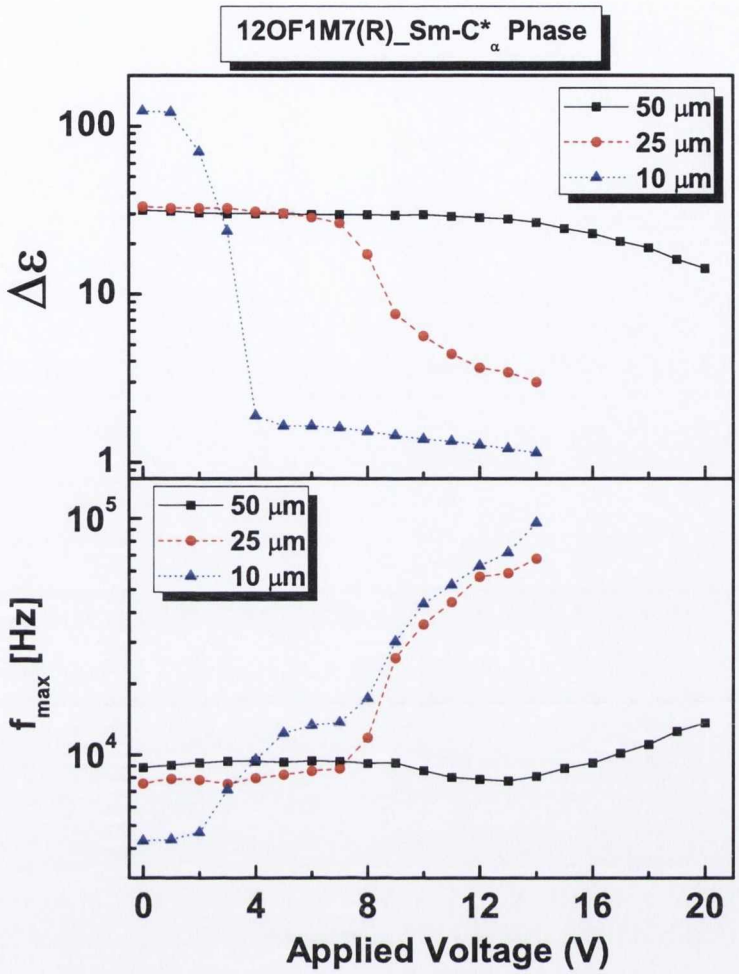

Figure 8.4: Dependence of dielectric strength ($\Delta\epsilon$), relaxation frequency (f_{max}) on dc bias in the Sm-C^*_α phase of 12OF1M7(R) for various thickness of 50, 25, and 10 μm.

as the cell thickness is decreased.

8.5 Electric field dependent dielectric response in smectic-C^*_α phase

Fig. 8.4 shows the dependence of dielectric strength ($\Delta\epsilon$), relaxation frequency (f_{max}) on dc bias in the Sm-C^*_α phase phase for various thicknesses of 50, 25, and 10 μm. The $\Delta\epsilon$ and f_{max} in the Sm-C^*_α phase are strongly modified under bias and it is probably connected with the ferroelectric like structure of this phase.

The behavior of $\Delta\epsilon$ and f_{max} under the influence of electric field in the Sm-C^*_α phase can be explained by an unwinding model based on helical fractures originally proposed for Sm-C^* phase [142, 143]. In this model, the applied field increases the stress on the helix, and the stress is released by the helix getting fractured followed by the propagation of domain wall. Here, the helical pitch increases with the helical fractures, because each π wall propagation reduces the helix by about half a turn. This is fundamentally different from a continuous increase in the helical pitch expected from the diverging pitch model [144]. The expression for electric field dependent $\Delta\epsilon$ and f_{max} based on the the non-diverging pitch model, can be calculated from the well-known free-energy expression and the corresponding Euler-Lagrange equation from the dependence of the azimuthal angle as a function of the distance along the layer normal $\phi(z) = qz + \sum \phi_i \sin[(i+1)qz]$, where $i = 0, 1, ...$, as follows:

For low fields;

$$\Delta\epsilon_{G,l} \simeq \frac{P_s A}{32\epsilon_0}\left[16 + \frac{2P_s^2 E_{dc}^2}{K^2 q^4} - \frac{9P_s^4 E_{dc}^4}{K^4 q^8}\right], \tag{8.2}$$

$$f_{G,l} = \frac{Kq^2}{2\pi\gamma}, \tag{8.3}$$

where $\Delta\epsilon_{G,l}$ and $f_{G,l}$ are the dielectric strength and the relaxation frequency of the Goldstone mode at low fields. $q(= 2\pi/p$, where p is pitch) is the wave vector, P_s is the spontaneous polarization, K is the elastic constant and γ is rotational viscocity. As shown in Eqs. 8.2 and 8.3, the relaxation frequency of the Goldstone mode does not depend on the dc bias at low fields, while the dielectric strength decreases slightly with the dc bias.

And for higher fields;

$$\langle P_E \rangle_h = \frac{2z_0 P_s}{p} + \frac{(p-2z_0)P_s}{p}\left[\frac{7}{16} + \frac{5}{16}\delta\phi_0 e^{jwt}\right]$$
$$= \frac{P_s}{16\rho}\left[16\rho - 9q + 5q\delta\phi_0 e^{jwt}\right], \tag{8.4}$$

$$\Delta\epsilon_{G,h} = \frac{5qP_s}{16\epsilon_0\rho E_{dc}} = \sqrt{\frac{5q^2KP_s}{64\epsilon_0^2 E_{dc}^3}}, \tag{8.5}$$

$$f_{G,h} = \frac{K\rho^2}{2\pi\gamma} = \frac{5P_s E_{dc}}{8\pi\gamma}, \tag{8.6}$$

Here $\rho = 2\pi/(p-2z_0)$ is the effective wave vector. $\Delta\epsilon_{G,h}$ and $f_{G,h}$ are the dielectric strength and the relaxation frequency of the Goldstone mode at higher fields. P_E is the component of P_s parallel to the applied field, and $P_E = P_s\cos\phi$. As shown in Eqs. 8.5 and 8.6, both the dielectric strength and the relaxation frequency are found to depend strongly on the amplitude of the dc bias at large fields. The dielectric strength decreases and the relaxation frequency increases with increasing field, which is in agreement with the experimental results shown in Fig. 8.4. However, the mechanism does not arise from the nonlinearity of K, but from an increase in the effective wave vector ρ. That is, the high bias field increases z_0 and reduces the effective pitch $(p - 2z_0)$, which in turn increases the relaxation frequency. Fig. 8.4 also shows that for larger thicknesses of the sample it takes higher amplitude of dc bias to unwind the helix compared to that of lower thickness of the sample.

8.6 Conclusion

The existence of Sm-C^*_α phase in 12OF1M7(R) is confirmed by dielectric spectroscopy and the electric-field-induced birefringence measurements. The dielectric strength ($\Delta\epsilon$), the relaxation frequency (f_{max}) and the distribution parameter (α) of Sm-C^*_α phases are very much dependent on the cell thickness. On reducing the cell gap, the surface-induced mode that is not inherent of the phase appears and this is a result of the influence of the cell substrates. This along with

the soft mode results in increasing dielectric strength and decreasing relaxation frequency in the Sm-C^*_α phase. The distribution parameter (α) decreases very much, and in the case of a thin cell, the decrease is quite large in the Sm-C^*_α phase indicating the behavior is a large mixture of the soft mode and a surface-induced mode. $\Delta\epsilon$ decreases and f_{max} increases in the Sm-C^*_α phase under the influence of dc bias, which is not connected to the nonlinearity of K, but is related to an increase in the effective wave vector ρ.

Chapter 9

Conclusions and Future Works

9.1 Summary and Conclusions of the Thesis

Despite many reports on the various aspects of the de Vries Sm-A^* phase, the structural aspects of this phase are not yet completely understood. In this Thesis, the structure and physical properties of de Vries Sm-A^* phase are studied using Electro-optics Spectroscopy, X-ray diffraction, and Dielectric Spectroscopy. The stability of smectic-C^* variant phases were also investigated by performing dielectric spectroscopy measurement for various cell thickness with application of dc electric field.

Mixtures of different compositions of an antiferroelectric and ferroelectric liquid crystal compounds that exhibits de Vries Sm-A^* to Sm-C^* and Sm-C^*_A transitions respectively were studied. The results of optical texture, birefringence, and the tilt angle suggest that a part of the Sm-A* phase is of de Vries type. The application of an external electric field produces a significant change in the color of the planar texture in de Vries Sm-A^* phase. In the de Vries Sm-A^* phase, the

molecules though significantly tilted but are azimuthally disordered. The external electric field produces a bias in the distribution of the tilt directions with the same symmetry as Sm-C^* through an azimuthal ordering of the already tilted molecules. This results in a significantly better alignment and a change in the birefringence and therefore a change in the spectrum of the transmitted light, and change in the color of the planar texture.

In the temperature range corresponding to the de Vries-type Sm-A^* phase, the macroscopic order parameter, measured by the birefringence is lower than in the conventional Sm-A^* phase due to molecular tilt and a distribution of the azimuthal angle. The disorder in the azimuthal angle with a tilt results in a reduction in the value of the birefringence with decreasing temperature. Furthermore, the application of the electric field in the de Vries-type Sm-A^* phase, forces these molecules to align in the same direction perpendicular to the electric field, which increases the birefringence. If the helical structure is suppressed by the surface anchoring, which is usually the case in planar cells, the S order parameter may show a sudden increase because the randomly distributed liquid crystalline molecules in de Vries SmA^* phase align along the same direction as in the SmC^* phase. As a result, the birefringence increases significantly on transition from de Vries-type SmA^* phase to SmC^* phase.

X-ray diffraction study shows that in the de Vries-type Sm-A^* phase the layer shrinkage at the Sm-A^*-Sm-C^* transition is smaller than the shrinkage which is expected by the conventional picture of 'tilting rodlike molecules'. It has also been shown that with increased ferroelectric component in the mixtures of ferroelectric and antiferroelectric compounds, the layer shrinkage at the Sm-A^*-Sm-C^* transition increases, while the layer shrinkage at the Sm-C^*-Sm-C^*_A transition decreases.

The Landau parameters associated with the Sm-A^*-Sm-C^*_A transition and Sm-A^*-Sm-C^* transition are calculated using Landau theory of the second order phase transition from dielectric measurements. It has been found that the soft mode dielectric relaxation strength decreases, Landau coefficient α increases

and the Curie-Weiss temperature range decreases at the de Vries-type Sm-A^*-Sm-C^* transition with increased ferroelectric composition in the mixture. These can be explained by the observation that with increased ferroelectric composition in the mixture, the layer shrinkage at the de Vries-type Sm-A^*-Sm-C^* transition increases, as a result of strong coupling between the tilt and the layer thickness. For low layer shrinkage materials, the restoring force of the tilt-angle fluctuations is smaller. As a result, the soft mode dielectric relaxation strength decreases, Landau coefficient α increases and the Curie-Weiss regime decreases with increased ferroelectric composition in the mixture. It has been also found that the soft mode dielectric strength and other related Landau parameters of the de Vries-type Sm-A^* phase exhibiting transitions both to Sm-C_A^* and to Sm-C^* phases are of the same order of magnitude except where the phase sequence on the phase-diagram is I-Sm-A^*-Sm-C^*-Sm-C_A^*. Measurements on mixtures close to an almost vertical line separating the phases Sm-C_A^* and Sm-C^* on the phase diagram may lead to further interesting results.

The dielectric strength and the response time are shown to increase, and the relaxation frequency decrease for a large temperature range up to a certain value of the electric field in the smectic-A^* phase. This behavior contrasts to that observed in a conventional smectic-A^*, but can be explained in terms of de Vries scenerio. On assuming the reorientation of the molecular dipoles with electric field to be of the Langevin type in the de Vries smectic-A^*, it is found that around 1300 molecules, corresponding to a minimum correlation length of $\xi_\perp \approx 45\ nm$ in a single layer cooperatively respond to the applied field. Hence, we must conclude the Langevin-type concentration of $f(\varphi)$ on the smectic cone with application of electric field is accompanied by the field dependent dielectric response in the de Vries SmA^*. Thus the field dependent dielectric response corresponds to the azimuthal angle (φ) fluctuations. The Langevin process does not consider the increase of μ_{eff} with electric field, which is supposed to be the case in the de Vries SmA^* since application of field tends to align the transverse dipole of these molecules. By fitting the electric field dependent polarization result, it has been found that with increasing field, μ_{eff} increases, hence the number of molecules

cooperatively responding to the field also increases, and so does the correlation length. As a result, $\Delta\epsilon$ and τ increase, and f_{max} decreases with the application of an increasing field.

The stability of SmC^*_α, Sm$C^*_A(1/2)$, Sm$C^*_A(1/3)$ and SmC^*_A phases is investigated by determining the transition temperatures and the temperature range for which these are stable by varying the cell thickness experimentally. A simple theory has explained experimental observations: *i*) Sm$C^*_A(1/3)$ is more stable than Sm$C^*_A(1/2)$ by including the effect due to surfaces. This is due to the reason that Sm$C^*_A(1/2)$ has the highest anchoring energy compared to the adjacent phases due to an absence of the polar anchoring energy. *ii*) The stability is mostly due to a large polar anchoring strength with large spontaneous polarization and a consequent reduction in its surface energy. *iii*) SmC^*_α is rather stable and the transition temperatures between the higher temperature phases are rather unaffected by the surfaces. This arises from the higher temperature dependent coefficient of the free energy. *iv*) The temperature range of Sm$C^*_A(1/3)$ is rather constant up to a thickness for which Sm$C^*_A(1/2)$ exists. Once Sm$C^*_A(1/2)$ disappears, the temperature range of Sm$C^*_A(1/3)$ decreases rapidly by decreasing the cell thickness.

The dielectric strength ($\Delta\epsilon$), the relaxation frequency (f_{max}) and the distribution parameter (α) of Sm-C^*_α phases are very much dependent on the cell thickness. On reducing the cell gap, the surface-induced mode that is not inherent of the phase appears and this is a result of the influence of the cell substrates. This along with the soft mode results in increasing dielectric strength and decreasing relaxation frequency in the Sm-C^*_α phase. The distribution parameter (α) decreases, and in the case of a thin cell, the decrease is quite large in the Sm-C^*_α phase indicating that the behavior is a large mixture of the soft mode and a surface-induced mode. $\Delta\epsilon$ decreases and f_{max} increases in the Sm-C^*_α phase under the influence of dc bias, which is not connected to the nonlinearity of K, but is related to an increase in the effective wave vector ρ.

9.2 Future Works

It has been found that the soft mode dielectric strength and other related Landau parameters of the de Vries-type Sm-A^* phase exhibiting transitions both to Sm-C_A^* and to Sm-C^* phases are of the same order of magnitude except where the phase sequence on the phase-diagram is I-Sm-A^*-Sm-C^*-Sm-C_A^*. Measurements on mixtures close to an almost vertical line separating the phases Sm-C_A^* and Sm-C^* on the phase diagram may lead to further interesting results.

With the application of an electric field in the de Vries SmA^* phase, the apparent optic axis orientation increases from zero (with $< \cos\varphi >= 0$, $< \cos^2\varphi >= 1/2$) to θ_A (with $< \cos\varphi > \approx 1$, $< \cos^2\varphi > \approx 1$, where θ_A is the smectic cone angle. The averages $< \cos\varphi >$ and $< \cos^2\varphi >$ can be evaluated using the Langevin equation for the azimuthal probablity distribution described by the ratio of an electric aligning energy $\mu_{eff}E$ to thermal energy k_BT. The Langevin process does not consider the increase of μ_{eff} with electric field, which is supposed to be the case in the de Vries SmA^* since application of a field tends to align the transverse dipole of these molecules. This is confirmed by achieving a better fitting of the field dependent polarization data to the Langevin process considering the increase of μ_{eff} with field. Hence, it is worth developing a model rather than artificial modification of the Langevin process, which will describe azimuthal probablity distribution by not only considering optic axis orientation, but also increase of μ_{eff} with electric field.

It could also be interesting to determine various orientation order parameters by measuring the Infrared absorbance components in de Vries Sm-A^* phase with planar and homeotropic alignment with the application of an electric field, and compare the results with conventional Sm-A^* phase.

Appendix A

A.1 Materials used for fabricating cells

Fig. A.1 shows the liquid crystal materials used in this thesis. The phase sequence shown in the figure may vary according to experimental conditions, material state, and experimental method.

MC815 and MC881 were synthesized by Mitsubishi Gas Chemical Company (MGC) in Japan. These materials were given to Prof. A. Fukuda and his coworkers for research purpose. 12OF1M7 was synthesized by Kingston Chemicals in Hull, UK. TSiKN65 was synthesized by Dr. J. Naciri at the Naval Research Laboratory, Washington DC, USA.The chemical structures of Felix0018 is not known (HOECHST AG Company in Germany).

For alignment layers, RN-1175 and RN-1266 supplied by Nissan Chemical Co. in Japan were used for planar alignment, and a Dow Corning silane coupling agent (72%3-(trimethoxysilyl)propyldimethyloctadecyl-ammonium-chloride and 28% MeOH) and carboxylatochromium complexes (chromolane) were used for homeotropic cells.

Commercial cells having 2, 5, 9 and 25 μm thickness were purchased from E. H. C Co., Ltd. in Japan, and were used for some measurements. For hand-made cells, either 0.7 mm thick glass coated with ITO (Indium Tin Oxide; 20$\Omega/\square$) or 1.1 mm thick glass coated ITO (100$\Omega/\square$) supplied by Prof. J. M. Oton in ETSI Telecomunicacion Ciudad Universitaria, Madrid, Spain, was used.

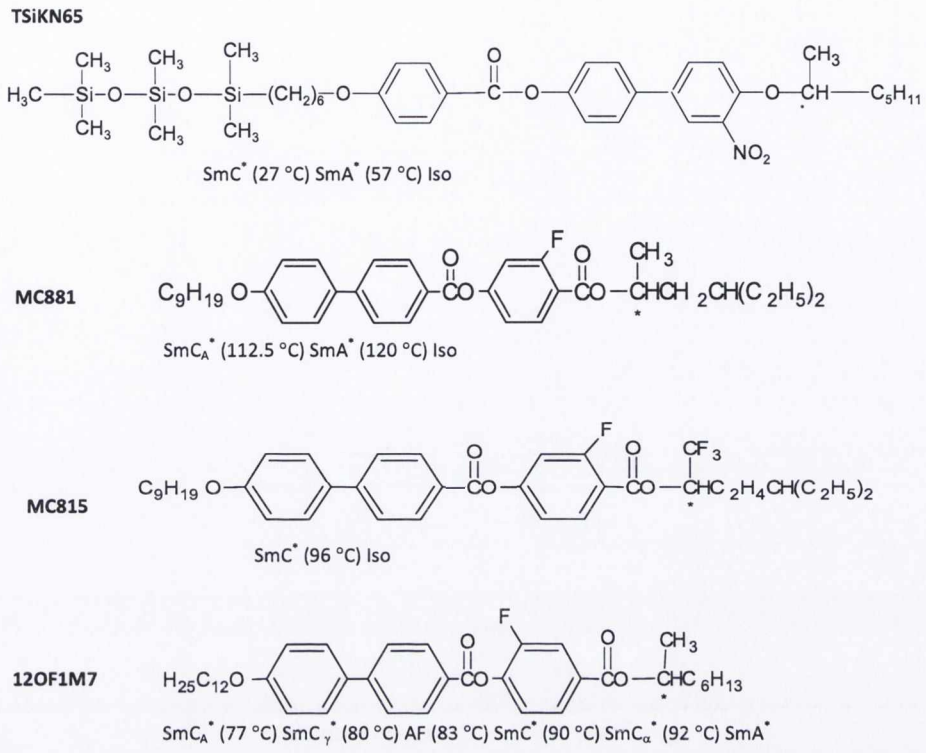

Figure A.1: Chemical structures and phase sequences of liquid crystal materials used in this thesis. Phase sequence could be measured slightly differently depending on experimental conditions, material state, and experimental method.

A.2 Apparatus

This section provides brief information about the main instruments used in this thesis. For further details concerning each instrument, please refer to the linked web-site.

• **Optical Microscope:** Olympus BX-52 (Olympus Company), including the objective lens (Olympus, LM PlanFI, 50X / 0.5NA), the condenser (Instech, 0.65 NA), and Leica DFC480 (Leica, Digital camera for microscope)

- http://www.olympusfluoview.com/brochures/pdfs/bx52.pdf

- http://www.leica-microsystems.com/

• **Broadband dielectric spectrometer:** This system includes Alpha-A High Performance Modular Measurement System (Novocontrol GmbH, Impedance analyzer, $3\times10^{-5} - 2 \times 10^{7}$ Hz), Agilent 4291B RF Impedance/Material Analyzer

(Agilent, $1 \times 10^6 - 1.8 \times 10^9$ Hz) and Quatro Cryosystem (Novocontrol GmbH, temperature controller, $-160 - +400$°C). Analysis software, WINFIT (Novocontrol GmbH, software) is required.

- http://www.novocontrol.de/
- http://www.home.agilent.com/agilent/home.jspx

• **Optical Spectrometer:** Lambda 900 UV/VIS/NIR spectrometer (PerkinElmer, broadband high resolution spectrometer), and Avaspec-2048 (Avantes, fast fiber optic spectrometer).

- http://www.perkinelmer.com/default.htm
- http://www.avantes.com/

• **Photo-Elastic Modulator (PEM) system:** PEM modulator (HINDS Instruments)

- http://www.hindsinstruments.com/PEM_Components/products/default.aspx
- see also references [6, 145] for applications

A.3 Software

• **Origin:** Origin 8.0 was used for analyzing experimental data, and for simple fitting simulation.

• **LaTex:** Miktex 2.7, Ghostscript 8.6, GSview, and TEXnicCenter were used for typesetting publications including this thesis.

Bibliography

[2] V.K. Agrawal H. Takezoe A. Fukuda Y. Takanishi, K. Hiraoka and M. Matsushita. *Jap.J. Appl. Phys.*, 30:2023, 1991.

[1] K. Hiraoka, Y. Takanishi, K. Skarp, H. Takezoe, and A. Fukuda. *Jpn. J. Appl. Phys., Part 2*, 30:L1819, 1991.

[3] H. Takezoe A. Fukuda T. Hagiwara Y. Suzuki T. Isozaki, T. Fujikawa and I. Kawamura. *Phys. Rev. B*, 48:13439, 1993.

[4] R. B. Meyer, L. Liebert, L. Strzelecki, and P. Keller. *J. Phys. Lett. (Paris)*, 36:L69, 1975.

[5] J. P. F. Lagerwall and F. Giesselmann. *ChemPhysChem*, 7:20, 2006.

[6] A. D. L. Chandani, N. M. Shtykov, V. P. Panov, A. V. Emelyanenko, A. Fukuda, and J. K. Vij. *Phys. Rev. E*, 72:041705, 2005.

[7] V. P. Panov, N. M Shtykov, A. Fukuda, J. K. Vij, R. A. Lewis, M. Hird, and J. W. Goodby. *Phys. Rev. E*, 69:060701(R), 2004.

[8] T. Isozaki, T. Fujikawa, H. Takezoe, A. Fukuda, T. Hagiwara, Y. Suzuki, and I. Kawamura. *Jpn. J. Appl. Phys.*, 31:L1435, 1992.

[9] A. Saupe. *Mol. Cryst. Liq. Cryst.*, 1:527, 1966.

[11] D. A. Dunmur, D. A. Hitchen, and X.-Y. Hong. *Mol. Cryst. Liq. Cryst.*, 140:303, 1986.

[10] Edited by D. Demus, J. W. Goodby, G. W. Gray, H. W. Spiess, and V. Vill. *Handbook of Liquid Crystals, Vol. 1.* Wiley-VCH, Weinheim, Germany, 1998.

[13] H. Orihara and Y. Ishibashi. *Jap. J. Appl. Phys.*, 29:L115, 1990.

[12] B. Zeks and M. Cepic. *Liq. Cryst.*, 14:445, 1993.

[15] S. Garoff and R. B. Meyer. *Phys. Rev. A*, 19:338, 1978.

[14] S. Garoff and R. B. Meyer. *Phys. Rev. A*, 19:338, 1979.

[16] Edited by J. W. Goodby et. al. *Ferroelectric Liquid Crystals: Principle, Properties and Applications, Vol. 7.* Gordon and Breach, Amsterdam, Netherlands, 1991.

[17] T. P. Rieker, N. A. Clark, G. S. Smith, D. S. Parmar, E. B. Sirota, , and C. R. Safinya. *Phys. Rev. Lett.*, 59:2658, 1987.

[18] A. de Vries. *Mol. Cryst. Liq. Cryst.*, 41:27, 1977.

[19] A. de Vries. *J. Chem. Phys.*, 71:25, 1979.

[20] A. de Vries, A. Ekachai, and N. Spielberg. *Mol. Cryst. Liq. Cryst.*, 49:143, 1979.

[21] S. Diele, P. Brand, and H. Sackmann. *Mol. Cryst. Liq. Cryst.*, 16:105, 1972.

[22] N. A. Clark, T. Bellini, R.-F. Shao, D. Coleman, S. Bardon, and D. R. Link. *Appl. Phys. Lett.*, 80:4097–4099, 2002.

[25] J. P. F. Lagerwall, F. Giesselmann, , and M. D. Radcliffe. *Phys. Rev. E*, 66: 031703, 2002.

[23] F. Giesselmann, P. Zugenmaier, I. Dierking, S. T. Lagerwall, B. Stebler, M. Kaspar, V. Hamplova, and M. Glogarova. *Phys. Rev. E*, 60:598, 1999.

[24] M. S. Spector, P. A. Heiney, J. Naciri, B. T. Weslowski, D. B. Holt, and R. Shashidhar. *Phys. Rev. E*, 61:1579, 2000.

[27] J. V. Selinger, P. J. Collings, , and R. Shashidhar. *Phys. Rev. E*, 64:061705, 2001.

[26] F. Giesselmann, J. P. F. Lagerwall, G. Andersson, and M. D. Radcliffe. *Phys. Rev. E*, 66:051704, 2002.

[28] *BX51 User Manual, publisher = Olympus, year = 2009, author = Olympus, address = http://www.olympusamerica.com.*

[29] D. W. Berreman. *Mol. Cryst. Liq. Cryst.*, 22:175, 1973.

[30] K. Hori. *Mol. Cryst. Liq. Cryst.*, 82:13, 1982.

[31] M. Brunet and E. Williams. *Ann. Phys.*, 3:237, 1977.

[32] J. Schacht I. Dierking, F. Giesselmann and P. Zugenmaier. *Liq. Cryst.*, 19: 179, 1995.

[33] C. S. Rosenblatt, R. Pindak, N. A. Clark, and R. B. Meyer. *J. Phys. (Paris)*, 39:1105, 1977.

[34] S. T. Lagerwall, M. Matuszczyk, P. Rodhe, and L. Oldman. *The Optics of Thermotropic Liquid Crystals, Chapt. 8.* Taylor and Francis, London, UK, 1998.

[35] P. Debye. *Polar Molecules.* Chemical Catalogue Co., New York, USA, 1929.

[36] K. S. Cole and R. H. Cole. *J. Chem. Phys.*, 9:341, 1941.

[37] K. S. Cole and R. H. Cole. *J. Chem. Phys.*, 10:98, 1941.

[38] S. Havriliak and S. Negami. *J. Polym. Sci.*, C14:99, 1966.

[39] F. M. Gouda. *Ph. D Thesis.* PhD thesis, Chalmers University of Technology, 1992.

[40] F. Gouda, K. Skarp, and S. T. Lagerwall. *Ferroelectrics*, 113:165, 1991.

[41] C. Filipic, T. Carlsson, A. Levsti, B. Zeks, R. Blinc, F. Gouda, S. T. Lagerwall, and K. Skarp. *Phys, Rev. A*, 38:5833, 1988.

[42] A. Levstik, T. Carlsson, C. Filipic, I. Levstik, and B. Zeks. *Phys. Rev. Lett.*, 35:3527, 1987.

[43] N. M. Shtykov, J. K. Vij, V. P. Panov, R. A. Lewis, M. Hird, and J. W. Goodby. *J. Mater. Chem.*, 9:1383, 1999.

[44] R. Douali, C. Legrand, V. Faye, and H. T. Nguyen. *Mol. Cryst. Liq. Cryst.*, 328:209, 1999.

[45] *AvaSpec-2048 User Manual, publisher = AvaSpec, year = 2009, author = AvaSpec, address = http://www.avantes.com.*

[46] J. Li and S. T. Wu. *J. Appl. Phys.*, 95:896, 2004.

[47] Y. Ouchi, J. Lee, H. Takezoe, A. Fukuda, K. Kondo, T. Kitamura, and A. Mukoh. *Jpn. J. Appl. Phys.*, 27:L725, 1988.

[48] L. Taylor, R. M. Richardson, J. Ebbutt, and J. C. Jones. *Mol. Cryst. Liq. Cryst.*, 263:255, 1995.

[49] C. Brown, P. E. Dunn, J. C. Jones, S. A. Jenkins, and R. M. Richardson. *Mol. Cryst. Liq. Cryst.*, 402:55, 2003.

[50] L. M. Blinov, L. A. Beresnev, N. M. Shtykov, and Z. M. Elashvili. *J. Phys.(Paris)*, 40:269, 1979.

[51] J. Hoffmann, W. Kuczynski, and J. Malecki. *Mol. Cryst. Liq. Cryst.*, 44: 287, 1978.

[52] S. Kimura, S. Nishiyama, Y. Ouchi, H. Takezoe, and A. Fukuda. *Jap. J. Appl. Phys.*, 26:L255, 1987.

[53] V. M. Vaksman and Yu. P. Panarin. *Mol. Mats.*, 1:147, 1992.

[54] R. Korlacki, A. Fukuda, and J. K. Vij. *Europhys. Lett.*, 77:36004, 2007.

[55] N. Hiji, Y. Ouchi, H. Takezoe, and A. Fukuda. *Jpn. J. Appl. Phys.*, 27:L1, 1988.

[56] S. T. Lagerwall, A. Dahlgren, P. Jagemalm, P. Rudquist, K. D'have, H. Pauwels, R. Dabrowski, and W. Drzewinski. *Adv. Funct. Mater.*, 11: 87, 2001.

[57] L. S. Matkin, S. J. Watson, H. F. Gleeson, R. Pindak, J. Pitney, P. M. Johnson, C. C. Huang, P. Barois, A. M. Levelut, G. Srajer, J. Pollmann, J. W. Goodby, , and M. Hird. *Phys. Rev. E*, 64:021705, 2001.

[58] D. M. Walba, E. Korblova, L. Eshdat, M. C. Biewer, H. Yang, C. Jones, M. Nakata, M. Talarico, R. Shao, and N. A. Clark. *J. Soc. Inf. Display*, 15: 585, 2007.

[59] N. Hayashi, A. Kocot, M. J. Linehan, A. Fukuda, J. K. Vij, G. Heppke, J. Naciri, S. Kawada, and S. Kondoh. *Phys. Rev. E*, 74:051706, 2006.

[60] O. E. Panarina, Yu. P. Panarin, J. K. Vij, M. S. Spector, and R. Shashidhar. *Phys. Rev. E*, 67:051709, July 2003.

[61] Yu. P. Panarin, F. Antonelli, O. E. Panarina, Y. Semenova, J. K. Vij, M. Reihmann, and G. Galli. *Ferroelectrics*, 310:111, 2004.

[62] M. Krueger and F. Giesselmann. *Phys. Rev. E*, 71:041704, 2005.

[63] O. E. Panarina, Yu. P. Panarin, F. Antonelli, J. K. Vij, M. Reihmann, and G. Galli. *J. Mater. Chem.*, 16:842, July 2006.

[64] N. Hayashi, T. Kato, A. Fukuda, J. K. Vij, Yu. P. Panarin, J. Naciri, R. Shashidhar, S. Kawada, and S. Kondoh. *Phys. Rev. E*, 2005.

[65] M. V. Gorkunov, F. Giesselmann, J. P. F. Lagerwall, T. J. Sluckin, and M. A. Osipov. *Phys. Rev. E*, 75:060701(R), 2007.

[66] K. Saunders, D. Hernandez, S. Pearson, and J. Toner. *Phys. Rev. Lett.*, 98: 197801, 2007.

[67] M. Takeuchi, K. Chao, T. Ando, T. Matsumoto, A. Fukuda, and M. Yamashita. *Ferroelectrics*, 246:1–20, 2000.

[68] Y. Yoshioka, M. Johno, T. Yui, and T. Matsumoto. *Euro. Pat. Appl.*, page EP1039329, 2000.

[69] U. Manna, J. K. Song, Yu. P. Panarin, A. Fukuda, and J. K. Vij. *Phys. Rev. E*, 77:041707, 2008.

[70] J. Pavel and M. Glogarova. *Liq. Cryst.*, 9:87, 1991.

[71] G. P. Crawford, R. E. Geer, J. Naciri, R. Sashidhar, and B. R. Ratna. *Appl. Phys. Lett.*, 65:2937, 1994.

[72] R. E. Geer, S. J. Singer, J. V. Selinger, B. R. Ratna, and R. Shashidhar. *Phys. Rev. E*, 57:3059, 1998.

[73] L. Lejcek and S. Pirkl. *Liq. Cryst.*, 8:871, 1990.

[74] W. H. de Jeu. *Physical properties of Liquid Crystalline materials.* Gordon and Breach, New York, USA, 1980.

[75] I. Musevic, M. Skarabot, R. Blinc, W. Schranz, and P. Dolinar. *Liq. Cryst.*, 20:771, 1996.

[76] B. Zeks R. Blinc G. Heppke A. V. Kityk M. Skarabot, M. Cepic and I. Musevic. *Phys. Rev. E*, 58:575, 1998.

[77] *ESRF Beamlines, publisher = ESRF, year = 2009, author = ESRF, address = http://www.esrf.eu.*

[78] V. P. Panov, J. K. Vij, Yu. P. Panarin, C. Blanc, V. Lorman, and J. W. Goodby. *Phys. Rev. E*, 75:042701, 2007.

[79] C. C. Huang, S. Wang, X. Han, A. Cady, R. Pindak, W. Caliebe, K. Ema, K. Takekoshi, and H. Yao. *Phys. Rev. E*, 69:041702, 2004.

[80] I. Musevic, R. Blinc, and B. Zeks. *The Physics of Ferroelectric and Antiferroelectric Liquid Crystals.* World Scientific, Singapore, 2000.

[81] B. Zeks. *Mol. Cryst. Liq. Cryst.*, 114:259, 1984.

[82] R. Blinc and B. Zeks. *Phys. Rev. A*, 18:740, 1978.

[83] S. Sarmento, M. R. Chaves, P. S. Carvalho, and H. T. Nguyen. *Liq. Cryst.*, 28:1561, 2001.

[84] K. Hiraoka, Y. Ouchi, H. Takezoe, A. Fukuda, S. Inui, S. Kawano, M. Saito, and H. Iwane. *Mol. Cryst. Liq. Cryst.*, 199:197, 1991.

[85] M. Kimura, M. Yamada, and T. Akahane. *Ferroelectrics*, 214:59, 1998.

[86] M. Glogarova, C. Destrade, J. P. Marcerou, J. J. Bonvent, and H. T. Nguyen. *Ferroelectrics*, 121:285, 1991.

[87] E. Gorecka, D. Pociecha, M. Glogarova, and J. Mieczkowski. *Phys. Rev. Lett.*, 81:2946–2949, 1998.

[88] P. J. Collings, B. R. Ratna, and R. Shashidhar. *Phys. Rev. E*, 67:021705, 2003.

[89] R. B. Meyer and R. A. Pelcovits. *Phys. Rev. E*, 65:061704, 2002.

[90] F. Gouda, G. Anderson, S. T. Lagerwall, K. Skarp, B. Stebler, T. Carlsson, B. Zeks, C. Filipic, and A. Levstik. *Liq. Cryst.*, 6:219, 1989.

[91] Yu. P. Kalmykov, J. K. Vij, H. Xu, A. Rappaport, and M. D. Wand. *Phys. Rev. E*, 50:2109, 1994.

[92] Ch. Bahr and G. Heppke. *Phys. Rev. A*, 39:5459, 1989.

[93] J. Naciri, J. Ruth, G. Crawford, R. Shashidhar, and B. R. Ratna. *Chem. Mater.*, 7:1397, 1995.

[94] I. Abdulhalim and G. Moddel. *Liq. Cryst.*, 9:493, 1991.

[95] B. R. Ratna, K. S. Nelson, H. Li, C. Wilson, and J. Naciri. *Proc. of SPIE*, 3297:2, 1998.

[96] A. Hermanns, C. M. Wilson, J. Y. Patel, J. W. Naciri, J. R. Lindle, and B. R. Ratna. *Appl. Phys. Lett.*, 73:3644, 1998.

[97] J. W. Goodby, R. Blinc, N. A. Clark, S. T. Lagerwall, M. A. Osipov, S. A. Pikin, T. Sakurai, K. Yoshino, and B. Zeks. *Ferroelectric Liquid Crystal: Principles, Properties and Applications.* Gordon and Breach, Amsterdam, 1991.

[98] Y. Shimbo, E. Gorecka, D. Pociecha, F. Araoka, M. Goto, Y. Takanishi, K. Ishikawa, J. Mieczkowski, K. Gomola, and Hideo Takezoe. *Phys. Rev. Lett.*, 97:113901, 2006.

[99] H. Xu, J. K. Vij, A. Rappaport, and N. A. Clark. *Phys. Rev. Lett.*, 79:249, 1997.

[100] A. D. L. Chandani, E. Gorecka, Y. Ouchi, H. Takezoe, and A. Fukuda. *Jpn. J. Appl. Phys.*, 28:L1265, 1989.

[101] A. D. L. Chandani, Y. Ouchi, H. Takezoe, A. Fukuda, K. Terashima, K. Furukawa, and A. Kishi. *Jpn. J. Appl. Phys.*, 28:L1261, 1989.

[102] N. Okabe, Y. Suzuki, I. Kawamura, T. Isozaki, H. Takezoe, and A. Fukuda. *Jpn. J. Appl. Phys.*, 31:L793, 1992.

[103] E. Gorecka, A. D. L. Chandani, Y. Ouchi, H. Takezoe, and A. Fukuda. *Jpn. J. Appl. Phys., Part 1*, 29:131–137, 1990.

[104] H. Takezoe, J. Lee, Y. Ouchi, and A. Fukuda.

[105] A. Fukuda, Y. Takanishi, T. Isozaki, K. Ishikawa, and H. Takezoe. *J. Mater. Chem.*, 4:997–1026, 1994.

[106] A. Roy and N. V. Madhusudana. *Europhys. Lett.*, 36:221, 1996.

[107] T. Akizuki, K. Miyachi, Y. Takanishi, K. Ishikawa, H. Takezoe, and A. Fukuda. *Jpn. J. Appl. Phys., Part 1*, 38:4832–4837, August 1999.

[108] P. M. Johnson, D. A. Olson, S. Pankratz, T. Nguyen, J. W. Goodby, M. Hird, and C. C. Huang. *Phys. Rev. Lett.*, 84:4870, 2000.

[109] A. V. Emelyanenko and M. A. Osipov. *Phys. Rev. E*, 68:051703, 2003.

[110] M. A. Osipov, A. Fukuda, and H. Hakoi. *Mol. Cryst. Liq. Cryst.*, 402:9, 2003.

[111] M. Cepic and B. Zeks. *Mol. Cryst. Liq. Cryst.*, 263:61, 1995.

[112] D. W. Berreman. *J. Opt. Soc. Am.*, 62:502, 1972.

[114] J. P. F. Lagerwall, D. D. Parghi, D. Kruerke, F. Gouda, and P. Jagemalm. *Liq. Cryst.*, 29:163, 2002.

[113] J. Lagerwall, P. Rudquist, S. Lagerwall, and B. Stebler. *Ferroelectrics*, 277: 239, 2002.

[115] P. Jagemalm, J. P. F. Lagerwall, A. Dahlgren, L. Komitov, A. S. Matharu, C. Grover, F. Gouda, and A. A. Kutub. *Ferroelectrics*, 244:147, 2000.

[116] H. Moritake, N. Shigeno, M. Ozaki, and K. Yoshino. *Liq. Cryst.*, 14:1283, 1993.

[117] K. Hiraoka, T. Maruyama, and Y. Noguchi. *Jpn. J. Appl. Phys.*, 43:8173, 2004.

[118] Yu. P. Panarin, C. Rosenblatt, and F. M. Aliev. *Phys. Rev. Lett.*, 81:2699, 1998.

[119] J.-F. Li, E. A. Shack, Y.-K. Yu, X.-Y. Wang, C. Rosenblatt, M. E. Neubert, S. S. Keast, and H. Gleeson. *Jpn. J. Appl. Phys.*, 35:L1608, 1996.

[120] Yu. P. Panarin, Y. P. Kalmykov, S. T. Mac Lughadha, H. Xu, and J. K. Vij. *Phys. Rev. E*, 50:4763, 1994.

[121] W. Chen, M. B. Feller, and Y. R. Shen. *Phys. Rev. Lett.*, 63:2665, 1989.

[123] J. K. Song. *Ph. D Thesis.* PhD thesis, Trinity College Dublin University, 2008.

[122] U. Manna, J. K. Song, G. Power, and J. K. Vij. *Phys. Rev. E*, 78:021711, 2008.

[124] M. A. Handschy, N. A. Clark, and S. T. Lagerwall. *Phys. Rev. Lett.*, 51:471, 1983.

[125] M. Glogarova, J. Fousek, L. Lejcek, and J. Pavel. *Ferroelectrics*, 58:161, 1984.

[126] S. J. Havriliak and S. Negami. *Polym.*, 8:161, 1967.

[127] Yu. P. Panarin, O. Kalinovskaya, J. K. Vij, and J. W. Goodby. *Phys. Rev. E*, 55:4345, 1997.

[128] Yu. P. Panarin, O. Kalinovskaya, and J. K. Vij. *Liq. Cryst.*, 25:241, 1998.

[129] J. M Hollidt D. Lotzsch D. Moro M. Cepic, G. Heppke and B. Zeks. *Mol. Cryst. Liq. Cryst.*, 263:207, 1995.

[130] M. Cepic and B. Zeks. *Liq. Cryst.*, 20:29, 1996.

[131] Y. Y. Yamada N. Yamamoto M. Fukui, H. Orihara and Y. Ishibashi. *Jpn. J. Appl. Phys.*, 28:L849, 1989.

[132] H. T. Nguyen M. Glogarova, H. Sverenyak and C. Destrade. *Ferroelectrics*, 147:43, 1993.

[133] K. Hiraoka, A. Taguchi, Y. Ouchi, H. Takezoe, and A. Fukuda. *Jpn. J. Appl. Phys., Part 2*, 29:L103, 1990.

[134] H. T. Nguyen R. Farhi and V. L. Lorman. *Europhys. Lett.*, 40:49, 1997.

[135] P. Mach, R. Pindak, A.-M. Levelut, P. Barois, H. T. Nguyen, C. C. Huang, and L. Furenlid. *Phys. Rev. Lett.*, 81:1015, 1998.

[136] A. M. Levelut P. Barois H. T. Nguyen H. Baltes M. Hird K. Toyne A. Seed J. W. Goodby C. C. Huang P. Mach, R. Pindak and L. Furenlid. *Phys. Rev. E*, 60:6793, 1999.

[137] J. P. F. Lagerwall. *Phys. Rev. E*, 71:051703, 2005.

[138] N. M. Shtykov, J. K. Vij, R. A. Lewis, M. Hird, and J. W. Goodby. *Phys. Rev. E*, 62:2279, 2000.

[139] V. P. Panov, B. K. McCoy, Z. Q. Liu, J. K. Vij, J. W. Goodby, and C. C. Huang. *Phys. Rev. E*, 74:011701, 2006.

[140] J. Kedzierski Z. Raszewski J. Rutkowska, P. Perkowski and S. Kolsowicz. *Mol. Cryst. Liq. Cryst.*, 409:389, 2004.

[141] V. Manjuladevi, Yu. P. Panarin, and J. K. Vij. *Appl. Phys. Lett.*, 91:052911–1–3, 2007.

[142] J. K. Song, U. Manna, and J. K. Vij. *Europhys. Lett.*, 82:26003, 2008.

[143] J. K. Song, J. K. Vij, and I. Kobayashi. *Phys. Rev. E*, 75:051705, 2007.

[144] R. B. Meyer. Ferroelectric liquid crystals. *Mol. Cryst. Liq. Cryst.*, 40:33, 1977.

[145] N. M. Shtykov, A. D. L. Chandani, A. V. Emelyanenko, A. Fukuda, , and J. K. Vij. *Phys. Rev. E*, 71:021711, 2005.